Development of Conditional Source-term Estimation (CSE) Framework for Turbulent Buoyant Diffusion Flames

by

Ahmed M.K. Abdalhamid

A thesis
presented to the University of Waterloo
in fulfillment of the
thesis requirement for the degree of
Doctor of Philosophy
in
Mechanical and Mechatronics Engineering

Waterloo, Ontario, Canada, 2024

© Ahmed M.K. Abdalhamid 2024

Examining Committee Membership

The following served on the Examining Committee for this thesis. The decision of the Examining Committee is by majority vote.

External Examiner:	Bart Merci Professor, Dept. of Structural Engineering and Building Materials, University of Ghent
Supervisor(s):	Cecile Devaud Professor, Dept. of Mechanical and Mechatronics Engineering, University of Waterloo
Internal Member:	Elizabeth Weckman Professor, Dept. of Mechanical and Mechatronics Engineering, University of Waterloo
Internal Member:	John Wen Professor, Dept. of Mechanical and Mechatronics Engineering, University of Waterloo
Internal-External Member:	Eric Croiset Professor, Dept. of Chemical Engineering, University of Waterloo

Author's Declaration

I hereby declare that I am the sole author of this thesis. This is a true copy of the thesis, including any required final revisions, as accepted by my examiners.

I understand that my thesis may be made electronically available to the public.

Abstract

Conditional Source-term Estimation (CSE) is a turbulent combustion model that relies on conditional averages of species mass fractions to provide closure for the mean chemical source terms. The model has the ability to account for detailed chemical kinetics while remaining computationally affordable for engineering cases. CSE has been successfully applied previously to simulate flames of different regimes and configurations. The current work aims at extending the CSE framework to model turbulent buoyant diffusion flames for the first time. Large Eddy Simulation (LES) is used to solve transport equations of mass, momentum, species and enthalpy. Chemistry is pretabulated prior to the simulations.

The LES FireFOAM solver is coupled with CSE approach. The new solver is first tested against University of Maryland methane line fire using different implementations for radiation modelling, all relying on the optically thin assumption. The results are validated against experimental measurements at different locations as well as previously published predictions of the same case using different combustion models. The predicted temperatures are in good agreement with the experimental data, except very close to the fuel inlet. The predicted flame height closely matches the experimental value. The predictions are consistent with previously published results as well.

Next, the inclusion of radiation absorption is considered by solving the radiative transfer equation (RTE), avoiding the optically thin approximation for the first time with CSE. Moreover, the weighted sum of grey gases (WSGG) approach is employed to estimate the absorption coefficients. The new framework is applied to the simulation of two medium and large scale methanol pool fires. The medium scale case is investigated using two angular meshes and compared to the optically thin results. The case that solves the RTE with fine angular mesh shows improved predictions. The radiative flux results show that the predictions align better with the measurements with the finer angular mesh outside the flame region. However, the results from both angular meshes are in agreement within the flame. For the large scale case, the time-averaged temperature predictions are in good agreement with the experimental data, except on the centerline downstream of the flame region where the results are overpredicted.

Finally, the newly developed CSE framework is extended to include soot modelling by coupling with two of the most widely used soot models in fire analysis. The new approach is used to simulate the ethanol pool fire case, providing acceptable predictions of soot and species mole fractions.

In conclusion, this study proves the capability of CSE in accurately simulating turbulent buoyant diffusion flames. Future work may address more complex fuels, cases of extinction with doubly-CSE, suppression by water mist, and more detailed soot models.

Acknowledgements

First, I would like to thank my supervisor, Prof. Cecile Devaud for her guidance and feedback throughout the time spent in my PhD process. Her expertise and insights have been valuable in shaping this thesis.

I would also like to thank the respectful committee members Prof. Bart Merci, Prof. Elizabeth Weckman, Prof. John Wen and Prof. Eric Croiset for agreeing to be part of the examining committee and for allocating the time and effort to read and review my thesis.

I am also thankful to my friends and colleagues, especially Ahmed Hussien, Mohammad Mortada, Ahmed AbdulMajuid and Mehdi Ashrafizadeh for their assistance and support. I also extend my thanks to Ahmed Beyrem, Mohamed Yehia, Moaz Khaled, Mazen Adel, Ahmed Hassan, Mahmoud Mabrouk, Ahmed Salah and Ahmed Hamouda. All of those people have made this journey enjoyable and memorable.

A special thanks goes to my family, especially my mother and father, whose love, patience, and understanding have been my greatest source of strength. Their constant support and belief in me have been a driving force throughout this process.

Lastly, I would like to acknowledge the financial support from the Natural Sciences and Engineering Research Council of Canada (NSERC), which made this research possible. Also, the Digital Research Alliance of Canada (alliance-can.ca) is acknowledged for providing the computational resources for the present work.

Thank you all for your contributions and support.

Dedication

This is dedicated to the ones I love: God, my family and my close friends.

Table of Contents

Examining Committee Membership ii

Author's Declaration iii

Abstract iv

Acknowledgements v

Dedication vi

List of Figures xi

List of Tables xvi

1 Introduction 1

1.1 Overview 1

1.2 Objectives 5

1.3 Thesis outline 6

1.4 Author's current contributions 7

2 Background 8

2.1 Governing Equations 8

2.2 Turbulent Flows 10

2.2.1 Direct numerical simulation . . . 10
2.2.2 RANS approach and Favre-averaging . . . 11
2.2.3 Large eddy simulation . . . 11
2.3 Summary . . . 14

3 Turbulent combustion and radiation modeling 16
3.1 Turbulent combustion models . . . 16
3.1.1 Eddy break up model . . . 17
3.1.2 EDM and EDC models . . . 17
3.1.3 Mixture fraction . . . 18
3.1.4 Laminar flamelet model . . . 19
3.1.5 Conditional moment closure model . . . 20
3.1.6 Transported probability density function methods . . . 21
3.1.7 Multiple mapping conditioning . . . 22
3.2 Conditional source term estimation . . . 23
3.2.1 Formulation . . . 23
3.2.2 Integral inversion and regularization . . . 26
3.3 Chemistry Tabulation . . . 27
3.4 Radiative Heat Transfer . . . 30
3.4.1 The radiative transfer equation . . . 30
3.4.2 Weighted sum of grey gases . . . 34
3.4.3 Optically thin approximation . . . 35
3.5 Soot formation and modeling . . . 35
3.6 Summary . . . 39

4 LES-CSE of a methane line flame with optically thin radiation 41
4.1 Computational details . . . 43
4.1.1 Experimental setup . . . 43

4.1.2 LES setup . . . 43
4.1.3 CSE details . . . 46
4.2 Radiation modeling . . . 47
4.3 Results . . . 48
4.3.1 Flame structure . . . 48
4.3.2 Time averaged temperatures . . . 49
4.3.3 Axial velocity and mixture fraction . . . 54
4.3.4 Species mass fractions . . . 55
4.3.5 Conditional averages . . . 56
4.3.6 Comparison with previously published numerical data . . . 56
4.4 Summary . . . 61

5 Coupling between CSE and RTE solver for LES of methanol pool fires 62
5.1 Radiation modeling . . . 64
5.2 Medium-scale methanol pool fire . . . 66
5.2.1 Computational details . . . 69
5.2.2 Results . . . 73
5.3 Large-scale methanol pool fire . . . 88
5.3.1 Experimental setup . . . 88
5.3.2 LES setup . . . 88
5.3.3 Results . . . 90
5.4 Summary . . . 97

6 Investigation of soot modeling in LES of a medium-scale ethanol pool flame coupled with CSE approach 99
6.1 Soot modeling . . . 100
6.2 Radiation modeling . . . 103
6.3 Computational details . . . 105

6.3.1 Experimental setup . . . 105
6.3.2 LES setup . . . 105
6.3.3 CSE details . . . 107
6.4 Results . . . 108
6.4.1 Flame structure . . . 108
6.4.2 Temperature . . . 109
6.4.3 Species mole fractions . . . 110
6.4.4 Soot mass fraction . . . 111
6.4.5 Radiative heat flux . . . 113
6.5 Summary . . . 116

7 Conclusions **118**
7.1 Summary of main findings . . . 118
7.2 Summary of accomplishments . . . 121
7.3 Future work . . . 122

Letter of copyright permission **124**

References **128**

List of Figures

1.1 Schematic showing the different physical processes in a pool fire. Reproduced from [1]. 2

3.1 Boundaries and trajectories evolving from start points in a TGLDM manifold. Taken from [2]. 28

3.2 TGLDM with Delaunay triangulation at the stoichiometric methane/air mixture fraction of 0.055. 29

3.3 Reaction rate of CO_2 [1/s] plotted on a TGLDM manifold with Delaunay triangulation at the stoichiometric methane/air mixture fraction of 0.055 . 30

3.4 Pressure-based spectral absorption coefficient of CO_2 in nitrogen variation with wavenumber. Reproduced from [3] 33

4.1 Schematic of the top view for UMD line burner [4]. 44

4.2 Temperature time history at z=0.25m. 45

4.3 Computational domain outline showing fuel inlet in blue, walls in green, co-flow inlet in yellow, and entrainment in red. 45

4.4 Distribution of CSE ensembles, shown on the centre plane of the LES domain 46

4.5 Comparison between the simulated flame surface defined as an iso-contour of the volumetric heat release rate of 200 kW/m^3 (left) and the experimental flame surface (right) reproduced from [5]. 49

4.6 LES instantaneous temperatures (upper) and time-averaged temperatures (lower) front view at the central (y-z) plane along the burner (left) and side-view at the central (x-z) plane across the burner (right). All distances in m. 50

4.7 Centerline profiles: left time-averaged temperatures, right corresponding rms including experimental data (symbols) and current LES-CSE results obtained with four different radiation treatments, as described in Section 4.2. 51

4.8 Cross-stream variation of the time averaged (left) and rms (right) temperature. From top to bottom, cross-stream profiles at heights 0.25 m, 0.5 m, 0.75 m, and 1 m. 53

4.9 Vertical variation of axial velocity along centerline: left time averaged values, right rms values 54

4.10 Vertical variation of mean mixture fraction along centerline: left time averaged values, right rms values 55

4.11 Centerline variation of the time averaged species mass fractions of (a) CH_4, (b) O_2, (c) CO_2, (d) H_2O, (e) CO ,and (f) H_2. 57

4.12 Conditional averages of mass fractions of CO_2, H_2O, and CO as well as temperature at 0.25, 0.5, 0.75, and 1.0 m from the inlet. 58

4.13 Comparison of centerline temperature profiles with previously published data employing EDC from Vilfayeau et al. [5], SLF from Le et al. [6], unsteady flamelet from Xu et al. [7], and CMC from Kruljevic et al. [8] combustion models. 59

5.1 Flow chart showing the solution procedure for the coupling between the CFD (LES) solver, CSE and the radiation calculation with the solution of the RTE. 67

5.2 Computational domain sectional view showing the fuel pan with the burner lip at the center, and the overall domain dimensions in meters. The fuel inlet is in grey, domain outlet in red, entrainment boundary in green, the burner walls and the ground are in blue. 70

5.3 Distribution of CSE ensembles over the computational domain 72

5.4 Comparison between the experimental flame surface (left) reproduced from [9] and the simulated flame surface defined as an iso-contour of the volumetric heat release rate of 200 kW/m^3 (right). For both the experimental and numerical snapshots high and low flames at different time instants are shown. 74

5.5 Centerline variation of the time averaged (upper) and rms (lower) temperature and axial velocity along the domain centerline. Solid lines optically thin radiation (OT), dashed-dotted lines solution of the RTE with 32 angles, and dashed lines solution of the RTE with 128 angles. Error bars represent experimental uncertainty. Vertical lines on the x-axis indicate the ensembles interfaces. Experimental data taken from Weckman and Strong [10]. 75

5.6 Radial variation of the time averaged (upper) and rms (lower) temperature, axial velocity, and radial velocity at 2 cm from the fuel surface. Experimental data taken from [10]. Same legend as in Figure 5.5. 77

5.7 Radial variation of the time averaged (upper) and rms (lower) temperature, axial velocity, and radial velocity at 6 cm from the fuel surface. Experimental data taken from [10]. Same legend as in Figure 5.5. 78

5.8 Radial variation of the time averaged (upper) and rms (lower) temperature, axial velocity, and radial velocity at 10 cm from the fuel surface. Experimental data taken from [10]. Same legend as in Figure 5.5. 79

5.9 Radial variation of the time averaged (upper) and rms (lower) temperature, axial velocity, and radial velocity at 20 cm from the fuel surface. Experimental data taken from [10]. Same legend as in Figure 5.5. 80

5.10 Radial variation of the time averaged (upper) and rms (lower) temperature, axial velocity, and radial velocity at 30 cm from the fuel surface. Experimental data taken from [10]. Same legend as in Figure 5.5. 81

5.11 Centerline variation of the time averaged species mole fractions of (a) CH_3OH, (b) O_2, (c) CO_2, (d) H_2O, (e) CO, and (f) H_2. Experimental data taken from [11]. Same legend as in Figure 5.5. 84

5.12 Estimated radiative heat flux in comparison to measured values: (a) Vertical distribution for flux in the radial direction at 0.6 m from the centerline (b) radial distribution for flux in the downward direction outside of the burner (c) radial distribution for flux in the downward direction over the pool surface. Experimental data taken from [9] except for (c) taken from [12]. Same legend as in Figure 5.5. 85

5.13 Conditional averages of mass fractions of CO_2, H_2O, and CO as well as temperature at 7.5, 22.5 and 37.5 cm from the inlet. 87

5.14 Computational domain sectional view for large scale methanol pool fire case showing the fuel pan with the burner lip at the center, and the overall domain dimensions in meters. The fuel inlet is in grey, domain outlet in red, and entrainment boundary in green. 89

5.15 Comparison between the experimental flame surface (upper) obtained from [13] and the simulated flame surface defined as an iso-contour of the volumetric heat release rate of 200 kW/m^3 (lower). For both the experimental and numerical snapshots flames at different stages are shown. 91

5.16 Vertical variation of temperature along centerline: left time-averaged values, right rms values. Experimental values taken from [13]. Error bars represent experimental uncertainty. 92

5.17 Radial variation of the time-averaged (left) and rms (right) temperature at z_p=20 cm (upper), z_p=60 cm (middle), and z_p=100 cm (lower). Experimental values taken from [13]. Error bars represent experimental uncertainty. Same legend as in Figure 5.16 94

5.18 Radial variation of the time-averaged (left) and rms (right) temperature at z_p=140 cm (upper), and z_p=180 cm (lower). Experimental values taken from [13]. Error bars represent experimental uncertainty. Same legend as in Figure 5.16 95

5.19 Estimated radiative heat flux in comparison to measured values: (a) Vertical distribution for flux in the radial direction at 2.07 m from the centerline (b) radial distribution for flux in the downward direction outside of the burner (c) radial distribution for flux in the downward direction over the pool surface. Experimental data taken from [13] except for (c) taken from [14]. 96

6.1 (a) Mixture fraction functions Eq. 6.11 and Eq. 6.12 and (b) Temperature functions for Eq. 6.11 and Eq. 6.12. In both, solid line is for soot formation and dashed line is for oxidation. 104

6.2 Sectional view of computational domain with fuel pan at the center and dimensions in meter. The fuel inlet is in grey, domain outlet in red, entrainment boundary in green, fuel pan side wall in blue and ground in yellow. . 106

6.3 Comparison between flame shapes. The left side shows the experimental flame surface, taken from reference [9]. The right side shows the simulated flame surface defined as an iso-contour of the volumetric heat release rate of 200 kW/m^3. Snapshots display high and low flames at different time instants. 109

6.4 Centerline variation of the time averaged (left) and rms (right) temperature along the domain centerline. Solid lines case without soot modelling, dashed-dotted lines solution with the first soot model, and dashed lines solution with the second soot model. Experimental data taken from [11]. 110

6.5 Centerline variation of the time averaged species mole fractions of (a) C_2H_5OH, (b) O_2, (c) CO_2, (d) H_2O, (e) CO, and (f) H_2. Experimental data taken from [11]. Same legend as in Figure 6.4. 112

6.6 Centerline variation of the time averaged soot mass fraction. Experimental data taken from [11]. Same legend as in Figure 6.4. 114

6.7 Estimated radiative heat flux in comparison to measured values: (a) Vertical distribution for flux in the radial direction at 0.6 m from the centerline (b) radial distribution for flux in the downward direction outside of the burner (c) radial distribution for total heat feedback over the pool surface. Experimental data taken from [9]. Same legend as in Figure 6.4. 115

List of Tables

4.1 Previous studies with modelling approaches 43

4.2 Duration, approximate time step and CPU time for current work and previously published studies, whenever available. 60

5.1 Previous studies with modelling approaches 69

6.1 Soot formation and oxidation function parameters for the second soot model from [15] 103

Chapter 1

Introduction

1.1 Overview

Combustion processes are encountered in various aspects of daily life, often taking diverse forms. Among these, are turbulent buoyant diffusion flames, commonly observed in fires, represent a significant area of concern. Fires pose a substantial threat to public safety resulting in considerable loss of life and property. Avoiding such losses encourages the development of new analysis tools to well predict the fire behavior [16]. Relying on computer simulations is a key element in analyzing fire scenarios that are too difficult or too expensive to perform experimentally. Simple models such as the two-zone CFAST model can provide quick predictions with low computational costs [17]. However, such models lack the accuracy and the details required to capture all the processes of the fire phenomena. In recent years, there has been continuous progress in the available computational power allowing for better models to be employed. The development of computational fluid dynamics (CFD) approaches relying on the large eddy simulation (LES) turbulence treatment is, therefore, the current trend in the fire analysis field [18].
Fires are different from controlled combustion in the fact that the amounts of fuel and oxidizer feeding the fire are out of control and are sustained by the surrounding environment. In most cases, fires are turbulent diffusion flames driven by buoyancy. Many complex interacting physical phenomena are encountered in fires such as turbulence, complex chemical reactions, radiation, soot formation, transient flame spread and pyrolysis. A schematic showing the different physical processes involved in pool fires is shown in Figure 1.1. Also, additional complexities can be encountered depending on the fire scenario such as flame extinction and reignition as in under-ventilated fires, suppression with water, and wind

effects.

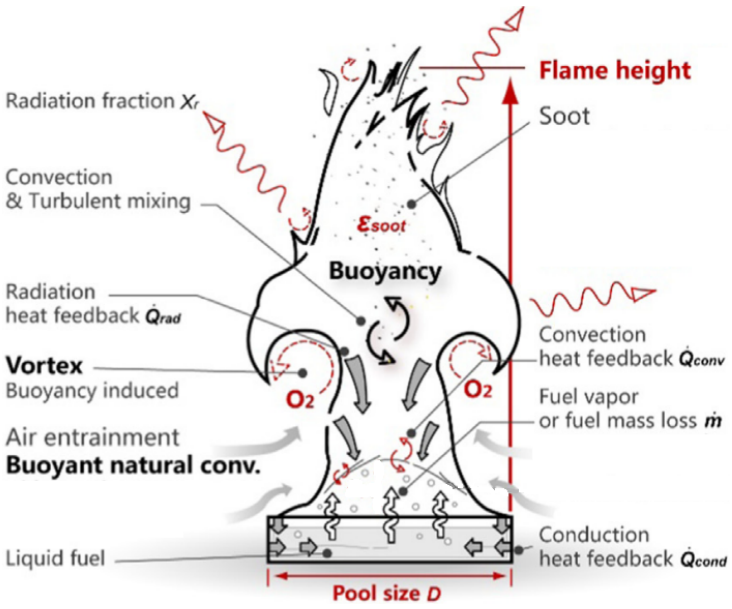


Figure 1.1: Schematic showing the different physical processes in a pool fire. Reproduced from [1].

Pool fires correspond to one of the generic configurations in fire analysis [19]. In pool fires, the fuel inlet is well-defined by either being a gas or a flat horizontal liquid surface, providing a simple configuration to test CFD models. Also, pool fire cases remove some complexities found in real fires related to flame spread and pyrolysis. Furthermore, depending on the type of fuel chosen, soot modeling may be avoided. For example, methane and methanol fire cases are non-sooting [20, 4], while heptane is a sooty fuel [21]. In addition, liquid pool fires provide a test bed to study gas to liquid thermal feedback that controls the fuel loss rate and the overall flame size. Pool fires also represent real-world fire hazards that exist in the case of leakages from fuel tanks at homes or in transportation accident scenarios. Large scale pool fires are also encountered in industrial accidents leading to severe air pollution and may trigger more serious cascading effects leading to losses in human lives and material properties.
In pool fires, the rate of fuel loss from the liquid pool that sustains the fire is controlled by the heat feedback from the flame region. The two main modes of the heat feedback are the convective and radiative feedback to the pool surface. The dominant mode among them varies according to the pool size. In small scale pool fires, the dominant mode is the convective feedback, while in large scale ones, which are bigger than one meter in diam-

eter, the radiative mode is dominant [22]. In addition, the increase of pool size leads to a reduction in the combustion efficiency and consequently, higher soot yield if the fuel is among the sooty hydrocarbons [19].

To simulate turbulent flows, several approaches can be used to solve the governing equations. Turbulent flows are characterized by the presence of eddies with different scales. The most accurate approach is the direct numerical simulation (DNS) where all the turbulent flow scales are resolved. However, DNS is limited to simple cases due to the associated high computational costs [23]. In contrast, the Reynolds Averaged Navier-Stokes (RANS) approach models all turbulent scales. RANS techniques have been shown to provide acceptable results with a significant reduction in computational costs compared to DNS.

The LES approach is a major improvement over RANS. Instead of modeling all the turbulent scales, LES captures the large-scale dynamics that are affordable to be resolved and models the effects of only the subfilter smaller scales. Thus, a better solution accuracy than RANS is obtained, while still at a much lower computational cost than required by DNS. In the fire community, the two most widely used CFD packages in fire modeling are the Fire Dynamics Simulator (FDS) [24] and FireFOAM [25]. Both of these packages use the LES approach in the treatment of turbulence. The advantage of LES in fire modeling over RANS is being capable of handling highly unsteady motions, and it is challenging to model all the turbulent scales correctly with RANS due to the buoyancy generated turbulence. The flame intermittent region exhibits strong fluctuations due to the puffing behaviour leading to periodic shedding [26]. However, in flows involving chemical reactions, turbulence-chemistry interactions require additional modeling considerations, as the chemical source term is a highly non-linear function in the flow variables. Thus, turbulent combustion models are developed to close the chemical source term.

In fire analysis, the most popular combustion models are those based on the eddy break-up model [27] like the eddy dissipation model (EDM) [28] and the eddy dissipation concept (EDC) [29] which are widely used due to their simplicity. However, there are constants in these models that require calibration in a case by case basis. In addition, such approaches rely on single step chemistry neglecting detailed chemical kinetics which are crucial for accurately simulating complex fire phenomena, including the tracking of minor species, flame extinction and soot production. Another set of methods relies on the filtered density function (FDF). Unlike the EDM and EDC techniques, these methods determine the reaction rate through correlations rather than direct modeling and can include detailed chemical kinetics. Techniques such as the laminar flamelet [30, 31], the conditional moment closure [32], and the conditional source term estimation [33] fall into this category. Still, these methods have seen limited application in fire analysis [7, 8, 34] compared to the EDM/EDC models.

The Conditional Source term Estimation (CSE) combustion model is adopted in the current

work. CSE offers many advantages compared to other combustion models. The method is more sophisticated than simple ones which are usually used in fire modeling. In addition, it allows the inclusion of detailed chemical kinetics. Moreover, CSE does not require the solution of additional transport equations to calculate reaction rates unlike comparable approaches such as the conditional moment closure model [35]. The approach has been successful in simulating different combustion regimes and configurations of premixed [36], non-premixed [37, 38], and partially premixed [39] flames. The current work builds upon recent advances in CSE combustion modeling and adopts the model for fire simulation for the first time.

Radiative heat transfer modeling is of major importance in analysis of fires. In medium scale pool fires, the fraction of thermal power emitted as radiation can be 20-30% of the total heat release rate [40]. In addition, radiation is a major contributor to the total heat feedback to the fuel surface in liquid pool fires. For a 0.3 meter diameter pool fire, the radiative heat feedback reaches 55%, 80%, and 96% for methanol, heptane, and toluene, respectively of the total heat feedback [12]. This contribution increases with increasing pool size and soot level. The radiation problem involves the solution of the radiative transfer equation (RTE) for a number of wavelengths. The finite volume discrete ordinate method is the typical RTE solver used with CFD calculations due to its compatibility with fluid dynamics discretization and accuracy [3]. The model is available in both FDS and FireFOAM software packages and is adopted for simulations of pool fires by many authors [5, 7, 20, 21, 41, 42, 43]. In addition, a suitable absorption-emission model is required to account for the non-grey nature of the combustion gases which can have up to a million absorption lines. Line-by-line methods are available, but they are computationally prohibitive to be used in CFD simulations [42]. Global models such as the weighted sum of grey gases (WSGG) are more appropriate to be coupled with CFD simulations.

Under certain conditions, the combustion of hydrocarbons can produce soot, which is composed of masses that consist mainly of carbon particles. Soot is a key component of smoke from fires, which not only reduces visibility and complicates evacuation during fire incidents but also leads to respiratory diseases and environmental pollution. Furthermore, smoke shielding in large hydrocarbon fires traps emitted radiation, influencing the overall fire dynamics [44, 45, 46]. Soot formation is a complicated process and remains one of the most challenging aspects in modeling flows involving combustion due to the complex steps involved. Over the years, many attempts have been made to accurately model soot in CFD simulations of combustion scenarios [47]. Detailed soot models rely on complex reaction mechanisms, but these are difficult to develop due to the complexity of the required measurements [48]. In contrast, smoke point-based models offer a practical and computationally efficient solution. In this approach, soot formation is assumed to be a function of the measured laminar smoke point height, which indicates the sooting propensity of a

given fuel. Two of the most widely used soot models in fire analysis are based on the laminar smoke point concept [49, 15].

1.2 Objectives

The objective of the current research is to develop a LES approach for fire analysis using more detailed models for combustion and radiation compared to existing fire modeling approaches. The model is to be validated against a series of experimental pool fires to test its accuracy in predicting temperature profiles, radiative heat fluxes and species mole fractions. CSE has been applied to both RANS and LES to simulate a wide range of combustion problems such as premixed flames, non-premixed flames, lifted flames, and combustion with sprays [36, 37, 39, 2, 50, 33, 51]. However, CSE was never considered before for buoyant diffusion flames such as fires. LES is the main approach in the current work, as the flow is buoyancy driven and highly unsteady. Also, only simple radiation models have been coupled before with CSE relying on the optically thin approximation that neglects absorption. In the proposed research, a more accurate radiation model that accounts for absorption will be coupled with CSE for the first time by solving the radiative transfer equation (RTE) with the finite-volume discrete ordinate method and estimating the absorption coefficients using the WSGG model. Moreover, the new framework is to be expanded to include soot modeling using CSE in turbulent buoyant diffusion flames for the first time. Pool fire cases will be investigated with different fuels such as methane, methanol and more complex ones such as ethanol. It is proposed in this research to account for detailed chemical kinetics using chemistry tabulation. Numerical predictions of various quantities, including temperature, velocity, species mole fractions, flame shape, and radiative heat flux, will be compared with experimental measurements and previously published numerical results from other groups investigating the same cases using different turbulent combustion models. The main objectives of this study are summarized as follows:

1. **Coupling CSE with FireFoam solver and validation with the University of Maryland line burner case.**

   CSE is coupled with the FireFOAM solver for the first time and tested for LES of a fire case by simulating the University of Maryland line burner methane case. The Smagorinsky model for subgrid-scale turbulence is selected. The reaction rates are tabulated using GRI-MECH 3.0 mechanism. Different treatments for radiation that rely on the optically thin radiation are considered. The results are compared with available experimental measurements as well as previously published simulations for

the same case. A paper presenting the numerical results and conclusions is published in a peer reviewed journal [52].

2. **Inclusion of radiation absorption effects with the solution of RTE in LES-CSE simulation of methanol pool fires.**

   Previously, CSE has been coupled with only optically thin radiation model that neglects absorption. Thus, the next step is expanding the CSE framework by accounting for radiation absorption through solution of the RTE. Moreover, the WSGG model is considered for estimating the absorption coefficients instead of the RADCAL model. The new modeling approach is tested by simulating a medium and large scale methanol pool fires. The methanol pool fire cases are well studied experimentally and there are several measurements for the temperature, velocity, and species mole fractions distributions available. The numerical results are validated using available experimental measurements. A paper presenting the numerical predictions and findings is submitted to a peer reviewed journal.

3. **Expanding the framework by inclusion of soot modeling and applying the new modeling approach to an ethanol pool fire.**

   The new CSE framework is expanded to include soot modeling. Two of the most commonly used soot models in fire simulations that are based on the laminar smoke point concept are coupled with CSE for the first time. The new approach is applied for investigating an ethanol pool fire, which was never simulated previously. The numerical results are compared with available measurements of temperature, soot mass fraction, species mole fractions and radiative flux at different locations. A paper describing the new framework and the findings is submitted to a peer reviewed journal.

1.3 Thesis outline

Chapter 2 discusses the governing equations and the turbulence treatment required for fire modeling. In Chapter 3, the turbulent combustion modeling with a focus on CSE approach and radiative heat transfer analysis techniques is described in addition to reviewing soot formation and modeling techniques. Chapter 4 presents the conducted simulations of the University of Maryland line burner including the experimental configuration, the numerical solver details, the computational configuration and comparison of the results with the experimental data as well as previously published results. Chapter 5 demonstrates the

coupling between CSE and solution of RTE to account for radiation absorption. The new framework is applied to investigate medium and large scale methanol pool fires. Chapter 6 discusses the introduction of soot modeling to the CSE framework and investigation of a medium scale ethanol pool fire. Finally, conclusions and proposed future work of the current dissertation are presented in Chapter 7.

1.4 Author's current contributions

It is acknowledged that parts of the content presented in Chapters 4-6 are published in the following articles or under review

- Ahmed MK Abdalhamid and Cecile Devaud. Large eddy simulations of a buoyant turbulent line flame using conditional source-term estimation (CSE). Combustion Theory and Modelling, 2023.
- Ahmed MK Abdalhamid, Cecile Devaud and Elizabeth Weckman. Development of the Conditional Source-term Estimation (CSE) framework including finite-rate kinetics and non-prescribed radiation applied to a methanol pool fire. Fire Safety Journal, under review, 2024.
- Ahmed MK Abdalhamid, Cecile Devaud and Elizabeth Weckman. Large eddy simulations of a medium-scale ethanol pool flame using Conditional Source-term Estimation including coupled soot radiation effects. Combustion Science and Technology, under review, 2024.
- Ahmed MK Abdalhamid, Cecile Devaud and Elizabeth Weckman. Pool fire simulation using Conditional Source-term Estimation (CSE) approach coupled with solution of the radiative transfer equation (RTE). Proceedings of Combustion Institute/Canadian Section Spring Technical Meeting, Queen's University, May 13 - 16, 2024.
- Ahmed MK Abdalhamid and Cecile Devaud. Large eddy simulations of a medium-scale methanol pool fire. Proceedings of Combustion Institute/Canadian Section Spring Technical Meeting, University of Alberta, May 15 - 18, 2023.
- Ahmed MK Abdalhamid and Cecile Devaud. Large eddy simulations of a turbulent line burner using Conditional Source-term estimation (CSE) approach. Proceedings of Combustion Institute/Canadian Section Spring Technical Meeting, University of Ottawa, May 16 - 19, 2022.

Chapter 2

Background

This chapter presents the background related to fire modeling. First, the chapter starts with governing equations. Next, the turbulence treatment methods are presented with an emphasis on large eddy simulation. The unclosed terms in the equations are discussed along with their treatment.

2.1 Governing Equations

Any reacting fluid flow is governed by transport equations that describe the evolution of the different flow variables. A solution for transport equations of mass, momentum, enthalpy (energy) and species mass fractions is required for simulating turbulent flames. The mass transport (continuity) equation is written as

$$\frac{\partial \rho}{\partial t} + \frac{\partial (\rho u_i)}{\partial x_i} = S_{\delta,eva}, \tag{2.1}$$

where ρ is the fluid density, u_i is the velocity component in the i-direction, and the source term $S_{\delta,eva}$ represents mass addition to the gaseous phase flow, for example due to the evaporation of liquid film or liquid droplets in cases of fire suppression with water.
The momentum conservation is given by

$$\frac{\partial (\rho u_j)}{\partial t} + \frac{\partial (\rho u_i u_j)}{\partial x_i} = -\frac{\partial p}{\partial x_j} + \frac{\partial \tau_{ij}}{\partial x_i} + F_{b,j}, \tag{2.2}$$

where p is the pressure and τ_{ij} represents the viscous stresses. The source term $F_{b,j}$ in Eq. 2.2 accounts for the effects of external forces. In the current work, forces arising from

external fields or spray particles are not present, thus, they are not accounted for. Only gravitational force is considered to model buoyancy effects. Consequently, the source term is written as

$$F_{b,j} = \rho g_j. \tag{2.3}$$

The viscous stresses are expressed as a function of the strain rate tensor S_{ij} such that

$$\tau_{ij} = \mu \left[2S_{ij} - \frac{2}{3}\delta_{ij}\frac{\partial u_k}{\partial x_k} \right]. \tag{2.4}$$

The species conservation equation is written as

$$\frac{\partial(\rho Y_k)}{\partial t} + \frac{\partial(\rho u_i Y_k)}{\partial x_i} = \frac{\partial J_{k,i}}{\partial x_i} + \dot{\omega}_k + \dot{\rho}_k, \tag{2.5}$$

where Y_k is the mass fraction of species k, $J_{k,i}$ is the diffusive flux of species k, $\dot{\omega}_k$ is the rate of production or destruction of species k due to chemical reactions, and $\dot{\rho}_k$ is a source term accounting for evaporation from liquid phase to gas phase, if present. The diffusive flux is defined using Fick's law as

$$J_{k,i} = \rho D_k \frac{\partial Y_k}{\partial x_i}, \tag{2.6}$$

and D_k is the molecular diffusivity of species k.
The conservation of energy is written in terms of the sensible enthalpy $h = e + p/\rho$, where e is the internal energy, as

$$\frac{\partial(\rho h)}{\partial t} + \frac{\partial(\rho u_i h)}{\partial x_i} = -\frac{\partial q_i}{\partial x_i} + \dot{Q}_{react} + \dot{Q}_{rad} + \dot{Q}_{liq} + \frac{\partial p}{\partial t} - \rho g_i u_i + \frac{\partial(u_i \tau_{ij})}{\partial x_i}, \tag{2.7}$$

where q_i is the energy flux given by $q_i = -\lambda\frac{\partial T}{\partial x_i} - \rho\sum_{k=1}^{n} h_k D_k \frac{\partial Y_k}{\partial x_i}$ by accounting for heat conduction using Fourier's law and energy flux due to diffusion using Fick's law while λ is the thermal conductivity. Using the definitions of Schmidt and Prandtl numbers and assuming a unity Lewis number for all species $Le = \frac{\lambda}{\rho c_p D} = 1$ the term is simplified [53] to

$$q_i = -\rho\frac{\nu}{Pr}\frac{\partial h}{\partial x_i}. \tag{2.8}$$

The terms $\dot{Q}_{react}, \dot{Q}_{rad}$ and $\dot{Q}_{liq}$ are source terms accounting for chemical reactions, radiation, and the heat exchange with the liquid phase, respectively. The temporal pressure variation, the work produced by gravitational forces and the energy produced by viscous shear stresses and by normal stresses are all negligible in fire applications [53].

2.2 Turbulent Flows

Equations 2.1, 2.2, 2.5 and 2.7 are the partial differential equations (PDEs) that govern any multicomponent reacting system including either laminar or turbulent flows. However, solving these equations numerically requires a fine resolution to capture all the spatial and temporal scales. This is called Direct Numerical Simulation (DNS) which, for turbulent cases, requires huge computational resources to capture all the turbulent scales down to the Kolmogorov length scale. Such solution is not feasible for practical turbulent flows. Consequently, not all of the turbulent scales can be resolved.
The other two approaches that are usually adopted to account for the influence of unresolved turbulent fluctuations on the resolved ones are the Reynolds Averaged Navier Stokes (RANS) and Large Eddy Simulation (LES) approaches. In RANS, all the turbulent fluctuations are modeled using a turbulence model to provide a closure for the unclosed terms in the averaged equations that accounts for the influence of such fluctuations on a defined local mean. In contrast, LES resolves the portion of larger scales that are computationally affordable to be solved and models the effect of the smaller scales beyond the filter. Therefore, LES serves as a compromise between the DNS and RANS approaches.

2.2.1 Direct numerical simulation

In DNS approach, all of the turbulent scales are simulated with no need for modeling any sub-grid fluctuations. This requires a very fine resolution in space and time deeming such approach impractical to simulate real life scenarios with the current computational capabilities. In addition, the computational cost with DNS increases rapidly with Reynolds number which limits its applicability to flows with low or moderate Reynolds numbers. Still, simplifications can be made to model specific cases that provide insight into elementary ingredients of the flow physics which are inaccessible to experiments [54].
The simulation of reacting flows with DNS is also more problematic than that of non-reacting flows. For instance, the large number of species involved in a chemical scheme is an additional computational load that is hard to handle for such fine time and space resolutions. Moreover, the chemical time and length scales are usually even smaller than that of the smallest turbulent scales. Consequently, DNS is not practical for fire modeling with the current computational capabilities except for some special cases. [53].

2.2.2 RANS approach and Favre-averaging

In RANS, the instantaneous transport equations are averaged to obtain balance equations for the mean quantities. Each variable ϕ is split into a mean component $\overline{\phi}$ and the deviation from the mean ϕ' as

$$\phi = \overline{\phi} + \phi', \tag{2.9}$$

where $\overline{\phi'} = 0$.
Reynolds decomposition and time-averaging as shown in Eq. 2.9 is suitable for incompressible flows where the density variations are small and fluctuations are encountered in velocity and pressure only. In flows with variable density such as high speed flows and flows involving combustion, the density fluctuations add additional terms that require closure. For example, after applying the Reynolds decomposition and time averaging on the continuity equation, the term $\overline{\rho' u'}$ appears in the equation, and so a correlation is required to achieve closure. This gets more complicated with the momentum and energy equations where triple correlations arise involving the density fluctuations. An alternative approach is to introduce a density-weighted averaging technique named Favre average [55] as

$$\phi = \tilde{\phi} + \phi'', \tag{2.10}$$

where

$$\tilde{\phi} = \frac{\overline{\rho\phi}}{\overline{\rho}}. \tag{2.11}$$

The RANS averaging procedure introduces new unclosed terms in the equations which require modeling to provide closure. This is accomplished by introducing turbulence models such as the $k-\epsilon$ [56] and $k-\omega$ [57]models.

2.2.3 Large eddy simulation

In LES, all the large scale eddies are resolved and only the small scale ones are modeled. Also, the effect of turbulent small-scales, beyond the filter width, are represented by a subgrid-scale (sgs) model [58].
LES is carried out by performing a filtering process through which the velocity is decomposed into a resolved component and a sub-grid component

$$U(x,t) = \overline{U}(x,t) + u'(x,t). \tag{2.12}$$

Although the Eq. 2.12 looks similar to Eq. 2.9, here the average of the sub-grid velocity is not equal to zero

$$\overline{u'}(x,t) \neq 0. \tag{2.13}$$

The large scale component is separated by carrying out the filtering process as

$$\overline{U}(x,t) = \int U(x',t)G(x-x')dx', \tag{2.14}$$

where G represents the LES filter. There are several types of filters in spectral and physical spaces such as the cut-off filter, the gaussian filter and the box filter defined as

$$G(x) = G(x_1,x_2,x_3) = \begin{cases} 1/\Delta^3 & \text{if } |x_i| \leq \Delta/2, i = 1,2,3 \\ 0 & \text{otherwise} \end{cases}, \tag{2.15}$$

where Δ is the filter size. This filter performs the averaging over a cubic box of size Δ. As with RANS approach, the Favre filtering is adopted for deriving the filtered governing equations for variable density cases

$$\tilde{U}(x,t) = \frac{1}{\rho}\int \rho U(x',t)G(x-x')dx'. \tag{2.16}$$

The transport equations are then obtained by filtering the governing transport equations resulting in:

- The Favre filtered continuity equation

$$\frac{\partial \overline{\rho}}{\partial t} + \frac{\partial(\rho\tilde{u}_i)}{\partial x_i} = 0. \tag{2.17}$$

- The Favre filtered conservation of momentum equation

$$\frac{\partial(\overline{\rho}\tilde{u}_j)}{\partial t} + \frac{\partial(\overline{\rho}\tilde{u}_i\tilde{u}_j)}{\partial x_i} = -\frac{\partial \overline{p}}{\partial x_j} + \frac{\partial}{\partial x_i}(\overline{\tau_{ij}} - \overline{\rho}(\widetilde{u_iu_j} - \tilde{u}_i\tilde{u}_j)) + \overline{F_{b,j}}. \tag{2.18}$$

- The Favre filtered species conservation equation

$$\frac{\partial(\overline{\rho}\tilde{Y_k})}{\partial t} + \frac{\partial(\overline{\rho}\tilde{u}_i\tilde{Y_k})}{\partial x_i} = \frac{\partial}{\partial x_i}(\overline{\rho D_k \frac{\partial Y_k}{\partial x_i}}) - \frac{\partial}{\partial x_i}[\overline{\rho}(\widetilde{u_iY_k} - \tilde{u}_i\tilde{Y_k})] + \overline{\dot{\omega}_k}. \tag{2.19}$$

- The Favre filtered energy conservation equation

$$\begin{aligned}\frac{\partial(\overline{\rho}\tilde{h})}{\partial t}+\frac{\partial(\overline{\rho}\tilde{u_i}\tilde{h})}{\partial x_i}=\\ =-\frac{\partial}{\partial x_i}[\overline{\rho}(\widetilde{u_i h}-\tilde{u_i}\tilde{h})]+\frac{\partial}{\partial x_i}(\overline{\rho\frac{\nu}{Pr}\frac{\partial h}{\partial x_i}})+\overline{\dot{Q}_{react}}+\overline{\dot{Q}_{rad}}.\end{aligned} \tag{2.20}$$

The unresolved Reynolds stresses term ($\tau_{ij}^{sgs}=\widetilde{u_iu_j}-\tilde{u_i}\tilde{u_j}$) is commonly modeled using Boussinesq's eddy viscosity concept

$$\tau_{ij}^{sgs}=-\nu_{sgs}(\frac{\partial\tilde{u_i}}{\partial x_j}+\frac{\partial\tilde{u_j}}{\partial x_i}-\frac{2}{3}\delta_{ij}\frac{\partial\tilde{u_k}}{\partial x_k})+\frac{2}{3}k_{sgs}\delta_{ij}, \tag{2.21}$$

where ν_{sgs} is the sub-grid viscosity and k_{sgs} is the sub-grid turbulent kinetic energy. There are several models that can be employed to model the sub-grid viscosity such as the widely used Smagorinsky model [59] and the one equation eddy viscosity model [60]. In the Smagorinsky model, ν_{sgs} is calculated as

$$\nu_{sgs}=(C_s\Delta)^2(2\widetilde{S_{ij}}\widetilde{S_{ij}})^{1/2}, \tag{2.22}$$

where C_s is a model constant, Δ is the filter width, and $\widetilde{S_{ij}}=\frac{1}{2}(\frac{\partial\tilde{u_i}}{\partial x_j}+\frac{\partial\tilde{u_j}}{\partial x_i})$ is the resolved rate of strain tensor. The one-equation eddy viscosity model calculates ν_{sgs} as

$$\nu_{sgs}=C_k\Delta\sqrt{k_{sgs}}, \tag{2.23}$$

where k_{sgs} is the sub-grid turbulent kinetic energy found by solving the transport equation:

$$\frac{\partial(\overline{\rho}k_{sgs})}{\partial t}+\frac{\partial(\overline{\rho}\tilde{u_i}k_{sgs})}{\partial x_i}=\frac{\partial}{\partial x_i}\left(\overline{\rho}\left(D+D_t\right)\frac{\partial k_{sgs}}{\partial x_i}\right)-\overline{\rho}\tau_{ij}^{sgs}\frac{\partial\tilde{u_i}}{\partial x_j}-C_\epsilon\overline{\rho}\frac{k_{sgs}\sqrt{k_{sgs}}}{\Delta}, \tag{2.24}$$

where C_k and C_ϵ are model constants. Since only the small scales are modeled in LES, the modeling of the buoyancy effects on turbulence is not an issue as with RANS [53] which is also verified numerically [61].
The unresolved species and enthalpy fluxes are closed using the gradient hypothesis as

$$(\widetilde{u_iY_k}-\tilde{u_i}\tilde{Y_k})=-\frac{\nu_t}{Sc_t}\frac{\partial\tilde{Y_k}}{\partial x_i}, \tag{2.25}$$

$$(\widetilde{u_i h} - \tilde{u}_i \tilde{h}) = -\frac{\nu_t}{Pr_t}\frac{\partial \tilde{h}}{\partial x_i}. \tag{2.26}$$

where Sc_t and Pr_t are the subgrid-scale Schmidt and Prandtl numbers specified depending on each case.
The molecular and enthalpy diffusion fluxes are closed as

$$\overline{\rho D_k \frac{\partial Y_k}{\partial x_i}} = \overline{\rho}\frac{\nu}{Sc}\frac{\partial \tilde{Y_k}}{\partial x_i}, \tag{2.27}$$

$$\overline{\rho \frac{\nu}{Pr}\frac{\partial h}{\partial x_i}} = \overline{\rho}\frac{\nu}{Pr}\frac{\partial \tilde{h}}{\partial x_i}. \tag{2.28}$$

The remaining terms to be modeled are the reaction rate term $\overline{\dot{\omega}_k}$ in the species equation and the radiation source term $\overline{\dot{Q}_{rad}}$ in the energy equation which will be discussed in the next chapter.
In fire analysis, LES is the most common approach rather than RANS since the fire behavior is highly unsteady, and it is challenging to model all the turbulent scales correctly due to the buoyancy generated turbulence. The flame intermittent region exhibits strong fluctuations due to the puffing behavior. The periodic shedding produced enhances the turbulence near the fire source and is, therefore, a key element in fire dynamics as it controls the air entrainment in the reaction zone. In turn, the heat release rate, the products composition, and all associated physics such as the soot generation are related to the accurate representation of turbulence [26]. In addition, turbulence models are altered by buoyancy in the RANS approach and requires additional tweaking while this is not the case with LES.

2.3 Summary

In this chapter, the governing equations required to provide a solution for reacting fluid flows as in fires are discussed. The transport equations that describe the evolution of flow variables of mass, momentum, species mass fraction and enthalpy are presented. Since most of the engineering flows are turbulent which is also the case with fires that are classified as turbulent buoyant diffusion flames, the different numerical techniques for turbulence treatment are discussed such as RANS, LES and DNS. The LES approach is given in more details since this is the method adopted in the current study as well as most of the previous CFD fire simulations. The Favre-filtered form of the governing equations are shown. In the equations, there are some unclosed terms that require modeling. The closure of such

terms are presented. The remaining terms that require closure are the species reaction rate and the radiation terms, which are discussed in the next chapter.

Chapter 3

Turbulent combustion and radiation modeling

This chapter discusses the additional modeling steps required for modeling flows involving reactions and heat transfer. First, the chapter starts with the different modeling approaches for closure of mean chemical source term. Second, the radiation treatment methods are presented. In the end, soot formation steps and modeling techniques in CFD are reviewed.

3.1 Turbulent combustion models

According to the law of mass action and Arrhenius form for the rate coefficients, the chemical source term is a highly non-linear function in the flow variables. Consequently, the mean quantities obtained from RANS or the filtered ones from LES cannot be used to estimate the averaged chemical source term as

$$\overline{\dot{\omega}(Y_k, T, \rho)} \neq \dot{\omega}(\tilde{Y}_k, \tilde{T}, \overline{\rho}). \tag{3.1}$$

Thus, turbulent combustion models are developed to close the chemical source term in turbulent flows involving chemical reactions modeled with RANS or LES. The modeling strategies are based on physical assumptions, therefore, they are dependent on the type of flame under consideration. In the non-premixed flames such as fires, the most popular models are those based on the eddy break-up model such as the eddy dissipation model (EDM) [28] and the eddy dissipation concept (EDC) [29]. Another class of methods is based on the presumed filtered density function (FDF). In these methods, the reaction rate is

found through correlations and is not modeled as with the EDM and EDC. The reactive scalars (temperature and species) are related to the mixture fraction through the FDF. One approach is to solve for the transport of FDF, but this is a computationally expensive approach. Instead, the FDF can be presumed and modeled through other transported or modeled variables such as the mixture fraction and its variance. Methods such as the laminar flamelet [30, 31], the conditional moment closure [32], and the conditional source term estimation [33] fall under this category.

3.1.1 Eddy break up model

The eddy break up (EBU) model [62, 27] is one of the early proposed models for turbulent combustion modeling. The model relies on the infinitely fast chemistry assumption that the chemistry time scale can be considered much smaller in comparison to the turbulence time scale. Therefore, the turbulent mixing rather than the chemistry is the rate determining process. The mean/filtered reaction rate is considered to be controlled by the variance of the product mass fraction $\widetilde{Y_p''^2}$ and a characteristic turbulent time τ_{EBU} as

$$\overline{\dot{\omega}_p} = \overline{\rho} C_{EBU} \frac{\sqrt{\widetilde{Y_p''^2}}}{\tau_{EBU}}, \tag{3.2}$$

where C_{EBU} is a model constant of the order of unity, and the characteristic turbulent time can be estimated from the turbulence kinetic energy k and its dissipation rate ϵ as

$$\tau_{EBU} = k/\epsilon. \tag{3.3}$$

The major advantage in the model is that it estimates the reaction rate based on simple relation obtained from known flow variables, making it easy to implement with any CFD code. However, the model does not account for any effects from chemical kinetics. Also, the model dependency on the ratio k/ϵ causes the reaction rate to be overestimated in highly strained regions.

3.1.2 EDM and EDC models

The EDM model is based on the EBU model. It applies the same formulation but replaces the variance of the product mass fraction with the mass fraction of the deficient species which would be the fuel or oxidizer depending on whether the mixture is lean or rich. The model estimates the mean/filtered reaction rate as the minimum of three rates as

$$\overline{\dot{\omega}_p} = \overline{\rho} C_{EDM1} \frac{\epsilon}{k} min(\widetilde{Y_F}, \frac{\widetilde{Y_{O_2}}}{s}, C_{EDM2} \frac{\widetilde{Y}_p}{1+s}), \tag{3.4}$$

where s is the stoichiometric oxygen to fuel mass ratio, C_{EDM1} and C_{EDM2} are model constants that require adjustments depending on the case, $\widetilde{Y_F}$ and $\widetilde{Y_{O_2}}$ are the Favre averaged/filtered mass fractions of the fuel and oxidizer respectively.
Another variation of the model is the eddy dissipation concept (EDC) [29] which assumes that the chemical reactions occur in small turbulent structures called the fine scales. The model calculates the reaction rate as

$$\overline{\dot{\omega}_p} = \overline{\rho} \frac{\gamma^2 \chi}{\tau_{EDC}(1-\gamma^3 \chi)} min(\widetilde{Y_F}, \frac{\widetilde{Y_{O_2}}}{s}), \tag{3.5}$$

where γ is the fine scale size, τ_{EDC} is mixing time scale for EDC model, χ is fine structures reactive part. The fine structure size and mixing time are modeled based on the turbulence scale relations with additional model constants for tuning. The model can be modified to include detailed chemistry by assuming that reactions take place in the fine scales, where chemical rates can be integrated numerically over the mixing time scale.

3.1.3 Mixture fraction

In non-premixed (diffusion) combustion, the fuel and oxidizer enter the combustion region from separate streams. Thus, the reactants need to mix first before combustion can take place. Moreover, the chemical time scale is small compared to the mixing time scale, meaning that it is safe to assume that combustion is mixing controlled. A scalar named the mixture fraction, Z, is defined to express the state of mixing. The mixture fraction is defined to have a value of 1 in the fuel stream and 0 in the oxidizer stream and between the two limits is defined by Bilger [63] as

$$Z = \frac{Y_i - Y_{i,O}}{Y_{i,F} - Y_{i,O}}, \tag{3.6}$$

where Y_i is the local mass fraction of element i at a given location, $Y_{i,O}$ and $Y_{i,F}$ is the mass fraction of element i in the oxidizer and fuel streams, respectively. The mixture fraction defines the local amount of mass that originated from the fuel side to the total mass originating from both the fuel and oxidizer sides. It acts as an inert tracer introduced to the flow with the fuel [32]. Therefore, the mixture fraction is a conserved scalar, meaning that there is no source term in its transport equation except if a mass source such as droplet

evaporation exists. The transport equation for the Favre-filtered mean mixture fraction can be written as

$$\frac{\partial \overline{\rho}\tilde{Z}}{\partial t} + \frac{\partial(\overline{\rho}\tilde{u}_i\tilde{Z})}{\partial x_i} = \frac{\partial}{\partial x_i}(\overline{\rho D \frac{\partial Z}{\partial x_i}}) - \frac{\partial}{\partial x_i}[\overline{\rho}(\widetilde{u_i Z} - \tilde{u}_i\tilde{Z})]. \tag{3.7}$$

The unclosed turbulent flux can be closed using the gradient approach similar to what was done before with the species equation as

$$(\widetilde{u_i Z} - \tilde{u}_i\tilde{Z}) = -\frac{\nu_t}{Sc_t}\frac{\partial \tilde{Z}}{\partial x_i}. \tag{3.8}$$

The Favre-filtered mean mixture fraction is not sufficient by itself for reaction rates estimation. The subgrid mixture fraction variance $\widetilde{Z''^2}$ at each cell is required as well. There are different ways to calculate $\widetilde{Z''^2}$. For example, the gradient model [64] provides a simple expression

$$\widetilde{Z''^2} = C_Z \Delta^2 \frac{\partial \tilde{Z}}{\partial x_i}\frac{\partial \tilde{Z}}{\partial x_i}, \tag{3.9}$$

where C_Z is a constant and Δ is the filter size calculated as the cubic root of the cell volume.
Instead, a Favre-filtered transport equation [39] can be solved to calculate $\widetilde{Z''^2}$ as

$$\frac{\partial \overline{\rho}\widetilde{Z''^2}}{\partial t} + \frac{\partial(\overline{\rho}\tilde{u}_i\widetilde{Z''^2})}{\partial x_i} = \frac{\partial}{\partial x_i}(\overline{\rho D \frac{\partial Z''^2}{\partial x_i}}) - \frac{\partial}{\partial x_i}[\overline{\rho}(\widetilde{u_i Z''^2} - \tilde{u}_i\widetilde{Z''^2})] + 2\frac{\mu}{Sc_t}\frac{\partial \tilde{Z}}{\partial x_i}\frac{\partial \tilde{Z}}{\partial x_i} - \overline{\rho}\tilde{\chi}, \tag{3.10}$$

where the first two terms on the right hand side are closed using the gradient assumption. The filtered scalar dissipation rate ($\tilde{\chi}$) is modeled as a function of the subgrid turbulent kinetic energy ($\tilde{k}$) and subgrid dissipation rate($\tilde{\epsilon}$) as

$$\tilde{\chi} = C_\chi \frac{\tilde{\epsilon}}{\tilde{k}}\widetilde{Z''^2}, \tag{3.11}$$

where C_χ is a constant set equal to 2 [65, 39].

3.1.4 Laminar flamelet model

The model assumes that chemical reactions take place in thin reactive-diffusive layers called the flamelets that are smaller than the smallest turbulent scales, while the rest of the field can be considered to be non-reacting. Since the flamelets are small, they are not

affected by turbulence and can be considered laminar, while diffusive transport occurs in the direction normal to the surface of the stoichiometric mixture [66]. This means that the scalar transport equations can be transformed to a system with the mixture fraction as an independent coordinate. In the steady laminar flamelet model, the flame structure is assumed to be in steady state and the time dependence can be neglected as

$$\rho \frac{\chi}{2} \frac{\partial^2 Y_k}{\partial Z^2} + \dot{\omega}_k = 0. \tag{3.12}$$

The solution for the flamelet equation can be computed prior to the CFD calculations and tabulated as function in the mixture fraction and parameterized scalar dissipation rate. The Favre-filtered quantities ($\tilde{\phi}$) such as the species mass fraction or temperature can be computed as

$$\tilde{\phi} = \int_0^\infty \int_0^1 \phi(Z, \chi_{st}) \tilde{P}(Z, \chi_{st}) dZ d\chi_{st}, \tag{3.13}$$

where $\tilde{P}$ is a presumed joint FDF and $\phi(Z, \chi_{st})$ is the pre-tabulated flamelet solution. Statistical independence is often assumed between the mixture fraction and scalar dissipation rate such that the $\tilde{P}$ is calculated as the product of two independent filtered density functions for mixture fraction and scalar dissipation rate. The mixture fraction FDF is usually presumed as β-distribution [67], calculated based on the filtered mean mixture fraction and its sgs variance. A Dirac-delta function is presumed for the scalar dissipation rate, assuming that it remains unchanged along the flame front [54].
In premixed flames, the same approach can be applied by relying on a different variable instead of the mixture fraction. A scalar that describes the degree of combustion completion, named progress variable, is defined such that it has a value of 0 for fresh reactants and 1 for burnt gases. The progress variable is constructed from the flame variables such as the normalized temperature or the mass fractions of the products [68].
The flamelet models provide better description of the chemistry than the EBU based models through the pre-tabulated functions with affordable computational cost. However, they are still limited by the assumption that the flamelets are smaller than the smallest turbulent scale.

3.1.5 Conditional moment closure model

The conditional moment closure (CMC) model takes advantage from the fact that most of the fluctuations of the reactive scalars can be correlated to the fluctuations of the mixture

fraction in non-premixed combustion. Thus, the difficulty in closure of reaction rates is avoided if the conditional averages of reactive scalars with respect to mixture fraction are considered [69, 70, 71]. In contrast to laminar flamelet models, CMC is not constrained by the laminar flamelet assumption, stating that the reactions take place in small scales not affected by turbulence [32]. In CMC, transport equations are solved to obtain the conditional moments. Such transport equations are usually solved over a grid coarser than the actual one, assuming that the spatial variation in conditional moments is limited in comparison to filtered values [72, 73]. The CMC equations can be derived from the corresponding transport equations for each reactive scalar through different methods such as the joint pdf method [70] and the decomposition method [69]. The conditional transport equation for species mass fraction is written as

$$\frac{\partial \langle Y_k|\eta\rangle}{\partial t} + \langle u_i|\eta\rangle \frac{\partial \langle Y_k|\eta\rangle}{\partial x_i} = \langle N|\eta\rangle \frac{\partial^2 \langle Y_k|\eta\rangle}{\partial \eta^2} + \langle \dot{\omega}_k|\eta\rangle, \tag{3.14}$$

where $\langle Y_k|\eta\rangle$ is the conditional mass fraction of species k, $\langle u_i|\eta\rangle$ is the conditional velocity, $\langle N|\eta\rangle$ is the conditional scalar dissipation rate and $\langle \dot{\omega}_k|\eta\rangle$ is the conditional reaction rate of species k. A similar transport equation is also solved for the conditional enthalpy. However, these equations involve additional terms that require further modeling.
After obtaining the conditional averages from their corresponding transport equations, the filtered quantities can be obtained by integrating the conditional averages with the FDF

$$\tilde{\phi} = \int_0^1 \langle \phi|\eta\rangle \tilde{P}(\eta) d\zeta. \tag{3.15}$$

The model can be extended to premixed combustion through conditioning with the progress variable instead of the mixture fraction [32]. The progress variable is defined as a normalized mass fraction of one of the reaction products such as carbon dioxide (CO_2) and water vapour (H_2O) or a weighted sum of more than one. The progress variable would then have a value of one in the fully burnt region and zero in the unburnt region.

3.1.6 Transported probability density function methods

The transported probability density function (PDF) methods are a class of modeling approaches that rely on solving a transport equation for a joint PDF of a set of variables that describe the state of a reacting medium rather than presuming it as in previous approaches. In principle, this approach is applicable to either premixed or non-premixed flames. The approach was first proposed by Dopazo and O'Brien [74, 75] and later developed to its

modern form by Pope [76].
In its baseline formulation, the PDF considered is a joint distribution of the velocity components, the composition variables and turbulent frequency. The local thermochemical properties are determined by the composition variables, which are typically taken as the species mass fractions and specific enthalpy for single-phase reacting mixtures. The joint PDF allows for complex interactions between turbulence and chemistry, as well as other physical aspects of flames such as soot and radiation to be well captured. Therefore, accurate modeling of scenarios where capturing these interactions are crucial can be achieved as in flames with strong local extinction and reignition [77].
The PDF transport equation requires closure for additional terms such as the transport of the probability density function in velocity space through the viscous stresses term. Modeling such additional terms is challenging, and the quality of the models providing the closure can affect the predictions depending on the combustion regime. In addition, the high dimensionality of the equation means that the standard numerical methods such as Finite-volume are not practical, and other approaches like the Monte-Carlo technique are adopted in nearly all simulations with the PDF methods [66].
The usage of PDF methods has been expanded from being only an academic research tool to becoming a modeling choice for laboratory scale flames. However, the application of PDF methods to engineering combustion scenarios is still limited due to the high computational cost associated with the solution of additional transport equations and incorporation of finite-rate chemical kinetics [77].

3.1.7 Multiple mapping conditioning

The multiple mapping conditioning (MMC) approach is a combination of the PDF and CMC methods with a generalized mapping closure that does not require an assumption about the type of the flow being modeled. The method is relatively new and was first proposed by Klimenko and Pope [78]. MMC makes use of the detailed treatment of the physical process provided by PDF methods but avoids the requirement for direct evaluation of the joint PDF which is dimensional in the composition space. Instead, CMC hypothesis can be used to restrict the dimensionality of the composition space to a certain manifold by making use of the assumption that the fluctuations in the reactive scalars are correlated to fluctuations in certain conserved scalar. Different formulations for MMC exist such as deterministic MMC and stochastic MMC as well as specific models with different reference variables [79, 80, 81]. A more detailed comprehensive review can be found in [82]. Although the reduction in dimensionality makes the MMC more computationally efficient than PDF methods, it is still computationally expensive for engineering

applications. In addition, model parameters choice requires more testing of the method in different combustion conditions.

3.2 Conditional source term estimation

The conditional source term estimation (CSE) method was first proposed by Bushe and Steiner [33]. CSE shares the same assumptions as the CMC method that the fluctuations in the reactive scalars can be linked to fluctuations in a conditioning variable. However, CSE does not require the solution of additional transport equations to obtain conditional averages and relies on integral inversion instead. Therefore, CSE avoids the need to model unclosed terms in those transport equations which can be problematic [35].
Although CSE was originally proposed for LES of non-premixed combustion, it has also been considered for RANS simulations [51, 83, 37, 84, 38, 85] and for premixed flames [86, 36, 50]. In addition, it has been extended to simulate lifted flames with double conditioning [39] and to simulate combustion with fuel spray [2, 87, 87] as well as sooty flames [88]. However, CSE was never considered previously for simulating buoyant diffusion flames as in fires which is the focus of the current study.

3.2.1 Formulation

CSE relies on the idea that the turbulent fluctuations of a filtered quantity such as species mass fractions and temperature are reduced when correlated to certain conditioning scalar depending on the combustion problem type. In non-premixed combustion, the mixture fraction is selected as the conditioning scalar in most cases. Consequently, scalars under consideration can be conditionally averaged on mixture fraction and, the resulting fluctuations in those conditional averages would be negligible compared to the fluctuations in the unconditional ones [35]. The filtered quantity can be related to the conditional average as

$$\tilde{f} = \int_0^1 \langle f|\eta\rangle \tilde{P}(\eta) d\zeta, \tag{3.16}$$

where $\langle f|\eta\rangle$ is the filtered scalar f conditioned at a specific mixture fraction value η in the mixture fraction space. The conditional averages are assumed to be constant spatially over an ensemble of cells and are considered space independent within each ensemble while varying with time only. To calculate the conditional averages, CSE uses an integral inversion approach.

A major advantage in dealing with conditional averages is that the negligible fluctuations allow for assuming first order closure for the chemical source term

$$\langle \dot{\omega}_k | \eta \rangle \approx \dot{\omega}(\langle Y_i | \eta \rangle, \langle T | \eta \rangle), \tag{3.17}$$

where $\langle Y_i | \eta \rangle$ is the conditional mass fraction of species i and $\langle T | \eta \rangle$ is the conditional temperature. For attached flames far from extinction and without ignition, this assumption is considered to be reasonable [89] and has been successfully applied previously [37, 65].
In the CSE approach, the species transport equations are first solved, and the Favre-filtered mass fractions are obtained. The conditional averaged mass fractions are then calculated through integral inversion of the relating equation

$$\tilde{Y}_k(x_j, t) = \int_0^1 \langle Y_k | \eta \rangle(\eta, x_j, t) \tilde{P}(\eta, x_j, t) d\eta. \tag{3.18}$$

The FDF $\tilde{P}$ is commonly presumed to be a β-distribution for non-premixed flames [67]. The β-distribution is constructed using the mean mixture fraction and its variance which are found using equations 3.7 and 3.10 as shown in Section 3.1.3 as

$$P(f) = \frac{\Gamma(\beta_1 + \beta_2)}{\Gamma(\beta_1)\Gamma(\beta_2)} f^{(\beta_1 - 1)}(1 - f)^{\beta_2 - 1}, \tag{3.19}$$

where Γ is the gamma function defined as

$$\Gamma(\beta) = \int_0^\infty x^{\beta - 1} e^{-x} dx, \tag{3.20}$$

β_1 and β_2 are the beta-function parameters and can be estimated as

$$\beta_1 = \mu \left(\frac{\mu(1 - \mu)}{\sigma^2} - 1 \right), \tag{3.21}$$

$$\beta_2 = (1 - \mu) \left(\frac{\mu(1 - \mu)}{\sigma^2} - 1 \right), \tag{3.22}$$

where μ is the mean mixture fraction value and σ^2 is its variance.
In theory, the conditional chemical source term is function in all of the considered species mass fractions in a given chemical kinetics mechanism. However, solving transport equations for all of the species then inverting them to find their conditional averages is a computationally expensive task since the number of species contributing in a given mechanism is usually big. For example, the GRI-MECH 3.0 [90] chemical kinetics mechanism for

methane-air combustion involves 53 species. Therefore, other techniques are used to reduce the number of required inversions such as pre-tabulation of the chemical mechanism as a function in small number of major species. Consequently, the chemical mechanism can be solved, and the rest of the species and reaction rates can be obtained as a function in those major species and the mixture fraction. The major species are chosen to be carbon dioxide (CO_2) and water (H_2O) because they have similar and relatively long formation time scales compared to other species [51]. This choice has been applied successfully previously for cases involving combustion of different fuels such as methane [37, 65, 39, 88], methanol [84], ethanol [87, 91] and acetone [2]. Thus, Eq. 3.18 is applied for the two species then inverted to get the conditional species mass fractions $\langle Y_{CO_2}|\eta\rangle$ and $\langle Y_{H_2O}|\eta\rangle$. Next, lookup tables are used to estimate the reaction rates as

$$\langle \dot{\omega}_k|\eta\rangle \approx \dot{\omega}(\langle Y_{CO_2}|\eta\rangle, \langle Y_{H_2O}|\eta\rangle). \tag{3.23}$$

The filtered reaction rate can then be obtained from the conditional reaction rate through integrating with the FDF as

$$\overline{\dot{\omega}_k}(x_j,t) = \overline{\rho}\int_0^1 \frac{\langle \dot{\omega}_k|\eta\rangle}{\langle \rho|\eta\rangle}\tilde{P}(\eta,x_j,t)d\eta. \tag{3.24}$$

The tabulation technique applied in the current study is the Trajectory Generated Low Dimensional Manifold (TGLDM) [92] which will be discussed in details in Section 3.3. The TGLDM technique has been successfully employed with most of the previous CSE studies [50, 37, 39, 88, 91]. Chemistry tabulation not only reduces the computational cost associated with inverting all of the mechanism species, but also avoids the problem of increased inaccuracies in mass conservation in mixture fraction space associated with inversion of large number of species which requires special treatment [93].

Although most of the previous CSE studies have relied on TGLDM for chemistry tabulation, CSE itself is not restricted to TGLDM. CSE has the ability to adopt any other tabulation technique such as the flamelet generated manifold (FGM) [94] which has been coupled successfully previously with both CMC for simulation of Sandia flames [95] and CSE in studying the transient effects of diesel spray [96]. In addition, CSE can rely on direct chemistry integration and avoid the need for tabulation [97].

In order to access the chemistry tables, the conditional mass fractions of major species are required, which are obtained from an integral inversion process that will be discussed in the next section.

3.2.2 Integral inversion and regularization

The variation of the conditional averages spatially is found to be much less compared to the spatial variation of the filtered quantities. This means that the conditional averages can be assumed to be homogeneous within an ensemble of points. Therefore, for each given ensemble, Eq. 3.18 that relates the Favre-filtered mass fraction to the conditionally averaged one can be rewritten as

$$\tilde{Y}_k(x_j,t) = \int_0^1 \langle Y_k|\eta\rangle(\eta,t)\tilde{P}(\eta,x_j,t)d\eta. \tag{3.25}$$

In this form, the conditionally averaged mass fractions are assumed not to vary in space within a given ensemble. The ensembles of points are constructed from the computational mesh. The ensemble distribution depends on the flame being studied. For example, it is usually assumed for axial jets that the conditional averages are radially consistent, and the ensembles are set as axial slices of the computational domain [98].
Eq. 3.25 is a Fredholm integral equation of the first kind with $\tilde{P}(\eta,t)$ as the kernel. It can be discretized using numerical quadrature into number of bins (M) in the conditioning variable space. Consequently, the equation can be written in the matrix form as

$$\vec{b} = \boldsymbol{A}.\vec{\alpha}, \tag{3.26}$$

where $\vec{b}$ representing the unconditional variable values is of size $N \times 1$, N is the number of grid points in a given ensemble, $\boldsymbol{A}$ is the matrix of integrated FDF over a mixture fraction interval, $\vec{\alpha}$ is the vector containing the conditional average values at each η_m with m as the mixture fraction bin index. The size of the matrix $\boldsymbol{A}$ is $N \times M$ and can be calculated as

$$A_{j,m} = \int_{\eta_1}^{\eta_2} \tilde{P}(\eta,x_j,t)d\eta, \tag{3.27}$$

where η_1 and η_2 define the mixture fraction bin lower and upper bounds. It is required to find the conditional averages $\vec{\alpha}$ knowing $\boldsymbol{A}$ and $\vec{b}$. However, direct numerical solution methods, such as the standard least-squares method, can not be used since Eq. 3.26 is an ill-posed system of equations. This means that the system of equations is sensitive to any small perturbations [99]. Therefore, a regularization method is required to obtain a unique solution that is smooth and stable. Various regularization techniques exist such as the Tikhonov regularization [100] and the truncated singular value decomposition [101]. In the current study, the Tikhonov regularization is adopted since it is characterized by a continuously-variable degree of regularization. The method can be implemented to

determine the conditional averages as

$$\vec{\alpha} = argmin \left\{ \left\| A\vec{\alpha} - \vec{b} \right\|_2^2 + \lambda^2 \left\| I(\vec{\alpha} - \vec{\alpha_0}) \right\|_2^2 \right\}, \tag{3.28}$$

where λ is the regularization parameter, $\vec{\alpha_0}$ is a priori knowledge of the solution which can be taken as the solution of an unstrained one-dimensional laminar flame [86] or the known solution from a previous time step [98], $\|..\|_2$ is the L-2 norm operator. In the current study, the solution from the previous time step is used as the priori solution. The regularization parameter is proposed following what is employed in previous CSE simulations [98, 65] to be

$$\lambda^2 = \frac{Tr(A^T A)}{Tr(I)}, \tag{3.29}$$

where Tr is the trace of the matrix and I is the identity matrix.

3.3 Chemistry Tabulation

The reaction rates are calculated based on the chemical reaction mechanism. Detailed chemical reaction mechanisms for a given fuel combustion are available such as the GRI-MECH 2.11 [102] and GRI-MECH 3.0 [103] for methane-air combustion. However, such mechanisms involve tens of species and hundreds of elementary reactions, and solving them for each computational cell at every time step requires prohibitive computational costs. In addition, the governing ordinary differential equations (ODE) are stiff since different time scales are included in the chemical reactions ranging from 10^{-10} second to more than 1 second. However, not all of such scales interact with turbulence, and the fast scales can be decoupled from the system [51]. Consequently, chemistry is tabulated in a way to include the detailed chemistry but still be represented by a low number of parameters. The method adopted in the current study is the Trajectory Generated Low Dimensional Manifold (TGLDM) [92, 104]. The TGLDM shares the same basic idea as the intrinsic low-dimensional manifold (ILDM) [105] method but does not suffer from the convergence difficulties and other problems associated with the ILDM [106]. In comparison to early efforts for chemical mechanism reduction such as the quasi-steady state and partial equilibrium assumptions, the only inputs required for TGLDM are the kinetic mechanism and the desired number of degrees of freedom of the reduced system [51].
In the TGLDM approach, the detailed chemistry is reduced to a low-dimensional manifold in the composition space. A manifold is generated corresponding to each mixture fraction

bin parameterized by the mass fractions of CO_2 and H_2O. The boundaries of the manifolds are determined based on the conservation of chemical elements for the given mixture fraction value. From the boundaries, initial points for the trajectories are specified. The trajectories evolve from the initial points until they reach the chemical equilibrium point. The evolution of the trajectories is based on the numerical integration of the governing ODE

$$\rho \frac{\partial Y_k}{\partial t} = \dot{\omega}_k \tag{3.30}$$

where $\dot{\omega}_k$ is the reaction rate of the species k determined by the chemical mechanism. A stiff ODE solver is used to get the trajectories evolution from Eq. 3.30 starting from the boundary points. The mass balance provides the initial conditions for the solution. The evolution of trajectories from different initial points ensures coverage of the realizable region defined by the boundary lines from pure mixing to the equilibrium point even that no strain rate term is included. An example of the generated trajectories for one of the manifolds is shown in Figure 3.1.

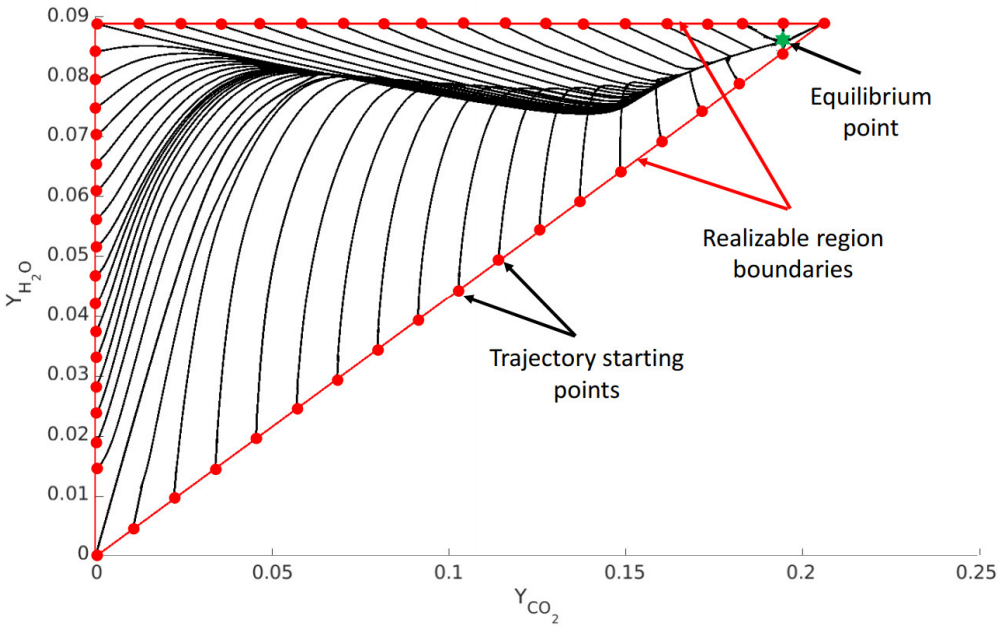


Figure 3.1: Boundaries and trajectories evolving from start points in a TGLDM manifold. Taken from [2].

The chemistry tables are represented in three dimensions, which are the mixture fraction, the mass fraction of CO_2 and the mass fraction of H_2O. These two species are selected

because they have similar and relatively long formation time scales compared to other species [51]. After the calculation of the trajectories, redundant points are removed from the tables to reduce their size. Then, delaunay triangulation technique [107] is employed to interpolate between the calculated points when looking up the tables to easily locate required points. The TGLDM with the triangulation applied is shown in Figure 3.2. The reaction rate of carbon dioxide for TGLDM manifold at the stoichiometric methane/air mixture fraction of 0.055 is shown in Figure 3.3.

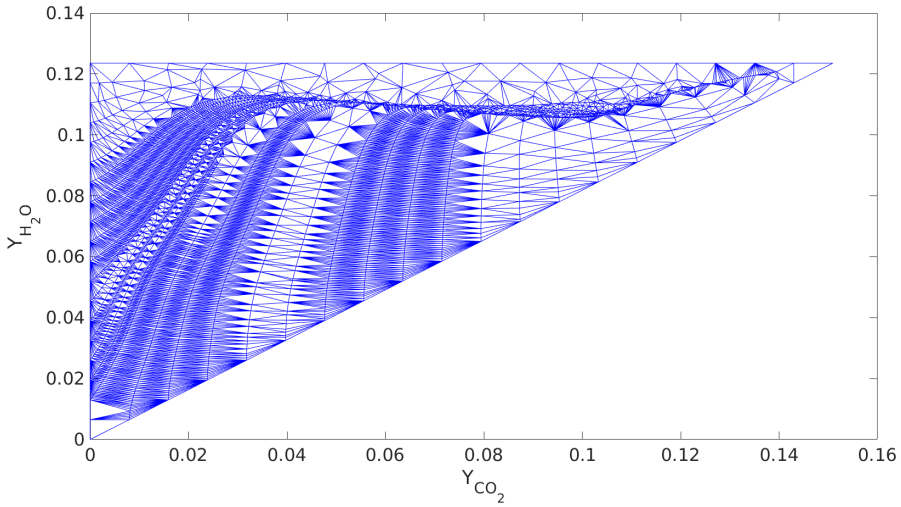


Figure 3.2: TGLDM with Delaunay triangulation at the stoichiometric methane/air mixture fraction of 0.055.

The tables include the species mass fractions and their corresponding reaction rates at each point. The conditional reaction rates can be extracted from the tables for a given conditional averages of CO_2 and H_2O mass fractions at a given mixture fraction bin. Filtered reaction rate may then be obtained from the conditional ones by integrating with the FDF following Eq. 3.24.

The standard chemistry tables in the current form are adiabatic ones that do not account for the effect of heat losses. Although the heat losses due to radiation are included in the enthalpy equation 2.7, the effect of the heat losses due to radiation or other sources on the chemical reactions can be included in the tables [88, 91]. In this case, an additional parameter is added to have different sets of tables with different enthalpy levels. More details are provided in Chapter 4.

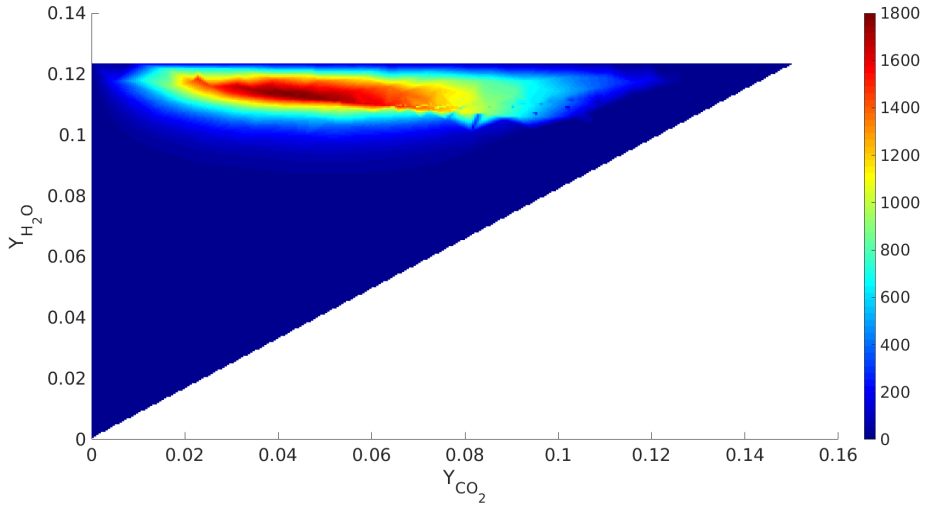


Figure 3.3: Reaction rate of CO_2 [1/s] plotted on a TGLDM manifold with Delaunay triangulation at the stoichiometric methane/air mixture fraction of 0.055

3.4 Radiative Heat Transfer

Unlike conduction and convection, thermal radiation is transferred through electromagnetic waves and, therefore, does not require a medium. Also, radiative heat flux tends to be proportional to the fourth power of temperature. That is why in combustion problems where temperatures exceed 1000 K, radiation cannot be neglected.

3.4.1 The radiative transfer equation

In order to determine the radiative flux at a point inside a participating medium, the radiative intensity at that point for all wavelengths and all directions should be known. This is governed by the radiative transfer equation (RTE) which is a radiative energy balance for a medium that emits, absorbs and scatters radiation along a line of sight in the direction s

$$\frac{dI_\lambda}{ds} = \kappa_\lambda I_{b\lambda} - \kappa_\lambda I_\lambda - \sigma_{s\lambda} I_\lambda + \frac{\sigma_{s\lambda}}{4\pi} \int_{4\pi} I_\lambda(\hat{s}_i)\Phi_\lambda(\hat{s}_i, \hat{s}) d\Omega_i, \tag{3.31}$$

where I_λ is the spectral radiative intensity of a wave with wavelength λ. The first two terms on the right hand side are the emission and absorption terms respectively. The

last two terms represent scattering which is usually negligible in flames. The coefficients of absorption and emission are the same (κ_λ) assuming the gas is diffuse and following Kirchhoff's law for a medium in a local thermodynamic equilibrium. The solution of the RTE provides the radiative intensity field which is then used to calculate radiative heat flux

$$q_{rad} = \int_0^\infty q_\lambda \, d\lambda = \int_0^\infty \int_{4\pi} I_\lambda(\hat{s})\hat{s} \, d\Omega \, d\eta. \tag{3.32}$$

The source term in the Favre-filtered enthalpy equation is then obtained as the divergence of the radiative heat flux [3]

$$-\dot{Q}_{rad} = \nabla . q_{rad} = \int_0^\infty (4\pi\kappa_\lambda I_{b\lambda} - \int_{4\pi} \kappa_\lambda I_\lambda \, d\Omega) \, d\lambda. \tag{3.33}$$

The blackbody radiation intensity is defined as

$$I_b = \int_0^\infty I_{b\lambda} \, d\lambda = \frac{\sigma}{\pi} T^4, \tag{3.34}$$

where $\sigma = 5.669 * 10^{-8} W/m^2 K^4$ is the Stefan–Boltzmann constant.

The RTE is an integro-differential equation with five independent variables (three space coordinates and two direction coordinates); thus, its solution is not straightforward. There are several methods developed to provide a solution for the RTE with various approximations. These methods include the spherical harmonics method or a variation of it, the discrete ordinates method (DOM) (or its more modern form, the finite volume method (FVM)), the zonal method, and the Monte Carlo method.
In the first approach, the directional dependence is expressed by a series representation (rather than discretized). However, such approach is not commonly employed due to the mathematical complexity involved. The exception is the lowest order implementation of the method (also known as the P_1) which is usually considered for its low computational cost. In the second technique, the intensity is assumed to be constant over discrete parts of the total solid angle of 4π. The zonal method (first developed by Hottel [108]) differs from the first two approaches in that it approximates the spatial, rather than the directional, behavior by dividing an enclosure into finite, isothermal subvolumes. The Monte Carlo technique is a statistical method that traces the history of bundles of photons through the enclosure.
There are also other approaches that combine features from the previous methods such as the discrete transfer technique [109] that combines features of the discrete ordinates, zonal, and Monte Carlo methods.

Currently, the most popular method implemented in CFD codes is the DOM/FVM method [110] as it relies on the same discretization techniques readily available for other transport equations. The finite-volume method is used to discretize the RTE spatially as well as in the angular direction. For a given direction (ordinate) $\hat{s}_i$ and for a cell of volume V, Eq. 3.31 is transformed to

$$\sum_k I_{ki}(s_i.\hat{n}_k)A_K = \beta_p(S_{pi} - I_{pi})V\Omega_i, \tag{3.35}$$

$$S_{pi} = (1-\omega_p)I_{bp} + \frac{\omega_p}{4\pi}\sum_{j=1}^{n} I_{bj}\overline{\Phi}_{ij}, \tag{3.36}$$

$$\overline{\Phi}_{ij} = \frac{1}{\Omega_i}\int_{\Omega_i}\int_{\Omega_j}\overline{\Phi}(\hat{s}', \hat{s})d\Omega' d\Omega, \tag{3.37}$$

$$s_i = \int_{\Omega_i}\hat{s}d\Omega, \tag{3.38}$$

where s_i is a vector emerging from the center of the solid angle Ω_i with a length that varies with the angle size, β is the extinction coefficient, ω is the scattering albedo, the subscript p refers to the value at the cell center, k refers to the value at the center of cell's face A_k and i is for the value associated with a solid angle Ω_i.
To relate intensities at face centers I_{ki} to those at cell centers I_{pi}, it is assumed that $I_{ki} = I_{pi}$ for intensities leaving the cell i.e. $s_i.\hat{n}_k > 0$. For intensities entering the cell, the value at the neighbouring cell center is used instead. Consequently, Eq. 3.35 can be rewritten as

$$I_{pi} = \frac{\beta_p S_{pi} V\Omega_i + \sum_{k,in} I_{ki}|si.\hat{n}_k|A_k}{\beta_p V\Omega_i + \sum_{k,out}(si.\hat{n}_k)A_k}. \tag{3.39}$$

where *in* means that the summation includes intensities entering the cell only ($s_i.\hat{n}_k < 0$) and *out* is for those leaving the cell only ($s_i.\hat{n}_k > 0$).

Since photons are emitted from gas molecules due to quantized changes in energy levels, this leads to the production of discrete spectral lines that are slightly broadened by number of effects such as molecular collisions and movements. This means that the spectral variation of the absorption coefficient is very huge. An illustration for this can be found in Figure 3.4 showing a part of the spectrum for carbon dioxide, composed of many spectral lines that are partially overlapping. Accounting for such variation requires the evaluation of the RTE at an extremely large number of wavenumbers which may reach a million. This is referred to as line-by-line calculations [111] which are, in consequence, computationally

highly expensive. Therefore, the use of this approach is limited to development of narrow-band correlations or validation of global models [112, 113].

To allow for more affordable calculations, band models were developed utilizing the fact

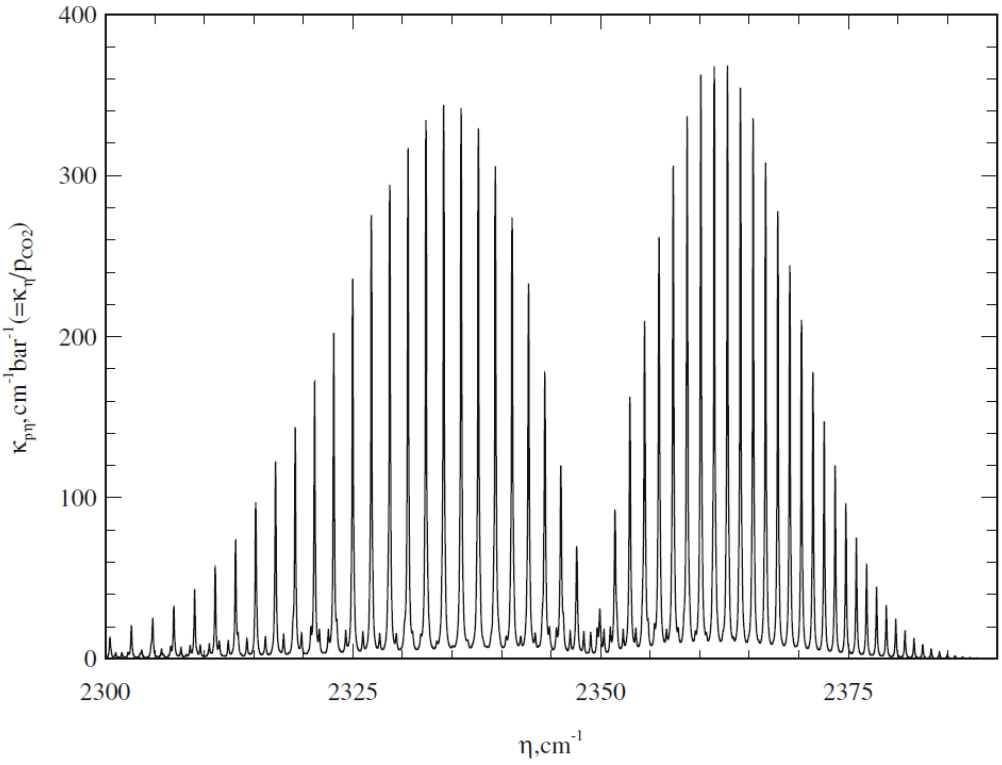


Figure 3.4: Pressure-based spectral absorption coefficient of CO_2 in nitrogen variation with wavenumber. Reproduced from [3]

that the blackbody intensity is nearly constant over a small spectral range, and that statistical models can be used to calculate the narrow band average emissivity [114]. Similarly, the narrow band k-distribution models benefit from the fact that within a narrow band, the repeated values of absorption coefficients will yield identical intensities I_η. Thus, the spectrally oscillating absorption coefficient can be reordered into a simpler monotonically increasing function varying with an artificial wavenumber [110]. However, a disadvantage of these methods is that they are difficult to apply in nonhomogeneous media.

In contrast, there are global models that integrate over the entire spectrum before solving the RTE. Thus, the number of RTE evaluations is hugely reduced. A popular example is the weighted sum of grey gasses (WSGG) model, first introduced by Hottel

[115]. The model has been extended from being used with the zonal method to becoming applicable with any arbitrary RTE solution methods [116], making it the most popular approach to deal with nongrey combustion media. In early approaches, WSGG model relied on experimental data but was later further developed to be used with high-resolution databases such as HITRAN [117] and HITEMP [118] referred to as spectral-line-based WSGG method. Similarly, the narrow band k-distribution concept has been extended to the entire spectrum to be referred to as the full-spectrum k-distribution method (FSK) [119].

3.4.2 Weighted sum of grey gases

Integrating the solution of the RTE for a spatially constant absorption coefficient in a non-scattering medium across the entire spectrum provides the expression of the total emissivity as

$$\epsilon(T,s) = \frac{1}{I_b(T)} \int_0^\infty (1 - e^{-\kappa_\lambda s}) I_{b\lambda}(T)\, d\lambda. \tag{3.40}$$

In the WSGG, the total emissivity is approximated as

$$\epsilon(T,s) = \sum_{n=0}^{N_g} a_n(T)(1 - e^{-\kappa_n s}). \tag{3.41}$$

where N_g is the number of proposed grey gases and κ_n is their absorption coefficients which are constants while the weighting function a_n is function in temperature

$$a_n = \sum_{k=0}^{K} b_{n,k} T^k. \tag{3.42}$$

The WSGG parameters for mixtures of carbon dioxide and water vapour were originally based on experimental data but are recently derived from correlations based on HITEMP as in [120, 121].

In the grey WSGG, a grey absorption coefficient is determined as

$$\kappa = -\frac{\ln(1-\epsilon)}{L}, \tag{3.43}$$

where L is the path length and can be defined as

$$L = 3.6\frac{V}{A}, \tag{3.44}$$

where V is the approximate flame volume and A is its surface area.

3.4.3 Optically thin approximation

The optically thin (OT) approximation assumes that the absorption term is negligible. This assumption has been employed successfully with CSE in jet flames [37, 2]. In addition, it has also been utilized in previous studies of pool fires [5, 20, 8, 122, 123, 124]. The radiative loss term in the enthalpy equation is expressed as

$$\dot{Q}_{rad} = 4\sigma(T^4 - T_b^4)\sum_i (p_i a_{pi}), \tag{3.45}$$

where T_b is the background temperature, a_{pi}, and p_i are the Planck mean absorption coefficient and the partial pressure of species i respectively. The background temperature term is included to prevent the temperature in the surroundings from dropping nonphysically, while still having a negligible effect on the flame region [125]. The Planck mean absorption coefficients for the main contributing species are calculated using RADCAL [126] with the curve fitting coefficients provided in [127].

Another implementation is to use a prescribed global radiant fraction, which is popular in fire simulations due to its simplicity. In this approach, the volumetric radiation source term that appears in the enthalpy equation is calculated as a fraction of the local heat release rate per unit volume

$$\dot{Q}_{rad} = \chi_{rad}\dot{Q}_{react}, \tag{3.46}$$

where χ_{rad} is the radiant fraction, which is set on a case by case basis and usually estimated experimentally. For medium scale pool fires, the radiant fraction value is approximately between 0.2 and 0.3 [40] depending on the fuel and the ambient conditions. It is measured to be 0.23 for methane [4], 0.24 for methanol [9], and 0.31 for acetone [9] fires.

3.5 Soot formation and modeling

Combustion of hydrocarbons under certain conditions may produce particulates called soot, which are masses composed mainly of carbon particles. Soot is produced due to incomplete

combustion of fuels in fuel rich regions at high temperatures. Studying soot is important because it is a major contributor affecting radiative emissions and concentration of toxic products in both engines combustors as well as fires [47]. Soot also is the main component in smoke generated from fires. It impairs visibility, complicating evacuation during fire-related incidents. Additionally, soot contributes to respiratory diseases and environmental pollution. In addition, smoke shielding blocks emitted radiation from escaping in large hydrocarbon fires, affecting the overall fire dynamics due to the interactions between chemistry, buoyancy generated flow and radiation.
A given fuel molecule may contain only few carbon atoms in gaseous phase, while soot particles are composed of carbonaceous agglomerate containing what may reach millions of carbon atoms in solid phase [128]. Consequently, the process of soot formation is complicated and is one of the challenging topics in combustion modeling due to the complex steps involved. In addition to the different chemical and physical natures of the fuel and the soot product, there is a high variability among the soot particles themselves with no unique chemical or physical structure. Soot starts as nearly spherical small primary particles smaller than 2 nm that combine to form aggregates of up to 300 nm [129].
The first step that leads to soot production is formation of radicals and intermediate hydrocarbon species from fuel pyrolysis under high temperature. Next, initial benzene rings are formed then combine together to produce polycyclic aromatic hydrocarbons (PAHs) which play a major role in soot formation. Nucleation of PAHs causes the formation of incipient soot particles. Finally, surface growth and coagulation of primary soot particles lead to formation of soot aggregates which are subject to oxidation.

- **Fuel pyrolysis and soot precursors**

Unsaturated hydrocarbons such as acetylene and its analogues as well as PAHs are thought to be the major contributors as soot precursors leading to soot nucleation [130]. After these species are formed from decomposition of fuel molecules, they react together or with other species, leading to chaining of the aromatic rings of PAHs and formation of higher order aromatics until reaching a point that allows transition to soot [53].

- **Soot nucleation (inception)**

After the formation of PAHs, these complex organic molecules begin to interact with each other as well as other species. PAH molecules collide and stick together, forming larger clusters. These clusters consist of multiple aromatic rings with stable structures. As the clusters grow, they reach a critical size, where they undergo a phase transition from the

gaseous state to a solid state. This phase change is crucial as it marks the nucleation of soot particles, transforming from individual PAH molecules into incipient soot particles. Next, the nascent soot particles provide the initial soot surface that evolve further through surface growth and coagulation, leading eventually to the mature soot particles [131].

- **Surface growth**

Condensed soot particles react with each other and with other gaseous species adding to the amount of soot. The growth of soot particles by reactions at the surface is thought to follow the same analogy as PAH growth through the H-abstraction carbon addition (HACA) mechanism. It is composed of an activation step followed by carbon addition through acetylene, as it is one of the most abundant species [132, 131]. The process is dependent on the available soot surface area and consequently the soot number density. Surface growth increases the total mass of soot but not the number of soot particles

- **Coagulation**

Soot particles can bounce into each other and combine to form bigger soot particles in a process called coagulation. This process allows for formation of larger soot particles. Particles may merge to form bigger spherical particles or stick to each other, forming clusters of particles of different shapes. Coagulation does not change the total mass of soot but affects the number of particles.

- **Oxidation**

The soot particles undergo oxidation (combustion) within the flame if the appropriate conditions are present. Soot oxidation requires the presence of oxidizing radicals and high temperatures. The counteracting effects between soot formation driven by nucleation, surface growth and coagulation against soot oxidation determine the leftover soot leaving the flame [133].

Numerous modeling attempts have been made in the past to accurately capture soot production and oxidation within CFD simulations of combustion scenarios [44, 45, 46]. However, no universal soot model exists as different models are varying in their applicability for an engineering scenario and accuracy. This issue is regarded to the complex physics of nucleation, inception, coagulation and agglomeration affecting soot formation chemistry [47].

Detailed soot models exist and rely on the description of reaction mechanisms of fuel pyrolysis and oxidation as well as polycyclic aromatic hydrocarbons (PAH) formation, mass growth and oxidation [134, 135]. However, their development and validation are restricted by limited simultaneous PAH and soot measurements [48]. Inclusion of detailed soot kinetics also remains computationally expensive for practical engineering fire CFD simulations. One alternative is to consider empirical soot modelling approaches that are much easier to implement in CFD. The major drawback is that they solely rely on experimental correlations for specific cases [136] and therefore, lack generality considering the wide range of fire conditions that may be encountered. As a trade-off between detailed kinetics and computational complexity/run time, semi-empirical soot models have been widely developed with varying levels of chemical description, using one or several additional transport equations of key soot quantities [137, 138]. They offer more affordable options, even if the model constants in the transport equations are often calibrated from experimental measurements [139, 140]. In fire analysis, two of the most common soot models are semi-empirical ones based on the smoke point concept. In this approach, the soot formation is assumed to be a function of the measured laminar smoke point (LSP) height for each fuel, which is an indicator of the sooting propensity for a given fuel [141]. The correlation between flame characteristics and the LSP height is first presented by Markstein et al. in [142] and is then related to soot formation by Delichatsios [143].

Previous studies have applied this concept to laminar flames for validation purposes [49, 144, 145, 15]. Beji et al. [49] have presented an approach based on the model from [143]. The model postulates that the soot formation in laminar diffusion flames is controlled by gaseous reaction processes. The model constants are calibrated with measurements from laminar candle type flames and extended to account for the variation of the sooting propensities in different fuels by determining a pre-exponential factor from the LSP height. The model is tested by Yao et al. [144] and coupled with soot oxidation model developed by [139] through simulating non-smoking and smoking ethylene flames as well as a propane flame. Good agreement is found between the predicted soot volume fractions and measured ones. The model is also capable of well reproducing the transition from non-smoking to smoking flames as the fuel flow rate increases. The study by Niu et al. [145] has extended the same model to simulate the sooting behaviour of multiple fuels mixing in the combustion region by introducing a new conserved scalar named the sooting tendency parameter and solving a transport equation for it similar to the mixture fraction transport equation but with boundary values at each fuel inlet equal to the ration of the mixture fraction boundary value and the corresponding LSP height. The model is validated in two different laminar flames, and it is found that soot is well predicted in them, indicating the ability of this approach in accounting for the sooting propensity of different fuels. Another approach is proposed by Lautenberger et al. [15] that models the

soot formation and oxidation, separately, as the product of presumed functions in mixture fraction and flow temperature. The functions are parameterized by the LSP height and fuel stoichiometry. The model is calibrated for laminar ethylene flames and then extended to laminar propylene and propane flames. The soot absorption cross-section peak values are relatively well predicted for the ethylene and propylene flames. For the propane flames, the predictions show that too much soot is predicted in the region near the inlet relative to what is measured experimentally.
Aside from laminar flames, limited studies have investigated LSP based soot models in simulating turbulent buoyant diffusion flames. In most cases, those studies have relied on EDM and EDC models for combustion modeling rather than more detailed approaches. Chen et al. [146] have extended the model by [49] to LES using the partially stirred reactor (PaSR) concept. The soot chemical time scale is assumed to be proportional to the fuel LSP height then the filtered soot formation rate is related to this time scale using the PaSR concept. Some modifications to this approach are proposed by Wang et al. [147] to overcome the limitations associated with the infinitely fast soot oxidation assumption and constant soot formation characteristic time. The modified model is tested in simulations of medium scale heptane and toluene pool fires, and it has been found that the modifications have limited effects on the results. Motaghian et al. [148] have used the local turbulent Reynolds number to calculate the mean chemical source term as a weighted average of the laminar and turbulent terms, and they have found that this approach is better in capturing soot concentrations near the burner in smaller pool fires where less turbulence is expected. Chatterjee et al. [21] have applied a flamelet-based subgrid soot-radiation model that is extended from the approach suggested in [15] to model a medium scale heptane pool fire [14]. The results indicate that there is good agreement in predictions of temperature and velocity and good qualitative reproduction of soot volume fraction data with some deviations. More recently, the model is extended to account for cases with varying oxygen concentration [149] and to model wall bounded buoyant turbulent diffusion flames anchored on a slot burner [150].

3.6 Summary

In this chapter, the different turbulent combustion models applied in CFD are reviewed with an emphasis on CSE approach. CSE shares the same assumptions as the CMC method but does not require the solution of additional transport equations and relies on integral inversion, thus avoiding the need to model unclosed terms in those transport equations

which can be problematic. The closure of the radiation term is also discussed with the solution methods of the RTE and the different approaches to estimate the absorption coefficient as well as the optically thin approximation. Finally, soot formation steps and soot modeling approaches in CFD are presented. The next chapter provides the modeling steps and results of turbulent line flame using CSE.

Chapter 4

LES-CSE of a methane line flame with optically thin radiation

The objective of this chapter is to assess the capabilities of a LES-CSE approach applied to a laboratory scaled turbulent buoyant flame without extinction. CSE is coupled with the LES solver, FireFOAM. Tabulated detailed chemistry is included. Radiation is treated using the optically thin model using four different implementations and the effect of sgs Turbulence-Radiation Interactions (TRI) is considered.
The availability of fire experimental data has been facilitated by the International Association for Fire Safety Science (IAFSS) working group, MaCFP (Measurements and Computations of Fire Phenomena) that shortlists a small number of target cases [151]. One of these cases is the University of Maryland (UMD) buoyancy-driven turbulent line flame burning methane [4, 152, 153].
As a first step, the baseline UMD case is considered for validation, in line with the strategy adopted in the first flamelet and CMC investigations [6, 8]. CSE combined with radiation modeling needs to be carefully examined in the context of LES and turbulent buoyant flame. This is the first time that LES-CSE is applied to a fire case and a suitable foundation must be established before more sophisticated models are applied. Further, detailed temperature measurements are available for the basline UMD case with 21% volume fraction in the coflow and they provide important intermediate information for model validation. The numerical predictions are compared with available experimental measurements for temperatures and their root mean square (rms) values. In addition, flame shape, unconditional and conditional species mass fractions, axial velocity and mixture fraction are also examined for qualitative analysis. Within the CSE framework, different radiation treatments are also considered to estimate the radiation and sgs TRI impact on the predictions. As

in the previous CMC study for the same flame [8], the RTE is not solved. Qualitative and quantitative comparisons will also be made with previously published results.

Previously published simulations can be found for the UMD flame conditions, varying in complexity for the description of the chemical kinetics, turbulence-chemistry interactions and radiative heat transfer. In the work of [5, 154], LES with the package FireFOAM in [5] and FDS in [154], including the EDC model is used including three step kinetics combined with an additional extinction model. The RTE is solved in finite volume, but radiation modeling is simplified by the assumption of a non scattering, non absorbing, optically thin grey medium and use of a prescribed global radiative loss fraction (PGRF) taken from the experiments. These initial studies are focused on assessing the implemented extinction and reignition models. In this context, global combustion efficiency trends are found to be well reproduced and limitations are also pointed out when mixing controlled turbulent combustion models like EDC are used to predict flame extinction. Maragkos and Merci [41] also consider FireFOAM with EDC and EDM, with one step chemistry. However, no prescribed radiative fraction is imposed. Instead, WSGG model [116] is selected for the absorption/emission. Reasonable temperature predictions and extinction trends are obtained, but results are shown to be sensitive to the critical temperature of the re-ignition model. In these three initial studies [5, 41, 154], the sgs turbulence-radiation interactions are neglected. Detailed chemical kinetics are included in the simulation of the UMD flame with the Steady Laminar Flamelet (SLF) model [6, 155], unsteady flamelet approach [7] and Flamelet Progress Variable (FPV) formulation [155]. In the the work of Xu et al. [7], non grey radiation effects with sgs TRI in the flamelet libraries and RTE solver are included. Temperature predictions were significantly improved with the unsteady flamelet model in comparison to those obtained by the SLF version due to the inclusion of unsteady effect and more accurate description of the radiation in the simulations. Ma et al. [155] solve the RTE equation including the Rank-Correlated Full-Spectrum k-distribution (RCFSK) method for the the determination of radiative properties coupled with two different flamelet models: SLF and FPV. For the UMD baseline case without extinction, both SLV and FPV are shown to provide similar predictions, but FPV performs better when extinction is present. Recently, Conditional Moment Closure (CMC) has been implemented for the baseline UMD flame, i.e. burning in a coflow of air without extinction [8]. In this first LES-CMC, one step chemistry and detailed kinetics are included and two radiation models, one based on a prescribed global radiative fraction and one using WSGG model without solving the RTE. The temperature predictions are shown to be sensitive to the selected chemical kinetics and CMC submodels, in particular to the conditional scalar dissipation rate (CSDR) model and coupling between CSDR and radiation model.
A summary of the different modeling approaches in previous studies is given in Table 4.1.

Table 4.1: Previous studies with modelling approaches

Study reference	Combustion	Chemical kinetics	Radiation
[5, 154]	EDC	3-step	PGRF
[41]	EDC/EDM	1-step	WSGG
[6]	SLF	GRI 3.0	WSGG
[7]	UnSt. LF	San Diego	WSGG
[155]	SLF/FPV	GRI 3.0	RCFSK
[8]	CMC	1/14-step	PGRF/WSGG OT

4.1 Computational details

4.1.1 Experimental setup

The University of Maryland (UMD) methane line burner is selected in the current study. The UMD line burner corresponds to a turbulent buoyant diffusion flame fuelled by methane [4, 152, 153]. The gas enters the domain through a rectangular slot with a length of 50 cm and width of 5 cm. The slot is surrounded by a horizontal plate followed by the coflow which is 75 cm in length by 50 cm in width. A schematic of burner top view is shown in Figure 4.1. The methane mass flow rate is 1 g/sec which corresponds to an average velocity of 1 cm/sec and a theoretical heat release rate of 50 kW. The coflow mass flow rate is 85 g/sec which corresponds to an average velocity of 25 cm/sec. The time-averaged and rms values of temperature are measured in the flame axially and laterally at several locations using 12.7-μm-diameter S-Type thermocouples. Soot production is negligible in this case [4] and is, therefore, not considered in the current work.

4.1.2 LES setup

The LES solver selected in the current study is a modified FireFOAM [25] solver, based on the open-source CFD package OpenFOAM. FireFOAM is a finite volume solver with implicit time integration that uses a variable density LES formulation and provide several options for treatment of turbulence, combustion and radiation.
In the present study, the sgs turbulence is treated using the Smagorinsky model [59] with the model constants set as $C_k = 0.02$ and $C_\epsilon = 1.048$. The computational domain is composed of a cuboid with 0.8 m length, 1.2 m width, and 2 m height in the x, y and z directions respectively, as shown in Figure 4.3. The cell size is 5 mm in the region $0.15 \times 0.6 \times 0.6$ m^3 in x, y, and directions resulting in 10 cells across the fuel port width.

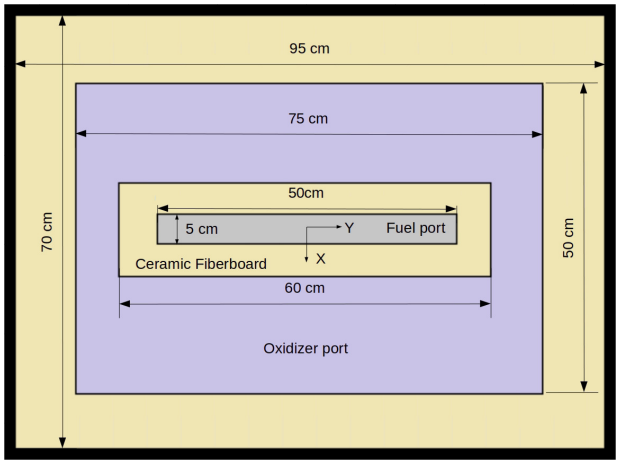


Figure 4.1: Schematic of the top view for UMD line burner [4].

The domain is high enough to cover the flame region which is measured to be 50 cm. The grid is stretched away in the rest of the domain and the total number of cells is 1,681,920. Finer grid resolution was tested and resulted in negligible changes in the results. The current grid resolution is also consistent with previously published LES for the same case where 5.5 mm [8], and 5 mm [7] grid resolutions are used in the region close to the fuel inlet.
The simulations are performed for a burning time of over 30 seconds in all of the cases. The collection of data starts after 10 seconds to make sure that initialization phase is not affecting the results. This is considered to be sufficient since fluctuations related to initialization settles in the first few seconds, as shown in the time history of temperature on the centerline at z=0.25m in Fig. 4.2. The Courant number is set to 0.8 resulting in a time step of approximately 0.4 ms. Each simulation is performed on one node of a Linux cluster with 20 processors for 7,200 CPU-hours.

For the inlet surfaces, the mass flow rate is described to match what is reported in the experiment. The convective and diffusive mass and energy fluxes are accounted for at the inlets following what is described in previously published studies for the same case [5, 6, 7, 155]. The imposed mass flow rate for methane is 1 g/sec and for the coflow air inlet is 85 g/sec. At the sides and outlet boundaries, a zero gradient is imposed for all scalars. The pressure and velocity are determined from the total hydrostatic pressure if the flow leaves the domain. In case of a flow reversal, the pressure is reduced by the dynamic pressure. This regulates any possible instability associated with a possible rapid rise in velocity since the driving pressure gradient is also reduced [156].

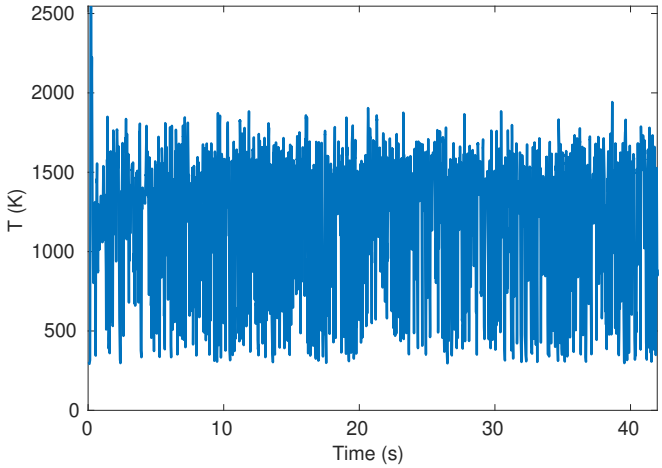


Figure 4.2: Temperature time history at z=0.25m.

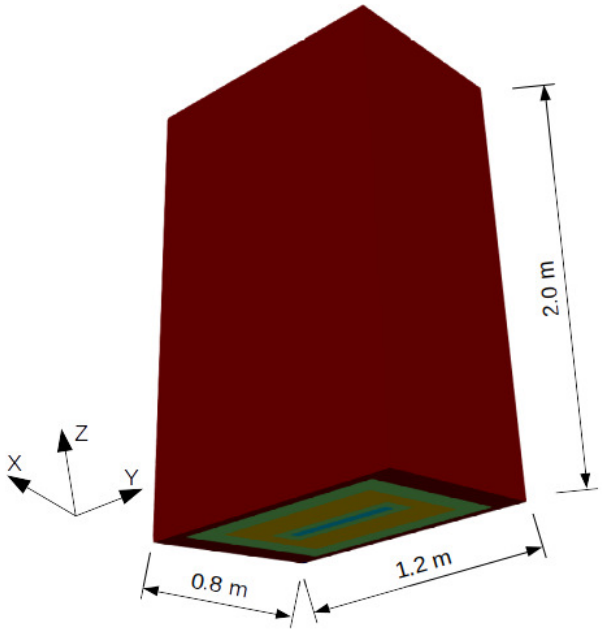


Figure 4.3: Computational domain outline showing fuel inlet in blue, walls in green, co-flow inlet in yellow, and entrainment in red.

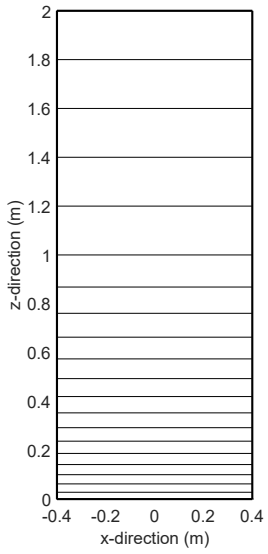


Figure 4.4: Distribution of CSE ensembles, shown on the centre plane of the LES domain

The LES solver uses implicit time integration with a second order accurate backward scheme and the time step is based on the maximum Courant number which is set to be 0.8. The convective terms in the governing equations are discretized spatially using a Total Variation Diminishing (TVD) scheme called limitedLinear while a second-order central difference scheme is used for diffusion terms.

4.1.3 CSE details

For CSE, the number of ensembles is equal to 20 dividing the domain as slices in the axial direction and clustered near the inlet to capture the spatial variations of the conditional quantities. The distribution of the ensembles is shown in Fig.5.3. The mixture fraction space is discretized in 50 bins clustered around the stoichiometric value (0.055). Two inversions are performed to determine $\langle Y_{CO_2}|\eta\rangle$ and $\langle Y_{H_2O}|\eta\rangle$ for each ensemble. For radiation modeling, in methods "CSE-Rad 3" and "CSE-Rad 4", an additional inversion is applied for $\langle T|\eta\rangle$. Conditional reactions rates of major species (methane (CH_4), O_2, CO_2 and H_2O) and mass fractions of minor species (carbon monoxide (CO), hydrogen (H_2 and hydroxide (OH)) are retrieved from the TGLDM tables. The unconditional values are calculated by integrating the conditional values with the FDF over η space.

4.2 Radiation modeling

Radiation is treated by assuming the medium to be non scattering and using the optically thin approximation that assumes the absorption to be negligible. This approximation is adopted in previous LES for the current case [8, 5] and medium scale pool fires [124, 20]. In the context of LES-CSE, four different implementations are considered focusing on the effects of TRI and radiation loss inclusion in the chemistry tables.
First, the radiative loss term in the enthalpy equation is expressed as

$$\overline{\dot{Q}}_{rad} = 4\sigma(\tilde{T}^4 - T_b^4)\sum_i(\tilde{a}_{pi}\tilde{p}_i), \tag{4.1}$$

where σ is the Stefan-Boltzmann constant, T_b is the background temperature, $\tilde{a}_{pi}$, and $\tilde{p}_i$ are the Planck mean absorption coefficient and the partial pressure of species i, respectively, calculated based on the Favre filtered flow variables. The Planck mean absorption coefficients for the main contributing species are calculated using RADCAL [126] with the curve fitting coefficients provided in [127]. In this initial approach, the effect of the sgs fluctuations on the radiative source term is entirely neglected, which is a crude approximation [157]. In the paper, this first method is denoted by "CSE-Rad 1".
In the second method, Eq. 4.1 is kept, but non-adiabatic TGLDM tables are included (instead of adiabatic tables in the first method). Different sets of tables with different levels of enthalpy loss are generated starting from the adiabatic set of tables. In other words, the tabulated conditional reaction rates and species mass fractions are corrected to include the effect of heat loss in the flame.
During the computations, a transport equation for adiabatic enthalpy with no radiation term is first solved to get a conditional adiabatic enthalpy $\tilde{h}_{ad}$

$$\frac{\partial(\overline{\rho}\tilde{h}_{ad})}{\partial t} + \frac{\partial(\overline{\rho}\tilde{u}_i\tilde{h}_{ad})}{\partial x_i} = \frac{\partial}{\partial x_i}\left(\overline{\rho}\,(D + D_t)\,\frac{\partial\tilde{h}_{ad}}{\partial x_i}\right) + \overline{\dot{Q}}_{react}. \tag{4.2}$$

Next, the enthalpy loss is calcuated from the Favre filtered adiabatic and sensible enthalpies as

$$\widetilde{h_{loss}} = \widetilde{h_{ad}} - \widetilde{h}. \tag{4.3}$$

The conditional enthalpy loss $< h_{loss}|\eta >$ is then obtained from the filtered one through integral inversion and used as one of the parameters in accessing the chemistry tables.
The conditional averages are found by linear interpolation using $< \Delta h|\eta >$ and the tabulated levels of enthalpy loss. In the present TGLDM, three different enthalpy loss values are included starting from adiabatic conditions moving to an enthalpy loss of 20% at stoichiometric conditions. This is achieved by decreasing the inlet temperature by 25K for all

mixture fraction values at the beginning of the TGLDM trajectory calculations. The total enthalpy is kept constant for each enthalpy loss value and the temperature is calculated from the total enthalpy and mixture properties in conditional space. Three enthalpy loss levels are found to be sufficient in the current case. This second method is denoted by "CSE-Rad 2".
In the third method, the adiabatic chemistry tables are considered only, as in the first method, however, the radiation loss term is calculated in conditional space using the conditionally averaged temperature and species, instead of the Favre filtered quantities to account for the sgs TRI as

$$\langle \dot{Q}|\eta\rangle_{rad} = 4\sigma(\langle T|\eta\rangle^4 - T_b^4)\sum_i(\langle p_i|\eta\rangle\langle a_{pi}|\eta\rangle). \tag{4.4}$$

$\langle T|\eta\rangle$ is determined by inverting Eq. 3.25 for $\widetilde{T}$, as described in Section 3.2.2. The radiation term, $\langle \dot{Q}|\eta\rangle_{rad}$ is then integrated with the FDF to get the averaged source term to be used in the filtered enthalpy equation following

$$\overline{\dot{Q}}_{rad} = \overline{\rho}\int_0^1 \frac{1}{\langle\rho|\eta\rangle}\langle\dot{Q}|\eta\rangle(\eta,t)\tilde{P}(\eta,x_j,t)d\eta. \tag{4.5}$$

In this approach, the sgs fluctuations related to temperature, Planck absorption coefficient and the species partial pressure are taken into account in the determination of $\overline{\dot{Q}}_{rad}$. This third method is denoted by "CSE-Rad 3".
The fourth method combined the second and third methods by implementing the non-adiabatic chemistry tables while calculating the radiation loss term in conditional space. This is the most complete optically thin model in the present LES-CSE context. This fourth method is denoted by "CSE-Rad 4".

4.3 Results

4.3.1 Flame structure

Instantaneous snapshots of the simulated and experimental flame surface are presented in Figure 4.5. The simulated flame surface is defined as an iso-contour of the volumetric heat release rate (200 kW/m^3). The experimental flame surface is obtained from a photographic view of the visible light emission from the flame region assuming that luminosity provides a suitable tracer of the flame contour [5]. In both the simulated and experimental flame

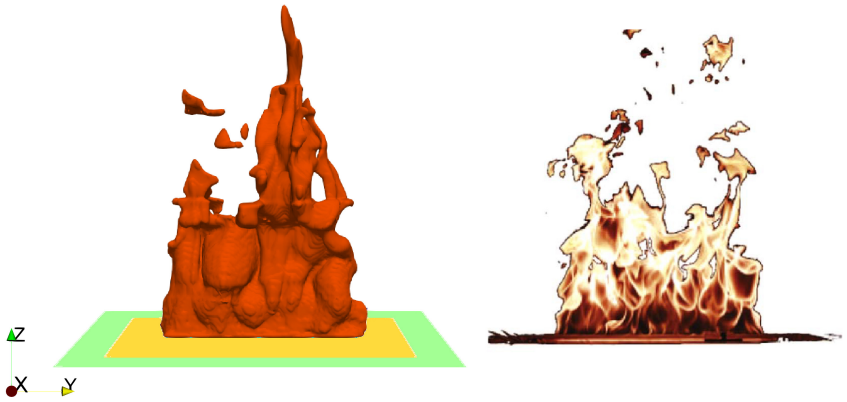


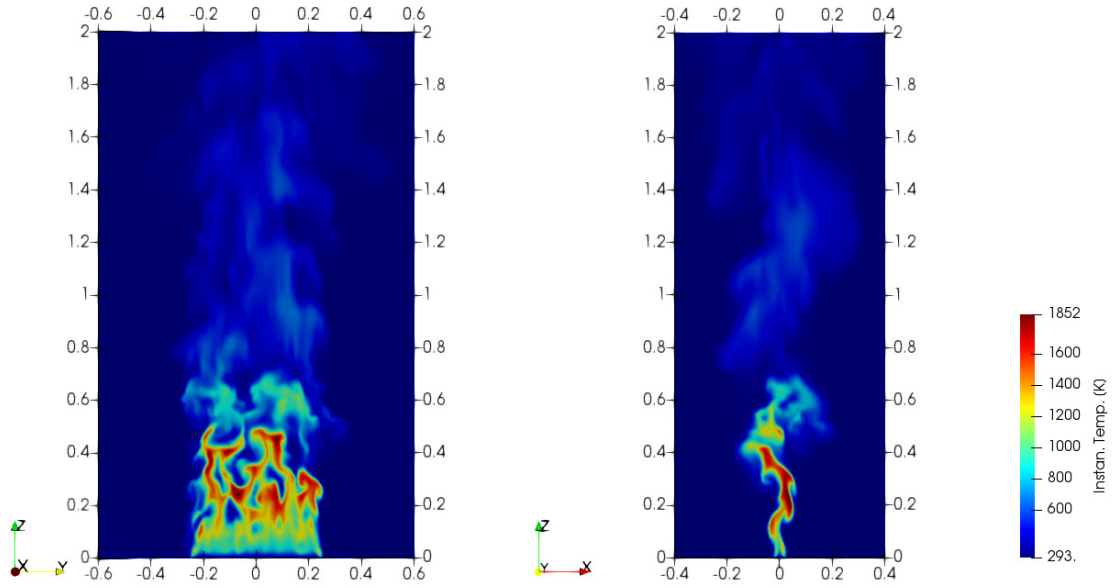
Figure 4.5: Comparison between the simulated flame surface defined as an iso-contour of the volumetric heat release rate of 200 kW/m^3 (left) and the experimental flame surface (right) reproduced from [5].

shapes, the flame near the inlet is continuous without any voids. Moving downstream, the intensity of turbulence increases due to the buoyancy driven motions. At the final region, the flame shows separated flame zones. The average height difference between the peak and the base of these zones is approximately 12.5 cm in both the experimental and simulated flames. At the tip of the fire, small independent flame structures that are completely detached from the main fire region are present.

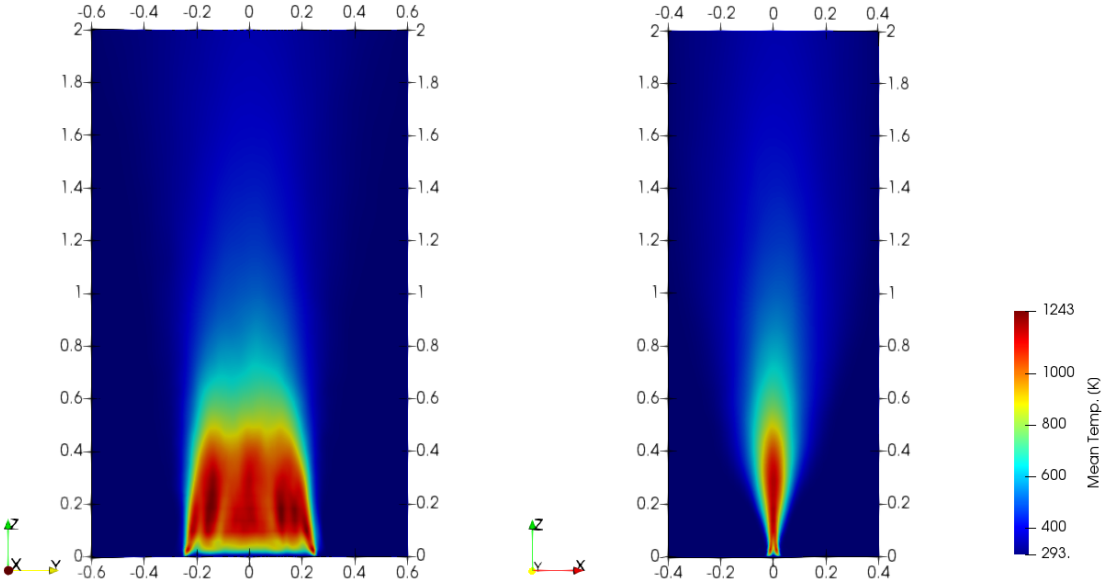
Figure 4.6 shows the instantaneous and mean temperature contours at the midsection of the domain from the front and side directions to present the overall shape of the flame. The predicted peak values in the instantaneous temperature are approximately 1890 K. The contours reveal that the flame region is confined within the first 50 cm, as measured experimentally [4]. The side view of the mean temperature contours shows that the flame width increases with elevation, which will be discussed in Section 5.2.2.

4.3.2 Time averaged temperatures

The centreline time averaged temperature profiles with corresponding rms are presented in Figure 4.7 for the four radiation model implementations, as shown in Section 4.2. In the four cases, the predicted temperatures increase from the fuel inlet value to a peak value. Then, farther downstream, the predicted temperature decreases, as expected. Experimental data show that the time averaged temperature increases rapidly from the inlet and reaches a peak of approximately 1180 K at 0.15 m above the fuel inlet. Then, the experi-



(a)



(b)

Figure 4.6: LES instantaneous temperatures (upper) and time-averaged temperatures (lower) front view at the central (y-z) plane along the burner (left) and side-view at the central (x-z) plane across the burner (right). All distances in m.

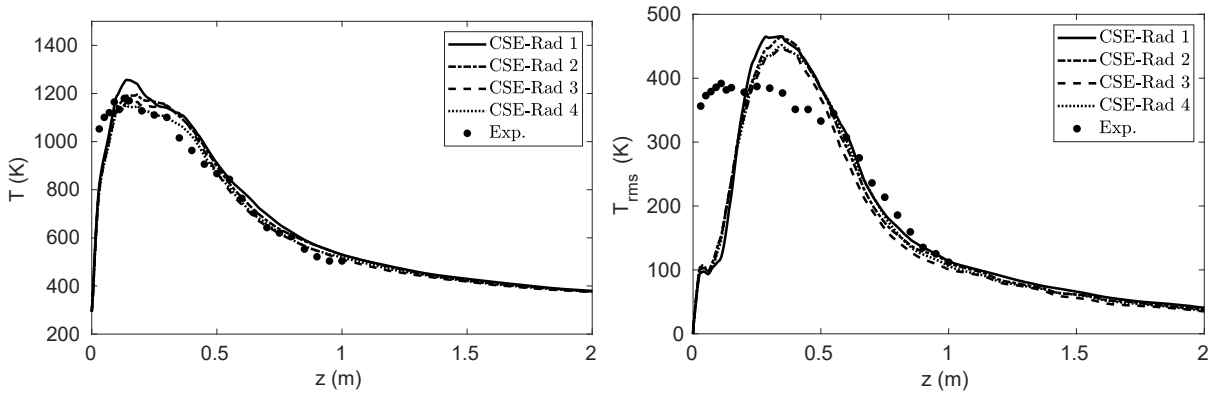


Figure 4.7: Centerline profiles: left time-averaged temperatures, right corresponding rms including experimental data (symbols) and current LES-CSE results obtained with four different radiation treatments, as described in Section 4.2.

mental centerline temperatures gradually decrease. In all of the four cases, the predicted time averaged temperatures increase to reach a peak value similar to the experimental value with a slight overprediction of approximately 6% in the first case with the adiabatic tables and 3% in the second case with the non-adiabatic ones. The other two cases, show very similar trends but with an underprediction of approximately 1% only in the maximum temperature value. However, the numerical temperature predictions show slower increase compared to the experimental data in the first 0.09 m. Farther downstream, the temperature profiles are well predicted and follow the experimental measurements.

The rms of the temperature T_{rms} profile is calculated by taking the square root of the time average of the squared difference between the recorded values and the calculated time average. Experimental T_{rms} values also increase rapidly to 400 K and then start dropping at z $\simeq$ 0.38 m. However, the predicted rise in T_{rms} is slower in the simulations and does not reach the peak value until 0.3 m from the fuel inlet. The peak value is overpredicted by approximately 17% in all of the four cases. Farther downstream in the plume region (z $>$ 0.5m), the predicted rms values decrease following the experimental measurements in the predictions of the four cases.

It is not clear why the LES-CSE temperatures and their rms are much lower than the experimental values in the first 0.09 m. Higher temperature and turbulence levels were tested at the inlet boundary conditions, but no improvement was noted: the initial temperature/rms increase was quickly damped out. In this flame, the experiments show a laminar region close to the inlet for z $<$ 0.05 m followed by a rapid transition to turbulence [5]. The current LES-CSE does not seem to capture the laminar and transition zones. Careful ex-

amination of the ensemble distribution, conditional average profiles and pdfs in this region (z < 0.9 m) do not reveal any anomaly. A grid refinement near the inlet was performed with a cell size of 2 mm instead of 5 mm, currently used, no significant improvement in the temperature could be seen, but an increase in the rms could be noticed, still well below the experimental values. Therefore, at this point, the discrepancies that can be seen in the predictions very close to the inlet are believed to be due to a grid resolution or sgs model or pdf shape. As will be seen in Section 4.3.6, temperature and rms underpredictions are also noted in some previously published studies.

Similar observations are found in the cross-stream temperature profiles at axial locations of 0.25 m, 0.5 m, 0.75 m, and 1.0 m from the fuel inlet, as shown in Figure 4.8. The time averaged temperature is well predicted and follows the experimental values. The variations in the predictions between the four cases are minimal and are present mainly near the centerline. The temperature rms is well predicted in general except near the centerline region at z = 0.25 m. This corresponds to what is observed in the axial distribution in Figure 4.7. At z = 0.5 m, the rms experimental values are overpredicted near the centerline by approximately 8% and closer agreement is achieved farther away from the centreline. At z = 0.75 m, the rms predictions are underpredicted near the centerline region. At z = 1.0 m, the rms predictions show only slight deviation from the experimental measurements. In addition, the flame width in all of the four cases is nearly the same and is slightly underpredicted at only z = 0.25 m, while it is more accurately predicted at the other locations. The flame height may also be determined using the time-averaged temperatures by examining the elevation where the mean flame temperature exceeds the surrounding air temperature by 550 K [124]. The calculated flame height is found to be 0.55 m for CSE Rad-1, 0.54 m for CSE Rad-1 and CSE-Rad-2, and 0.52 m for CSE-Rad-3 and 4. The experimental value is equal to 0.5 m determined by the 50% intermittency criterion for visible flame emission [152]. Therefore, the predicted flame height is in good agreement with the experimental value, keeping in mind that the comparison is not fully quantitative due to the different methods used to determine the height.

Overall, the results suggest that the current modeling approach captures well the flame structure and that the optically thin approximation is reasonable in the current study. The results are also in agreement with previously published data, as will be discussed in Section 4.3.6. The different radiation modeling approaches under consideration provide temperature predictions close to each other, with variations most evident at the region of the maximum temperature. However, the fourth case, CSE-Rad 4 that employs the non-adiabatic chemistry tables along with the calculation of the radiation term in the conditional domain provides the most accurate predictions among the investigated approaches. In the current CSE implementation, even when adiabatic TGLDM tables are used, radiative effects are still included in the enthalpy equation and therefore, have an impact on

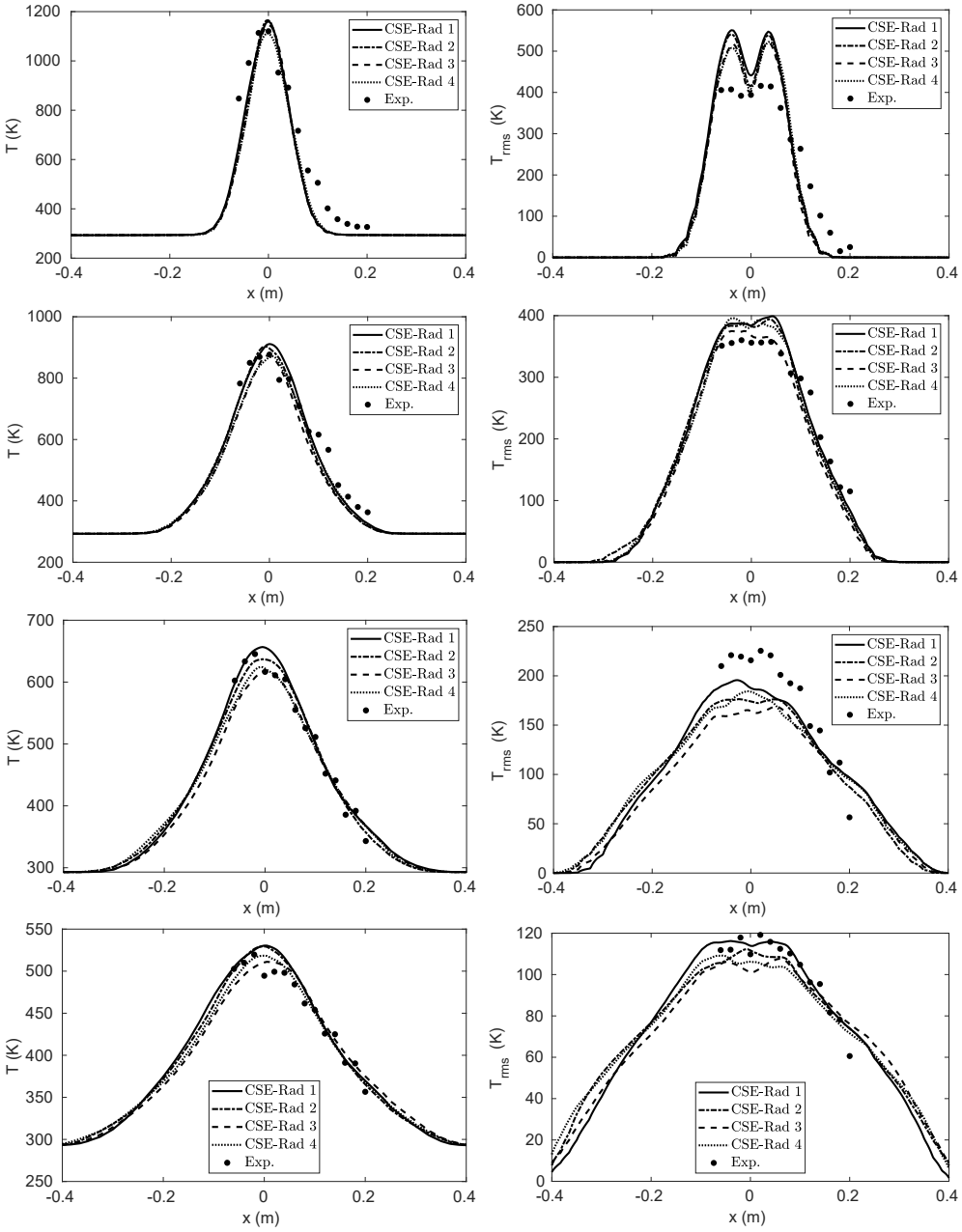


Figure 4.8: Cross-stream variation of the time averaged (left) and rms (right) temperature. From top to bottom, cross-stream profiles at heights 0.25 m, 0.5 m, 0.75 m, and 1 m.

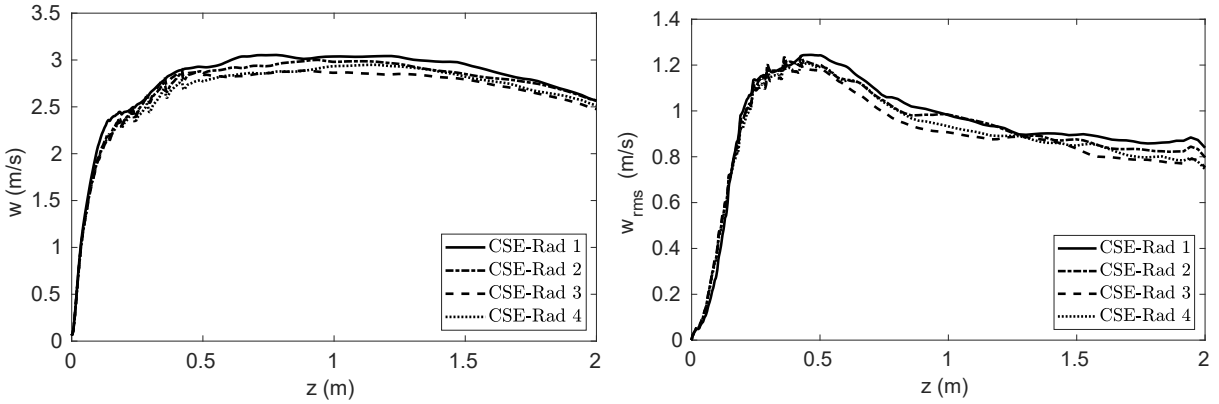


Figure 4.9: Vertical variation of axial velocity along centerline: left time averaged values, right rms values

the turbulent flow and mixing fields. Thus, some radiative effects are also included in the determination of the conditional mass fractions of CO_2 and H_2O through the inversion process in which the PDF is a major term, and then the other conditional quantities taken from TGLDM. In other words, the use of adiabatic TGLDM does not mean adiabatic conditions. In the non-adiabatic version of TGLDM tables, radiation is accounted entirely for in both physical and conditional spaces in a consistent manner. That is why the impact between the inclusion of adiabatic and non-adiabatic TGLDM may appear small in the current predictions. These findings are consistent with previous CSE predictions in a turbulent methane jet flame in atmospheric conditions with negligible soot formation [88]. Larger differences may be seen for other conditions like those close to extinction.

4.3.3 Axial velocity and mixture fraction

The vertical velocity along the centerline is presented in Figure 4.9. The time averaged vertical velocity increases from the fuel inlet value following the temperature rise. The axial velocity increases to approximately 2.8 m/s near z = 0.4 m for the four cases with slight variation between the four cases due to the variation in the temperature predictions in these cases and then stays approximately constant. The rms of the vertical velocity profiles show similar trends as the rms values increase from zero at the inlet to reach a value of 1.2 m/s at z = 0.4 m then start to decline with a lower rate.

The centerline mean mixture fraction is shown in Figure 4.10. However, there is no available experimental measurements for the mixture fraction for the current case. As

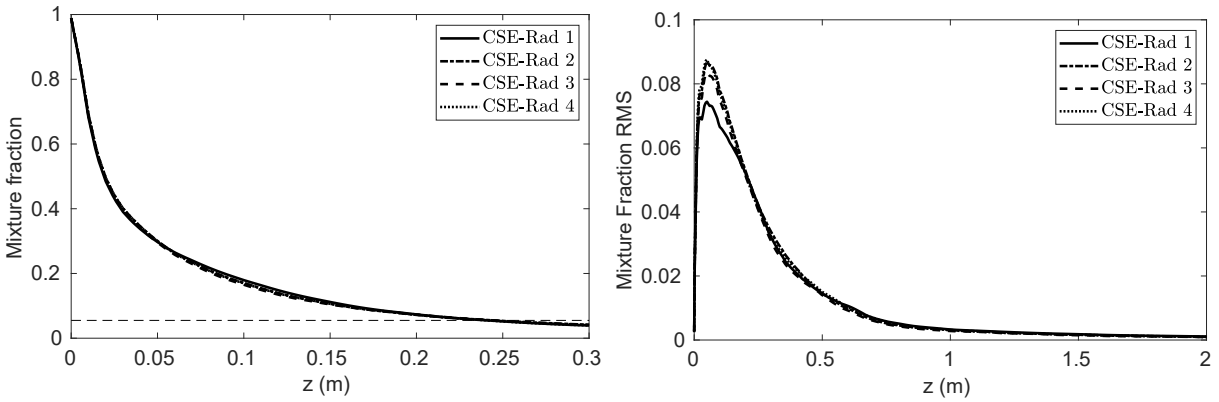


Figure 4.10: Vertical variation of mean mixture fraction along centerline: left time averaged values, right rms values

expected, the centerline values of the time averaged $\tilde{Z}$ follow closely what is observed in the axial velocity component. The time averaged $\tilde{Z}$ starts with value of 1 at the fuel inlet then rapidly declines along the centerline as mixing with the surroundings increases. The profiles reach the stoichiometric value of 0.055 for the methane-air mixture near z = 0.24 m. The rms of the mean mixture fraction fluctuations profiles show rapid increase up to z = 0.1 where the gradient of the time averaged values is maximum and then declines.

Although there are no available experimental measurements for velocity or mixture fraction for the case under investigation, the trends are in agreement with previously published results for the same case [5, 8].

4.3.4 Species mass fractions

The time averaged centerline mass fractions of CH_4, O_2, CO_2, H_2O, carbon monoxide (CO) and hydrogen (H_2) species are shown in Figure 4.11. Overall, the four cases present only slight variations in the species mass fraction predictions. The fuel mass fraction is rapidly decreasing from the inlet and is almost totally consumed 30 cm from the inlet. In contrast, O_2 is consumed in the flame region, as expected, and its mass fraction increases moving farther downstream approaching the ambient air value as more air is entrained into the fire plume. The mass fractions of CO_2 and H_2O increase in the flame region, as expected and then decay in the plume region as they mix with the coflow and entrained air. The CO profile shows rapid rise near the inlet where the mixture is rich, as expected. Farther downstream, CO is depleted as the mixture gets leaner and reaction with the excess O_2

takes place. The influence of such behaviour is evident also in the O_2 mass fraction profile as there is a step in the profile within the flame region and the slope is not smooth. In addition, the CO_2 profile's double peak can be explained by the same reason as near the inlet the mixture is rich, thus, the fuel is burned into CO_2 as well as CO. As the fuel is consumed, the CO_2 generation is hindered but then rises again as the CO oxidizes into CO_2 as the mixture gets leaner.

Although there is no experimental species mass fraction measurements for the given case, the general trends are in agreement with measurements and simulation results of a pool fire [158, 43].

4.3.5 Conditional averages

The conditional averages of the mass fractions of CO_2, H_2O, CO, and temperature are shown at different locations in Figure 4.12 for the base case. As can be seen, the conditional averages are close to each other at different locations. This confirms the lack of large spatial variation in the conditional average variation, as commonly seen in turbulent flames without extinction [32, 159]. The conditional averages of the mass fractions of CO_2, H_2O, and the temperature reach their peak near the stoichiometric mixture fraction and have lower values at the leaner and richer mixtures, as expected.

For the mass fraction of CO in Fig.4.12(c), the value is nearly zero for the lean mixtures where no production of CO occurs and the value starts to rise around a mixture fraction of 0.05 very close to the stoichiometric mixture fraction value as the mixture starts to shift from lean to rich.

4.3.6 Comparison with previously published numerical data

The centerline temperature profiles obtained from the fourth case, CSE-Rad 4, are shown in Figure 4.13 with the LES results published previously using EDC [5], SLF [6], unsteady flamelet [7] and CMC [8]. Different predictions were obtained in the CMC study, here, the best CMC predictions for the mean centerline time averaged temperature are included and correspond to the case with the Amplitude Mapping Closure (AMC) model for CSDR with prescribed radiative fraction as well as single step chemistry. Other cases with the WSGG radiation model show a high degree of underprediction in time averaged temperatures in comparison to the experimental measurements. As mentioned in the Introduction, these previous simulations also include different radiation models.
It can be seen that the current predictions are generally in good agreement with previously

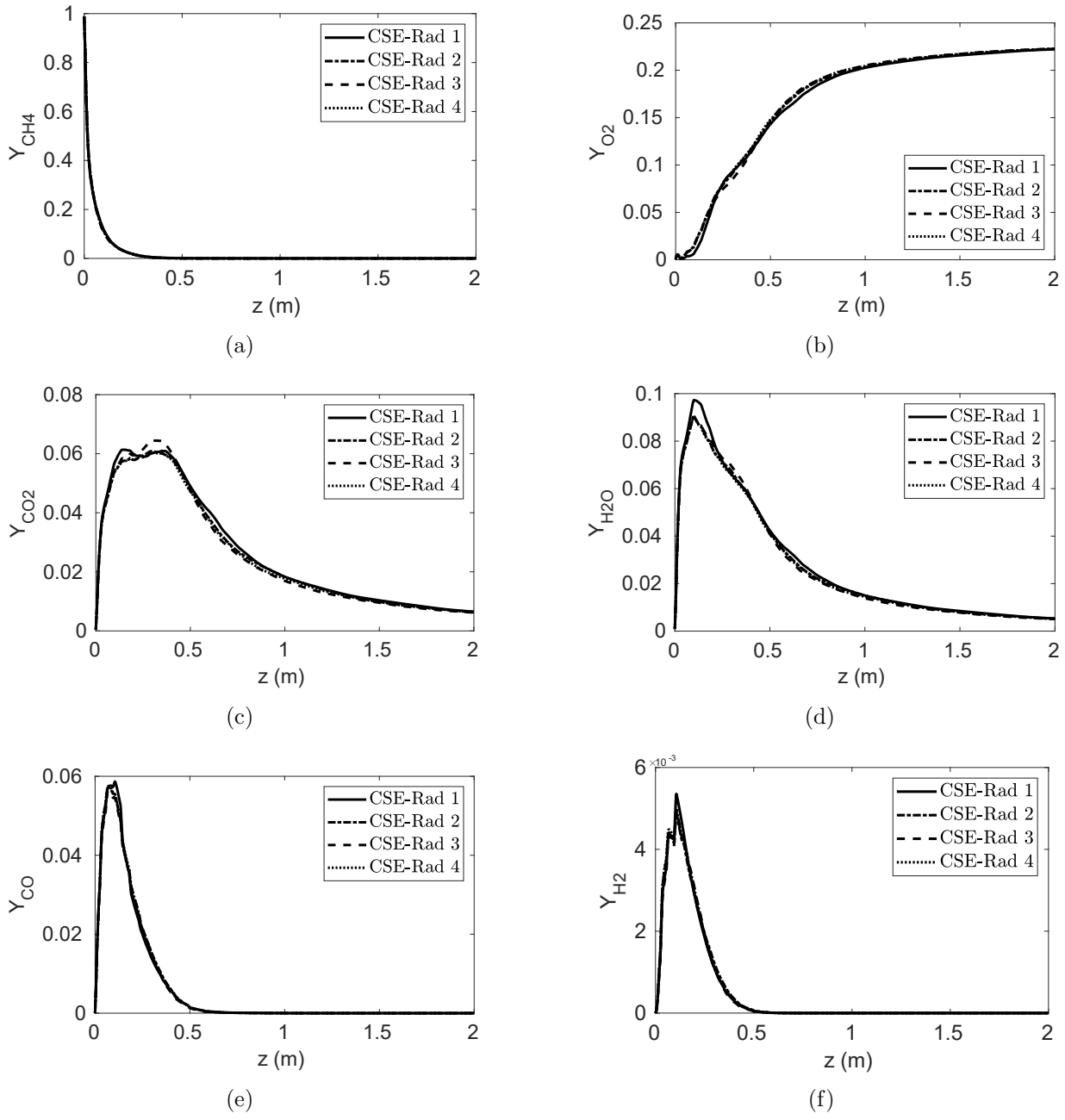


Figure 4.11: Centerline variation of the time averaged species mass fractions of (a) CH_4, (b) O_2, (c) CO_2, (d) H_2O, (e) CO ,and (f) H_2.

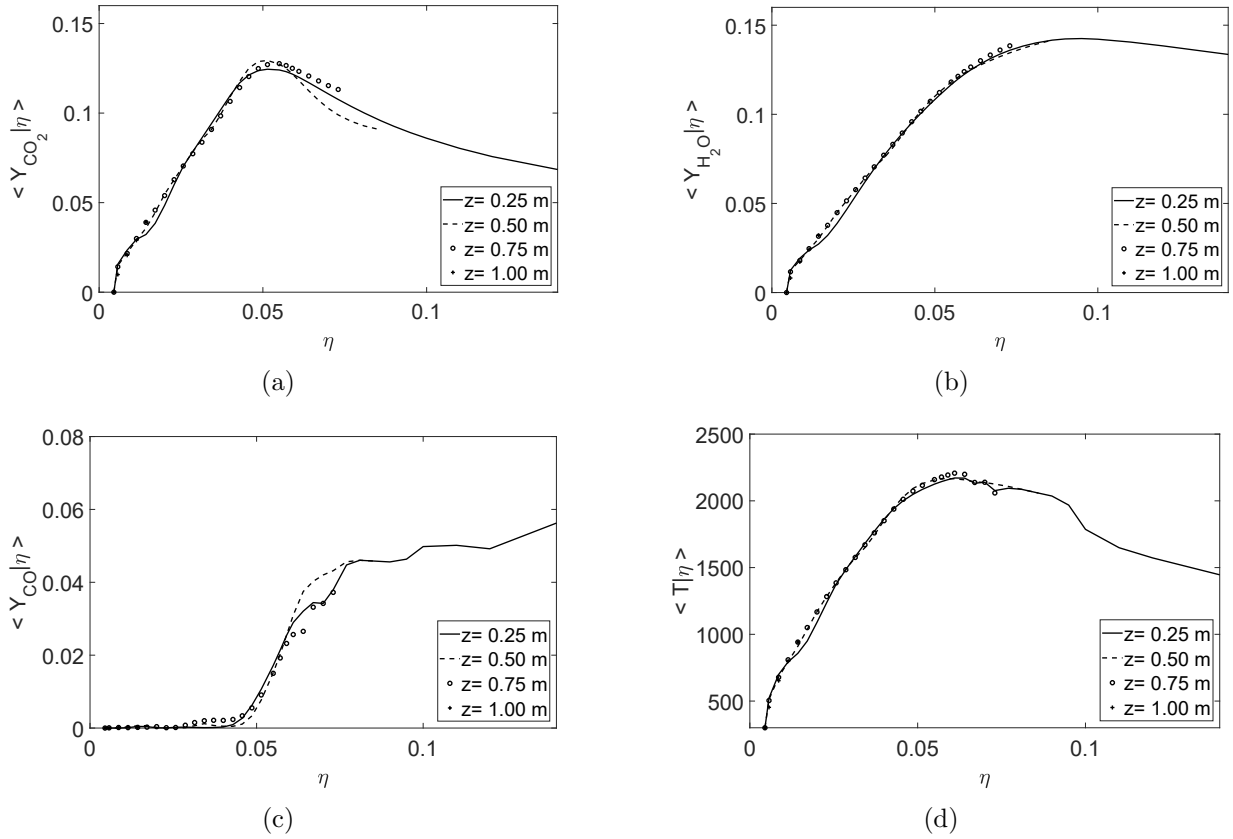


Figure 4.12: Conditional averages of mass fractions of CO_2, H_2O, and CO as well as temperature at 0.25, 0.5, 0.75, and 1.0 m from the inlet.

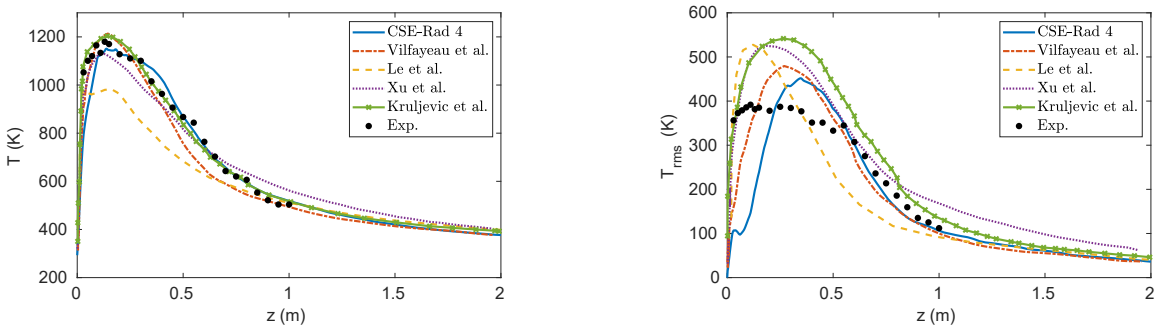


Figure 4.13: Comparison of centerline temperature profiles with previously published data employing EDC from Vilfayeau et al. [5], SLF from Le et al. [6], unsteady flamelet from Xu et al. [7], and CMC from Kruljevic et al. [8] combustion models.

published results except for the case with SLF which shows significant underprediction in the maximum time averaged temperature value. The predicted maximum temperature values using the EDC and CMC are nearly the same, while in comparison, that of the unsteady flamelet is lower by approximately 6.5%. The current predictions are situated between these two sets. In the downstream region after reaching the peak, the CMC profile follows the experimental measurements, while the EDC profile presents a more rapid decline with an underprediction in the time averaged values in comparison to the experimental measurements. The unsteady flamelet mean temperature predictions are closer to the experimental points for axial distances between 0.03 and 0.09 m, then farther downstream the unsteady flamelet and CSE predictions follow each other closely. The unsteady flamelet temperatures show a rapid decline with values lower than the measurements until z = 0.6 m and farther downstream, the opposite trend is displayed. The current LES-CSE results show closer agreement with the experiments in the plume region with only small overpredictions near z = 0.4 m. In addition, previous rms results with different models show overpredictions in the peak value at a higher level than that obtained in the current study with the CMC results showing the highest peak of about 40% overprediction compared to the experimental measurements. Near the inlet, the rms underpredictions are also visible in the results obtained by LES-EDC [5] and more recently in the work of Ma et al. [155] with the SLF and FPV models including a dynamic sgs model in LES. The current LES boundary conditions closely match those reported in previous studies for the same case [5, 6, 7, 8, 155]. At this stage, it is not clear what the sources of rms discrepancies between some simulation results and experiments are.

For additional comparison, the radiative fraction, χ_{rad}, is also calculated in the current

LES-CSE-Rad4 as

$$\chi_{rad} = \frac{\int \overline{\dot{Q}}_{rad} dV}{\int \overline{\dot{Q}}_{react} dV}, \tag{4.6}$$

where V is the computational domain volume. A value of 24.9% is found, which is in good agreement with the experimental estimate of 23% ±4.5% [7]. In previous work, 19% is reported in the unsteady flamelet simulations with the WSGG model and 35% with the grey assumption [7]. Previous EDC and CMC results include a prescribed value corresponding to the experimental value, in their simulations. However, the Heat Release Rate (HRR) is found to be 61.2 kW, larger than the experimental value of 50 kW. Similar discrepancies in the HRR are observed in the previous LES for the same case [7, 8]. The HRR is not an input for the current model formulation and does not have a direct impact on the predictions. Further detail on the issue of HRR prediction in fire simulation may be found in [160]. This HRR mismatch remains an outstanding problem in flamelet, CMC and CSE approaches and further research is needed to reconcile the experimental HRR and the values calculated by conditional or tabulated quantities.

Table 4.2: Duration, approximate time step and CPU time for current work and previously published studies, whenever available.

modeling approach	duration (s)	time step (ms)	CPU time (hours)
current work	30	0.4	7,200
LES-EDC [5]	20	0.5	2,700
LES-SLF [6]	30	0.5	25,000
LES-unsteady flamelet [7]	25	0.5	25,000

Computational costs may be compared with caution between the current LES-CSE and what is reported for the previously published simulations. Table 4.2 shows the duration, approximate time step and total CPU hours for the set of simulations run for the same flame, whenever available. The CPU time reported for the different flamelet model calculations (grey model for radiation) is larger than what is required for the present CSE calculations for similar durations. For fairness, it should be noted that the RTE is solved in these previous studies [5, 6, 7], expected to add significant computational time. No run time is reported in the LES-CMC study [8]. The CPU time also depends on processor architecture and code implementation.

4.4 Summary

The LES FireFOAM solver coupled with the CSE approach is applied to the UMD buoyant turbulent flame including tabulated detailed chemistry and different approaches for radiation modeling. The current time averaged temperature predictions are in good agreement with the experimental measurements, except very close to the fuel inlet. The predicted temperatures increase more slowly compared to the experimental data in the first 0.09 m above the burner exit. The temperature rms is in reasonable agreement with experimental data with the peak rms being overpredicted by approximately 17%. Further, flame shape, unconditional and conditional quantities, axial velocity and mixture fraction are also examined for qualitative analysis and found to correspond to expected trends.
The current LES-CSE predicted temperature and rms compare well with previously published numerical results for the same flame. The present LES-CSE formulation does not incorporate any conditional space submodels that were problematic in previous LES-CMC. The effect of the calculation of the radiation term in the conditional domain to account for TRI is found to have an influence on the predicted maximum temperature: the peak is reduced by approximately 7% moving the predictions closer to the experimental data. However, the use of the non-adiabatic tables is found to show only slight effect on the predictions for the current case. The predicted flame height closely matches the experimental value. The calculated radiative fraction is found to be in agreement with the reported value in the experiments. However, the HRR is found to be larger than the experimental value of 50 kW. In the current work, the radiation modeling formulation relies on the optically thin assumption along with the Planck mean absorption coefficients calculated using RADCAL. This is found to be reasonable for the selected case. This first LES-CSE provides a good foundation for further developments for more complex fire cases. The study can be extended to include more detailed models that account for absorption such as the finite volume discrete ordinate method combined with the weighted sum of grey gases. For this, the RTE will need to be solved, the conditional absorption coefficient may be calculated in conditional space as a function of conditional temperature and species concentrations like CO_2 and H_2O, the mean absorption may be determined by integrating the product of conditional absorption and FDF over mixture fraction space, similar to what is reported in [7] and the absorption TRI would be neglected, shown to be a reasonable assumption [161]. A more detailed radiation model is needed to extend the current LES-CSE framework to larger buoyant turbulent flames.

Chapter 5

Coupling between CSE and RTE solver for LES of methanol pool fires

Pool fires are well suited for the purpose of CFD model validation, displaying an ideal balance between realistic coupled thermo-chemical-fluids phenomena and simple geometry in controlled conditions. Generally, focusing on pool fires removes some complexities found in real fires related to flame spread and pyrolysis [162, 163]. As such, they are one of the most studied configurations [16]. They mimic real-world fire hazards that exist in the case of leakages from fuel tanks in industrial facilities, homes, or in transportation accident scenarios. Further, the fuel inlet can be defined as a flat horizontal surface of liquid or gas providing a simple study configuration.
Most pool fire simulations consider simplified sgs combustion models assuming infinitely fast chemistry such as EDC or EDM models [164, 16]. In these approaches, chemical reactions rates are limited by the turbulent mixing between fuel and oxidizer occurring at the sgs level and therefore, neglect the effects of finite-rate kinetics, crucial for accurate prediction of species concentrations and extinction/reignition. Similarly, radiation modeling is often simplified to the use of a constant radiative fraction. This approach may be effective when the radiative fraction is known prior to the simulations, but this poses issues when different fuels are present, leads to inaccuracies for the accurate estimation of heat feedback at the fuel surface and is questionable when several radiative flux components interact and large scale fires occur [165, 20]. Therefore, the use of a constant radiative fraction in the simulations sets a severe limitation to the desired predictive capabilities of CFD tools for fire safety. There are more sophisticated sgs combustion models capable of including detailed kinetics coupled with radiative effects using the transported probability density function [166, 167], flamelet model concept [168, 169], or CMC methods [32, 170].

The present investigation fits within this last class of approaches using CSE [171, 35] relying on the CMC concept with more accurate radiation models without prescription of any radiative fraction.
CMC and CSE have not been applied to methanol pool fires or any other pool fires with their developments and validation more focused on non-fire related turbulent combustion applications. These two approaches have the advantage of incorporating detailed kinetics without any specific assumption on the flame structure and in particular, no flamelet assumption is needed. This is achieved by including at least one additional conditioning space and using conditional averages. LES-CMC may be found for the well-ventilated case of UMD turbulent line flame with radiation modeled with a prescribed global radiative fraction and using WSGG [8]. Mixed success was observed due to high sensitivity of the predictions to the selected chemical kinetics and submodels, in particular the conditional scalar dissipation rate which had a notable impact on the results.
In Chapter 4, the first fire related application using CSE is illustrated. LES-CSE results are shown for the UMD case using detailed chemistry and with different radiation implementations, all assuming an optically thin medium and the radiative transfer equation was not solved. Numerical predictions for temperature and rms, and flame height were in good agreement with the experimental data.
The present chapter builds on these previous developments with some important changes to further expand the CSE framework. The RTE is solved, as available in the default version of FireFOAM, with the extension that all the radiation and chemical sources are evaluated in conditional space to account for TRI, adding significant steps in the calculations. Further, radiation absorption is included to advance from the optically thin assumption. The inclusion of radiation absorption effects in the solution of the RTE is important in real fire scenarios as the physical scale of the combustion zone implies that the optical thickness cannot be considered negligible. Further, WSGG model is implemented for the radiation calculations, first time in CSE, to bring the radiation modeling closer to previous studies of the same pool fire.
The objective of the present chapter is to assess the new developments of the CSE framework with improved radiation modeling in large eddy simulations applied to medium and large scale methanol pool fires. Results of radiation treatment in two ways are compared. The first is the optically thin approximation neglecting absorption. The second is through solution of the radiative transfer equation to account for absorption. The weighted sum of grey gases model is included in both cases and turbulence-radiation interactions are accounted for. The numerical predictions are compared with existing experimental measurements of time-averaged temperature and velocity as well as their rms values. The distribution of species mole fraction in the axial direction is also examined and compared with available experimental data. Within the current CSE framework, different radiation

treatments are considered that account for sgs TRI and account for absorption through the solution of the RTE.

5.1 Radiation modeling

Radiation is treated by assuming the medium to be non-scattering. Two methods are considered. The first relies on the optically thin approximation that assumes the absorption is negligible. In this method, the radiation loss term is calculated in conditional space using the conditionally averaged temperature and species mass fractions, instead of the Favre filtered quantities, as

$$\langle \dot{Q}|\eta\rangle_{rad} = -4\sigma\langle\kappa|\eta\rangle(\langle T|\eta\rangle^4 - T_b^4), \tag{5.1}$$

where σ is the Stefan-Boltzmann constant, $\langle T|\eta\rangle$ is the conditional temperature determined by inverting Eq. 3.25 for $\widetilde{T}$, as described in Section 3.2.2, $\langle\kappa|\eta\rangle$ is a wavelength-independent absorption coefficient calculated in conditional space, T_b is the background temperature [125].
The WSGG model [116] is used to estimate the absorption coefficient. In the WSGG, method, the total emissivity is approximated as

$$\langle\epsilon|\eta\rangle = \sum_{n=0}^{N_g}\langle a_n|\eta\rangle(1 - e^{-\kappa_n p_a L}), \tag{5.2}$$

where p_a is the partial pressure of the participating gases, N_g is the number of proposed gray gases, κ_n is their absorption coefficients which are constants while the weighting function a_n is a function of temperature,

$$\langle a_n|\eta\rangle = \sum_{k=0}^{K} b_{n,k}\langle T|\eta\rangle^k. \tag{5.3}$$

The WSGG parameters for mixtures of CO_2 and H_2O were originally based on experimental data but can also be derived from recent correlations based on HITEMP [121]. The latter derived values are selected in the current study. The present WSGG formulation does not account for fuel contribution. The absorption coefficient is then determined as

$$\langle\kappa|\eta\rangle = -\frac{\ln(1 - \langle\epsilon|\eta\rangle)}{L}, \tag{5.4}$$

where L is the mean path length and is defined as

$$L = 3.6\frac{V}{A}, \tag{5.5}$$

where V is the approximate flame volume and A is its surface area. The flame volume and area are calculated by assuming the flame to be cone-shaped with a diameter equal to that of the pool and a height equal to the one reported in the experiments.
The radiation term, $\langle \dot{Q}|\eta \rangle_{rad}$ is then integrated with the FDF to get the averaged source term to be used in Eq. 2.20 following

$$\overline{\dot{Q}}_{rad} = \overline{\rho} \int_0^1 \frac{1}{\langle \rho|\eta \rangle} \langle \dot{Q}|\eta \rangle(\eta, t)\tilde{P}(\eta, x_j, t)d\eta. \tag{5.6}$$

The advantage of integrating $\langle \dot{Q}|\eta \rangle_{rad}$ over the sample space is that the TRI effects are accounted for.

In the second approach, the absorption is accounted for by solving the RTE for an absorbing-emitting medium which is written as

$$\nabla \overline{I}.\vec{s} = \overline{\kappa I_b} - \overline{\kappa I}, \tag{5.7}$$

where I is the radiation intensity, $\overrightarrow{s}$ is its direction vector, κ is the absorption coefficient, and I_b is the blackbody radiation intensity defined as

$$I_b = \sigma T^4/\pi. \tag{5.8}$$

As presented below, Equation 5.8 is determined in conditional space using the conditional temperature. For the solution of the RTE, the WSGG model is also applied as in Eq. 5.4 to estimate wavelength-independent absorption coefficient at an affordable computational cost for LES. There are several methods developed to provide a solution for the RTE with various approximations [3]. In the current study, the finite-volume discrete ordinates method (FVDOM) is selected where the intensity is assumed to be constant over discrete parts of the total solid angle 4π as discussed in Section 3.4.1.
The source term in the Favre-filtered enthalpy equation (Eq. 2.20) is then obtained as the divergence of the radiative heat flux as

$$\overline{\dot{Q}}_{rad} = -\nabla.\overline{q}_{rad} = -4\pi\overline{\kappa I_b} + \int_{4\pi} \overline{\kappa I}\, d\Omega. \tag{5.9}$$

The TRI effects are accounted for by calculating the absorption coefficient and the emission term in conditional space first then integrating them with the FDF as

$$\overline{\kappa} = \overline{\rho} \int_0^1 \frac{1}{\langle \rho|\eta \rangle} \langle \kappa|\eta \rangle (\eta, t) \tilde{P}(\eta, x_j, t) d\eta \tag{5.10}$$

$$\overline{\kappa I_b} = \overline{\rho} \int_0^1 \frac{1}{\langle \rho|\eta \rangle} \langle \kappa I_b|\eta \rangle (\eta, t) \tilde{P}(\eta, x_j, t) d\eta. \tag{5.11}$$

The sgs fluctuations in the absorption term $\overline{\kappa I}$ are assumed negligible. Thus, the filtered absorption term may be closed as $\overline{\kappa I} \approx \overline{\kappa}\overline{I}$. This is known as the optically thin fluctuation approximation [172]. The effects of absorption TRI are shown to be negligible in LES [173]. The same approximation is also applied in previous numerical studies for the same methanol pool fire [43, 174, 42] as well as similar cases [7, 34, 6]. The inclusion of sgs fluctuations in the absorption term is not straightforward. In principle, the current CSE framework would be able to provide a complete closure of the absorption term: this would require inversion of the filtered radiative intensities and determination of the absorption term in conditional space and then use the FDF to recover the filtered intensities. However, this is extremely challenging to implement due to many additional inversions, equal to the number of solid angles considered, to be performed.
A flow chart summarizing the coupling between the CFD solver, CSE and the radiation calculations with the solution of the RTE is shown in Figure 5.1.

5.2 Medium-scale methanol pool fire

In the current section, the medium-scale methanol pool fire experimentally characterized by several groups [12, 10, 158, 9, 11, 175] is investigated due to the availability of experimental measurements of different flow quantities such as temperature, velocity, species and radiative fluxes. Methanol also offers the advantage of producing a non-sooting flame, which allows testing the main modeling elements of fluid mechanics, turbulence and radiation while avoiding the uncertainties usually related to soot modeling. This case is one of the target experiments in the MaCFP working group of the International Association of Fire Safety Science [176, 177], helpful for comparison with other numerical predictions using different modeling approaches.
Previous numerical results using EDM and EDC turbulent combustion models are available for this pool fire [122, 178, 179, 20, 180]. Early investigations by Chen et al. [122] including EDC for combustion modeling and relying on the optically thin approximation for treating radiation showed reasonable agreement with experimental data for velocity, but the temperature results were underpredicted in comparison to the experimental data.

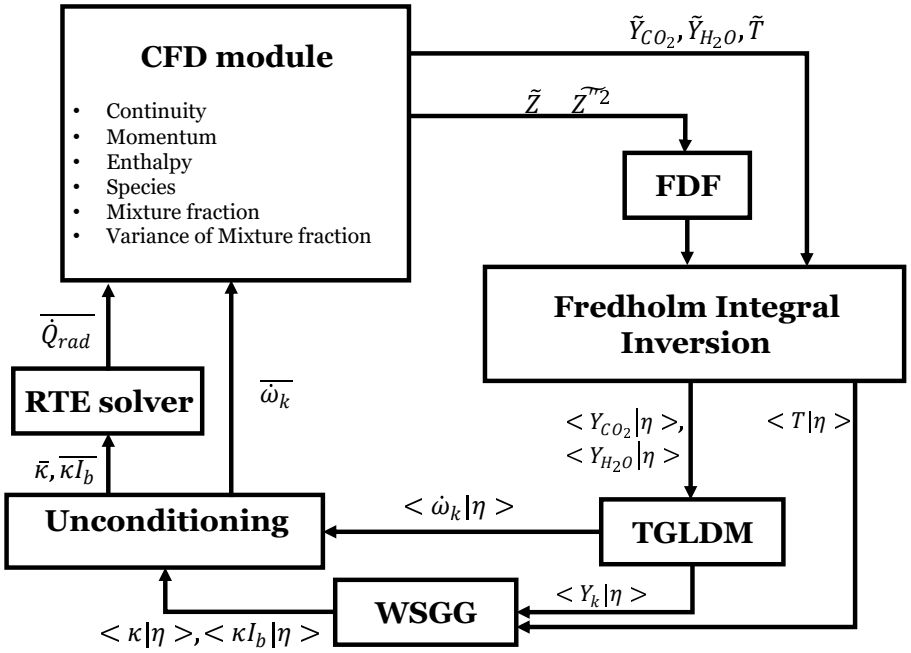


Figure 5.1: Flow chart showing the solution procedure for the coupling between the CFD (LES) solver, CSE and the radiation calculation with the solution of the RTE.

Maragkos et al. [178] applied the EDC model for combustion modeling with a one-step, infinitely fast, irreversible chemical reaction and compared different modeling approaches for turbulence and radiation. The use of the dynamic, instead of the standard, Smagorinsky model for modeling the sgs turbulence stresses and WSGG for modeling radiation instead of the optically thin global radiant fraction, in addition to considering a non-unity Lewis number and inclusion of differential diffusion effects provided better results for the centerline temperature predictions, but with increased computational cost. The study was extended to consider different mesh sizes and other fire cases as well [179]. The results showed that the dynamic procedure was more accurate and less grid dependent in comparison to the standard modeling approaches. Ahmed et al. [20] simulated the same case with combustion described using a global equation and EDM. Radiation was included with a prescribed radiation fraction and the WSGG approaches. Different mesh levels were compared for a domain that featured the fuel pan lip and pool elevation from the ground. The large scale processes occurring at length scales on the order of the pool diameter controlled the global pool fire features, while the dynamics near the pool surface were controlled by vortices and structures with smaller length scales. Different approaches were investigated for modeling the convective heat flux to the pool surface and the model based on stagnant film theory was found to be the best approach as it was only slightly grid sensitive [180].
More detailed chemical kinetics have been included in the simulation of the methanol pool fire with the laminar flamelet model [43, 174, 181, 182]. In the work by Ma et al. [43], the steady laminar flamelet model was implemented for turbulent combustion modeling along with the Rank-Correlated Full-Spectrum k-distribution (RCFSK) method for the determination of radiative properties. A comparison between different domain layouts showed the importance of reproducing the experimental configuration by including a fuel pan lip and an elevated pool surface from the ground to obtain accurate predictions. Consalvi et al. [174] focused on the effect of fuel radiation in both the medium and large scale methanol pool fires. They found that the inclusion of radiation effects due to methanol fuel vapor near the fuel surface improved the predictions of the heat feedback to the fuel surface with a small decrease in the mean temperature. Hubbard et al. [181] used a version of the narrow band RADCAL model to estimate the radiation absorption coefficients with a calibration applied to the radiation source terms by varying a reduction coefficient until a more accurate radiative fraction prediction was attained. The simulations included two cases, one with a standard prescribed fuel mass loss rate and the second using an algorithm to predict mass flux based on a mass and energy balance at the fuel surface. Both approaches showed similar predictions.
A summary of the different modeling approaches in previous studies is given in Table 5.1.

Table 5.1: Previous studies with modelling approaches

Study reference	Combustion	Chemical kinetics	Radiation
[122]	EDC	1-step	OT
[178, 179]	EDC	1-step	WSGG
[20]	EDM	1-step	PGRF/WSGG
[43]	SLF	Li et al.	RCFSK
[181]	SLF	San Diego	RADCAL

5.2.1 Computational details

Experimental setup

The medium-scale methanol pool fire reported in [10] is used in the simulations for the current study. This case is one of the target experiments in the Measurement and Computation of Fire Phenomena (MaCFP) working group of the International Association of Fire Safety Science [176, 177]. The fuel evaporates from a pool of 30.5 cm diameter. The methanol evaporation volume flow rate is reported to be 1.35 cm^3/s which corresponds to a theoretical heat release rate of 21.3 kW (corrected value from what is originally reported [183]). The time-averaged and rms values of temperature and velocity are measured in the flame at several locations. The species mole fraction centerline measurements are provided for the same case [11] as well as radiative heat flux at different locations [9]. Soot production is negligible and is, therefore, not modeled in the current study.

LES setup

The LES calculations are performed with a modified FireFOAM [25] solver, based on the general purpose open-source CFD package OpenFOAM. FireFOAM is a finite volume solver with a variable density LES formulation following what is performed in Chapter 4. This LES platform is selected due to extensive validation for buoyant turbulent flows with and without combustion and was shown to reproduce the turbulent plume features and associated phenomena of entrainment and puffing [184, 185, 163, 186, 179].
The computational domain is cylindrical in shape with 1.5 m diameter, and 1.75 m height in the z direction, as shown in Figure 5.2. The fuel inlet is placed such that it is raised 0.3 m (one diameter) above the ground and the burner features a lip height of 1 cm to replicate the experimental setup [10]. A previous study showed that it was important to reproduce the rim height maintained in the experiments for accurate results [43].

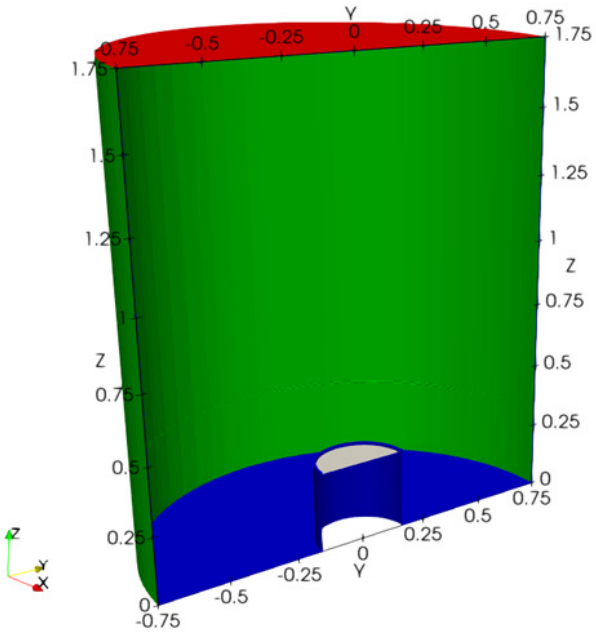


Figure 5.2: Computational domain sectional view showing the fuel pan with the burner lip at the center, and the overall domain dimensions in meters. The fuel inlet is in grey, domain outlet in red, entrainment boundary in green, the burner walls and the ground are in blue.

The grid cell size is equal to 5 mm in the pool region up to a height of 43 cm from the surface of the pool. Then the grid is stretched away in the rest of the domain. This means that the inlet is lower than the rim by 2 cell thicknesses in the current model. Previously, 1 and 2 cell thicknesses have been reported for modelling the lip wall height [178, 179, 180] and a finer resolution of 2.5 mm was used in the work of Ma et al. [43]. The 5 mm mesh resolution follows the MaCFP recommendation [177] for this case and is consistent with previously published LES for the same case but using different sgs combustion modeling approaches [180, 179, 42, 178, 43]. In addition, this resolution guarantees the satisfaction of the criterion that the ratio of the characteristic fire size (D^*) [187], to the grid size is in the order of 10–15 or higher [176]. TThis ratio with the selected LES mesh is approximately 40. Further, the current mesh resolves over 90% of the turbulent kinetic energy. The total number of cells is 677,336. Finer grid resolution with 2.5 mm cell size near fuel inlet and at the middle of the pool was tested and resulted in negligible changes in the predictions. The simulations are performed for a burning time of at least 35 seconds in all the cases. To make sure that the initialization phase is not altering the results, the collection of data does not start until after 10 seconds. The time step for the simulations is approximately 0.5 ms controlled by the Courant number which is set to 0.8. This value was also selected in previous LES-CSE of another buoyant flame [52]. The current Courant number also falls within values used in previous studies, 0.9 [178, 179, 180], 0.75 [20] and 0.6 [43] for the same case currently investigated. In the present study, the constant Smagorinsky model [59] is used for treating the sgs turbulence with the model constants set as $C_k = 0.02$ and $C_\epsilon = 1.048$. Implicit time integration with a second order accurate backward scheme is taken for the LES solver. In the governing equations, a Total Variation Diminishing (TVD) scheme called limitedLinear is applied for the spatial discretization of the convective terms while a second-order central difference scheme is used for the diffusion terms.

For the inlet surface, the mass flow rate is described to match what is reported in the experiment. The imposed mass flow rate for methanol is equal to 1.067 g/s. The inlet boundary condition for the scalars accounts for both advection and diffusion fluxes. Zero gradient is imposed for all scalars at the sides and outlet boundaries. If the flow leaves the domain, the total hydrostatic pressure is used to determine the pressure and velocity. In case of a flow reversal, the pressure is reduced by the dynamic pressure. This regulates any possible instability associated with a possible rapid rise in velocity since the driving pressure gradient is also reduced [25].

For the solution of the RTE, two angular meshes of 32 and 128 angles are considered. The finer mesh exceeds the recommendation by the MaCFP working group of 100 angles resolution for this case [177]. In addition, previously published simulations used 48 angles [179], 64 angles [20], 72 angles [178] and 128 angles [181].

The three cases that are considered with the optically thin approximation and with solving

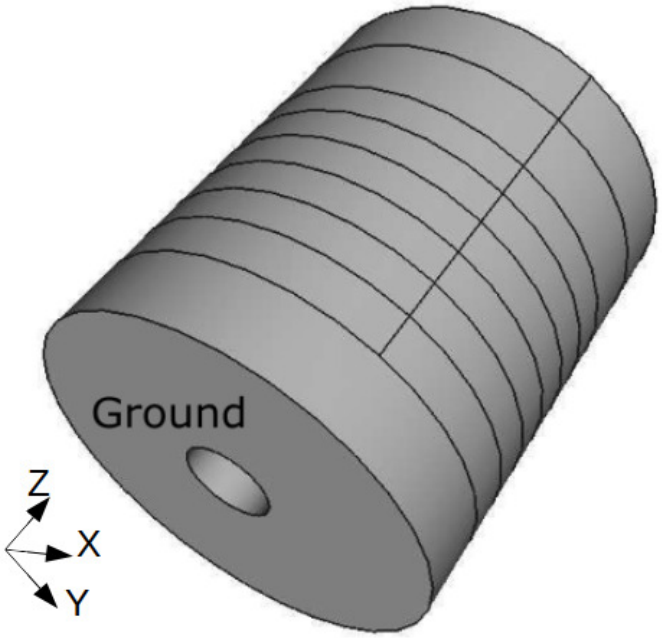


Figure 5.3: Distribution of CSE ensembles over the computational domain

the RTE with the two angular meshes will be referred to as Case-OT, Case-RTE32 and Case-RTE128, respectively.

CSE details

The LES domain is divided into CSE ensembles defined as slices in the axial direction and split into two halves. The ensembles covering the first 90 cm from the pool surface each have a height of 15 cm, equivalent to half of the pool diameter, and the height of ensembles in the rest of the domain is 27.5 cm. The ensembles do not cover the region lower than the pool surface on the sides of the burner as no reactions are expected in those regions given that the fuel evaporates from the pool surface and gets burned downstream. The distribution of the ensembles is illustrated in Figure 5.3. This ensemble distribution follows what was previously employed for LES with CSE [65, 39]. The mixture fraction space is discretized in 70 bins clustered around the stoichiometric value (0.135). To determine $\langle Y_{CO_2}|\eta\rangle$ and $\langle Y_{H2_O}|\eta\rangle$, two inversions are performed for each ensemble in addition to an extra inversion applied for $\langle T|\eta\rangle$ needed for radiation modeling. Conditional reactions rates of major species (methanol (CH_3OH), O_2, CO_2 and H_2O) are retrieved from the TGLDM

tables as well as mass fractions of minor species (CO, H_2 and OH). Eq. 3.25 is applied to calculate the unconditional values by integrating the conditional values with the FDF over η space.

5.2.2 Results

Flame structure

In Figure 5.4, instantaneous snapshots of the experimental and simulated flame surfaces of Case-OT are presented. The experimental flame snapshots are obtained from a photographic view of the visible light emission at two time instances during the flame cyclic pulsing [9]. The simulated flame surface is defined by the iso-contour of the volumetric heat release rate (200 kW/m^3). Both the experimental and simulated flames experience the puffing behavior common in pool fires. They both appear attached near the fuel surface with the combustion zones initially confined to near the fuel surface. In the second view, both the experimental and simulated flames appear to have a smaller base near the pool surface that forms an elongated tube-like shape with larger flame puffing structures in the downstream due to the buoyancy driven motions. Also, smaller structures appear to be branching from the main combustion zone away from the pool surface as well.
The flame height is estimated to be 40 cm in Case-OT and 42 cm in Case-RTE32 and Case-RTE128. The estimation is based on the axial point at which the time-averaged temperature exceeds that of the ambient by 550 K beyond the maximum temperature point [124]. These predictions fall within the reported value of 36.4 ± 16 cm in the experiments, for which, the measured value is based on processing video recorded frames of the experiments [11]. In addition, the radiative fraction is estimated by evaluating $\chi_{rad} = \int \overline{\dot{Q}}_{rad} dV / \int \overline{\dot{Q}}_{react} dV$. In the three cases, the radiative fraction is approximately 0.21 which is in agreement with the experimentally measured value of $0.24 \pm 25\%$ [9] including the experimental uncertainty.
The pulsation frequency is obtained from the simulations using the Fourier transform of the time history of vertical velocity at 0.35 m above the pool surface on the centerline. The estimated value is 2.08 Hz for Case-OT, 1.97 Hz with Case-RTE32 and 1.93 Hz with Case-RTE128. These frequencies are lower than those found in the experiments by examining the video record of the fires, determined to be 2.8 ± 0.3 Hz in [12] and 2.65 ± 0.08 Hz in [188].
A possible explanation for the discrepancy in the puffing frequency prediction is related to the way the fuel pool surface is modelled in the simulations. The current fuel inlet is modelled as flat horizontal surface where gaseous fuel at boiling temperature enters the

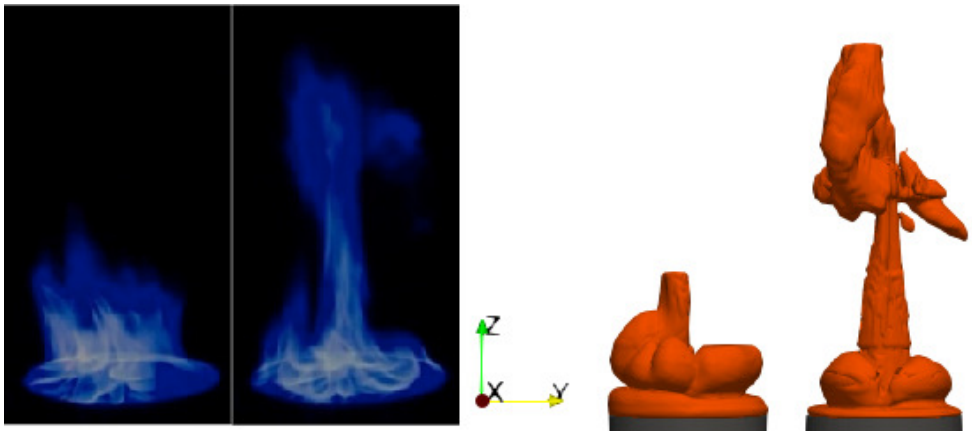


Figure 5.4: Comparison between the experimental flame surface (left) reproduced from [9] and the simulated flame surface defined as an iso-contour of the volumetric heat release rate of 200 kW/m^3 (right). For both the experimental and numerical snapshots high and low flames at different time instants are shown.

domain. In the experiments, it is reported that the liquid pool surface exhibits standing waves of 2.0 Hz frequency [12]. Thus, the fuel evaporation rate would be neither steady nor uniform. It is expected that such variation at the fuel inlet would alter the predicted overall fire puffing frequency.

Temperature and velocity

In the LES-CSE, mean quantities are obtained as both time and azimuthal averaging. Figure 5.5 shows the centerline variation of the temperature and axial velocity with height above the pool surface. Both the time-averaged and the root mean square (rms) variations are presented. Simulation results are shown for the case with the optically thin assumption as well as with solving the RTE using 32 and 128 angular resolutions. In all the figures, z_p is the axial height measured from the pool surface (30 cm from the ground). In general, the time-averaged results are in good agreement with the measurements [10] with slight underprediction in the time-averaged maximum temperature value for the optically thin case and that using 32 angles. The maximum time-averaged temperature reported experimentally is 1324 K and is measured at 8 cm from the pool surface at the center of the pool. The predicted maximum time-averaged temperature is nearly the same in Case-OT and Case-RTE32 and is lower than the measured value by approximately 8%. These predictions are reasonable considering the estimated experimental uncertainty of about 5%.

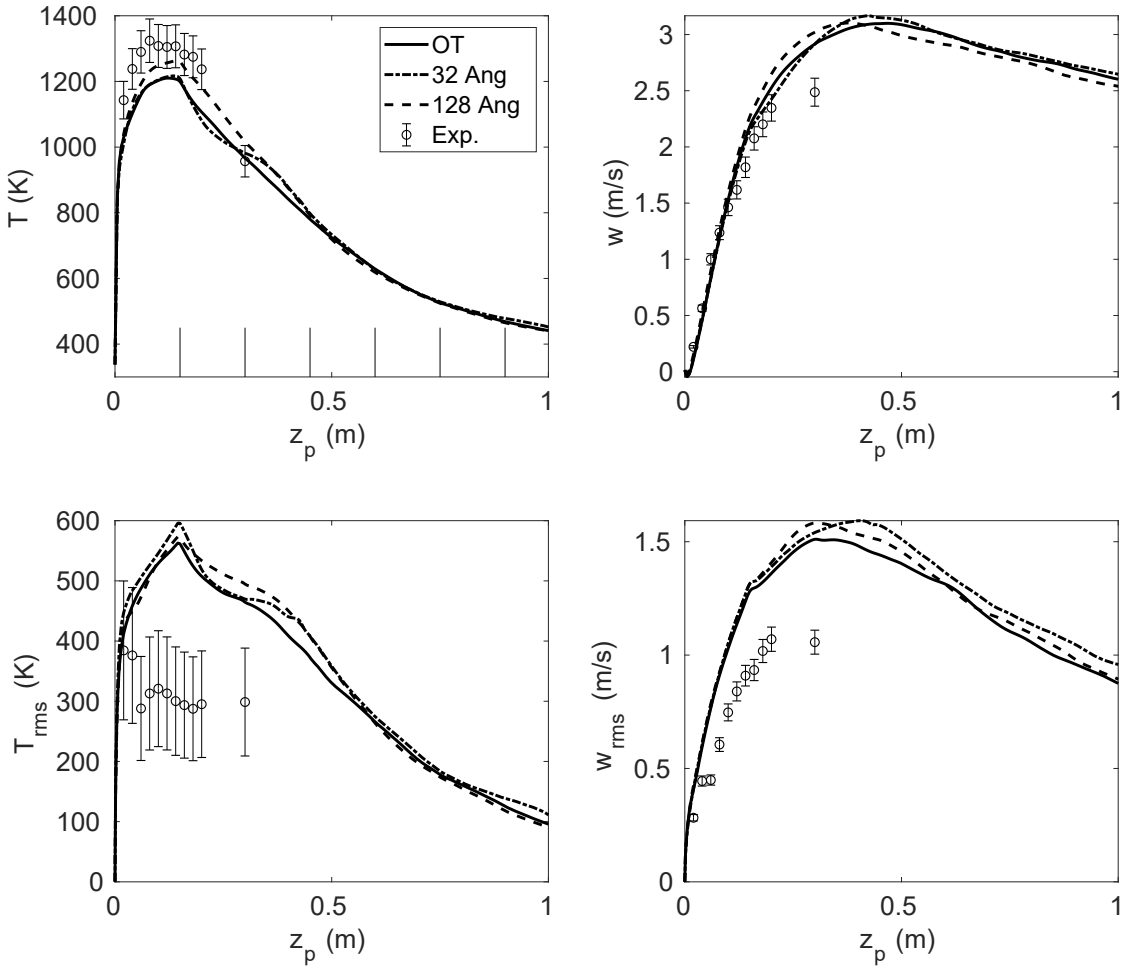


Figure 5.5: Centerline variation of the time averaged (upper) and rms (lower) temperature and axial velocity along the domain centerline. Solid lines optically thin radiation (OT), dashed-dotted lines solution of the RTE with 32 angles, and dashed lines solution of the RTE with 128 angles. Error bars represent experimental uncertainty. Vertical lines on the x-axis indicate the ensembles interfaces. Experimental data taken from Weckman and Strong [10].

In the third case which solves the RTE with 128 angles, the numerical time-averaged peak temperature falls within the experimental uncertainty. The location of the maximum temperature point in the simulations is approximately 14 cm above the pool surface which is higher than the location in the experiments.
An overprediction can be noted in the time-averaged vertical velocity at the last axial locations at $z_p = 30$ cm from the inlet of approximately 18%. This is also noted in the time-averaged temperature predictions, but to a much lesser extent as the centerline temperature is overpredicted by only 6% at this location.
The predicted temperature rms values do not agree as well. This can be explained in part by the expected higher level of uncertainties in the rms measurements, which were not given in the experiments, but are estimated to be in the range of 25%-30% [189, 10]. The rms bars are added with 30% uncertainty following what is selected in [178]. Overall, the three simulated cases show similar results which suggests that the optically thin approximation is reasonable for the current scale of fire. Still, predictions are improved with the inclusion of the RTE solution with 128 angles.
In comparison to previously published results, the maximum time-averaged temperature value and location in the simulations by Ahmed et al. [20] and Ma et al. [43] agree well with the current predictions. However, the near pool centerline temperatures up to 10 cm above the fuel surface are closer to the experimental measurements in the current results. The results by Hubbard et al. [181] show larger underpredictions in the region close to the pool and lower maximum time-averaged temperature that occurs even farther downstream, at 20 cm from the pool surface. In the simulations by Maragkos et al. [178] the maximum time-averaged temperature and its location are closer to the measurements, but there is a more notable overprediction in the centerline temperature at 30 cm from the inlet and higher overprediction in time-averaged vertical velocity as well.

Figures 5.6 - 5.9 show the radial variation of the temperature, axial velocity and radial velocity at different axial locations from the pool surface. The general trends in mean predicted values are in good agreement with the measurements and the simulated flame width matches the measured value at different stations. In Figures 5.6 and 5.7, there is an underprediction in the mean temperature localized around the centerline region above the pool surface at 2 cm and 6 cm from it. The predictions improve in the downstream region. This may in part be due to the constant and uniform evaporation rate used in the simulation, and potentially could be improved by defining the evaporation as a function of the thermal feedback to the fuel surface which may better mimic the physical process in a real fire. However, the pool surface would still be flat in the simulations while it was reported in the experiments to exhibit a standing wave of a frequency with about 2.0 Hz due to interactions between the gas pulsations and the free surface of the liquid fuel [12].
In Figure 5.6, the velocity at 2 cm from the fuel surface shows high radial unsteadiness

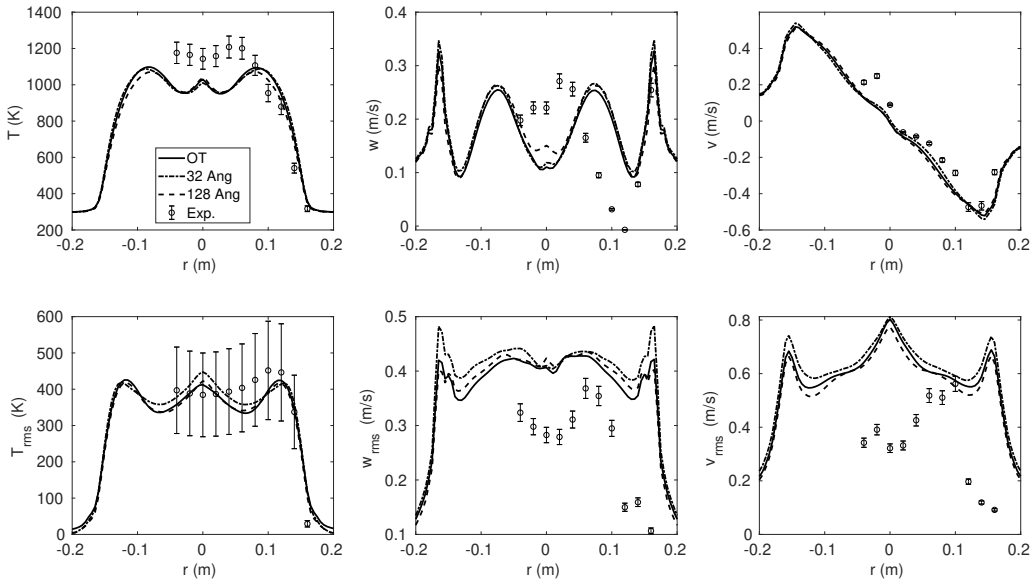


Figure 5.6: Radial variation of the time averaged (upper) and rms (lower) temperature, axial velocity, and radial velocity at 2 cm from the fuel surface. Experimental data taken from [10]. Same legend as in Figure 5.5.

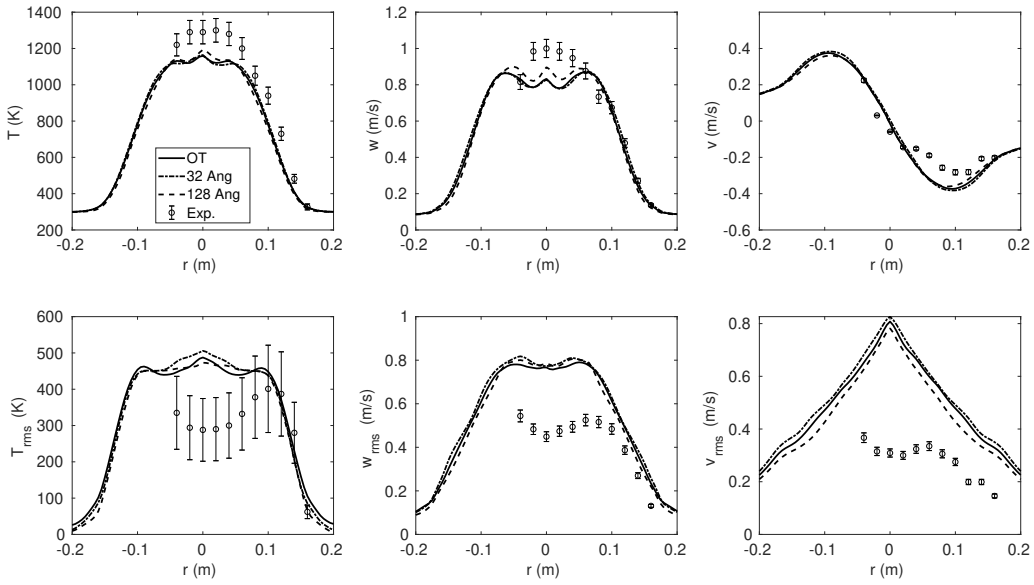


Figure 5.7: Radial variation of the time averaged (upper) and rms (lower) temperature, axial velocity, and radial velocity at 6 cm from the fuel surface. Experimental data taken from [10]. Same legend as in Figure 5.5.

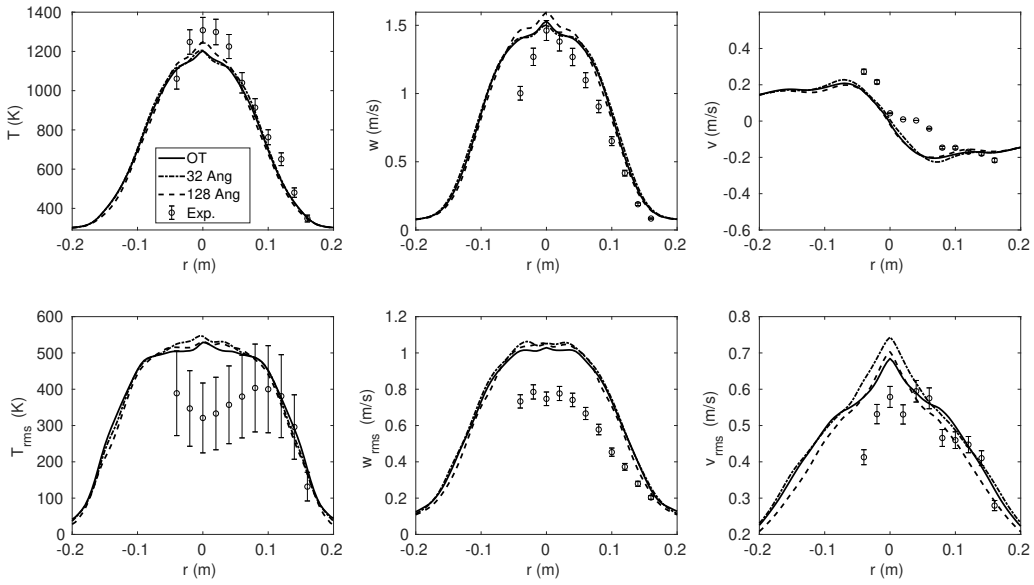


Figure 5.8: Radial variation of the time averaged (upper) and rms (lower) temperature, axial velocity, and radial velocity at 10 cm from the fuel surface. Experimental data taken from [10]. Same legend as in Figure 5.5.

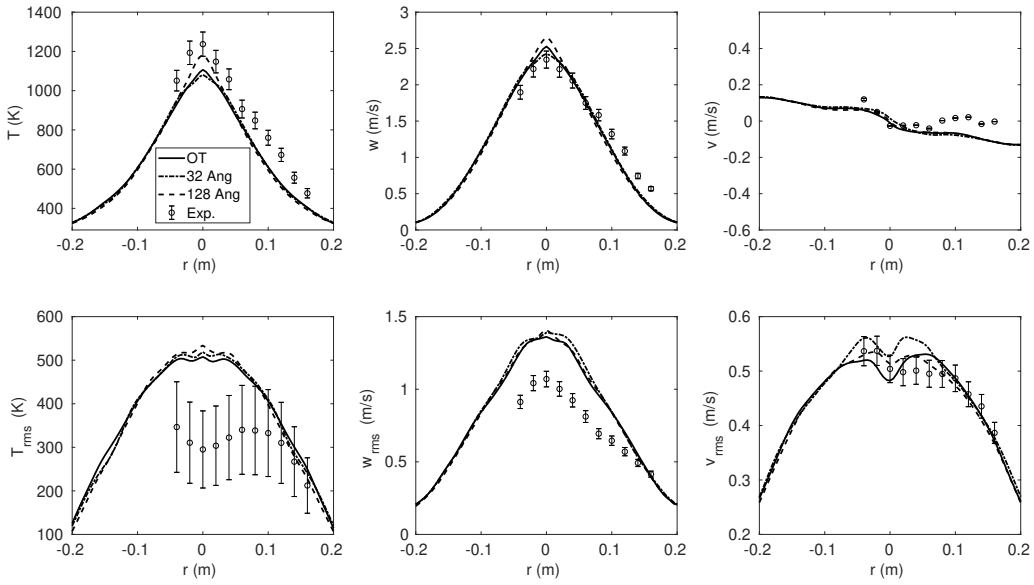


Figure 5.9: Radial variation of the time averaged (upper) and rms (lower) temperature, axial velocity, and radial velocity at 20 cm from the fuel surface. Experimental data taken from [10]. Same legend as in Figure 5.5.

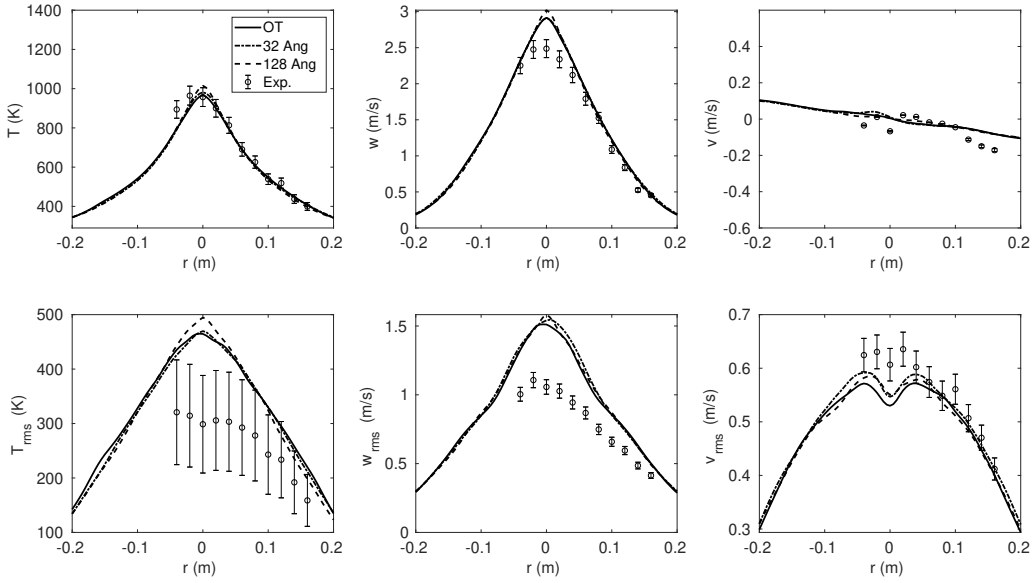


Figure 5.10: Radial variation of the time averaged (upper) and rms (lower) temperature, axial velocity, and radial velocity at 30 cm from the fuel surface. Experimental data taken from [10]. Same legend as in Figure 5.5.

which is reproduced in the simulations by a wavy pattern. There is a deeper decrease in the measured values at 12 cm from the center that is not reproduced in the simulations. Moving downstream, however, predicted time-averaged vertical velocities are more in alignment with the measured values with an overprediction at the last location 30 cm from the inlet. The time-averaged radial velocity predictions are in overall good agreement with the experimental measurements indicating that the entrainment is well predicted. The estimated radial velocity rms values agree with measured ones in the region near the surface but become underpredicted in the downstream locations.

Time-averaged species mole fractions

The time-averaged centerline species mole fractions of CH_3OH, O_2, CO_2, H_2O, CO and H_2 species are shown in Figure 5.11 and compared with the experimental values [11]. Overall, the three cases present only slight variations in the species mole fraction predictions and their trends agree well with the experimental profiles. The predicted fuel mole fraction rapidly decreases from the inlet and is almost totally consumed within 20 cm from the pool surface in agreement with the experimental profile. However, the rate of decrease is higher in the simulations compared to the experiments. Due to combustion, O_2 is consumed in the flame region and the O_2 mole fraction increases with downstream distance approaching the value in ambient as more air is entrained into the fire plume. Although the predicted rate of increase of O_2 is high near the fuel surface, the O_2 mole fraction becomes underpredicted in the downstream region which may be explained by the underprediction in the radial velocity rms in the downstream locations. Higher radial velocity rms values would enhance mixing with ambient air and decrease the height required for O_2 mole fraction to reach the ambient value. The mole fractions of CO_2 and H_2O increase in the flame region, as expected and then decay in the plume region as they mix with the entrained air. The predicted peak of CO_2 is lower than that in the experiments by 12%, while the numerical peak of H_2O mole fraction is within the experimental uncertainty. The CO and H_2 profiles show a rapid rise near the inlet where the mixture is fuel rich, following the experimental trend. Farther downstream, these minor species are depleted as the mixture gets leaner and reactions with the excess O_2 taking place. In comparison to the reported experimental values, the CO mole fraction peak is underpredicted, while that of H_2 is in good agreement with the measurements taking into consideration the experimental uncertainty. No radial profiles of chemical species are available in the experimental investigations.
The variation between the measurements and the simulation results may be explained by the uncertainties in the measurements which, for example, can reach about 50% for the values of fuel and water mole fractions [175] close to the pool. Further, the modeled case

prescribed fuel mass flow rate is 1.067 g/s based on what is reported by Weckman et. al [10]. This is higher than the value of 0.8579 g/s reported by Falkenstein-Smith et al. [11] in the experiments for which the species mole fractions are measured. The possible effects of tabulated chemistry were also considered. Another tabulation technique, the flamelet generated manifold (FGM), was tested with different definitions for the progress variable [95]. However, the predictions did not improve and the technique was not investigated further.

Previously published simulations reporting species mole fraction distributions are limited. The results obtained by Ma et al. [43] show that the fuel mole fraction is overpredicted in comparison to the experiments and the current predictions. Their O_2 profile is overall underpredicted, which is also the case in the current simulation, but only after 15 cm from the fuel surface. The CO_2 mole fraction peak is underpredicted as well, but is closer to the measured values. This is also true for CO, however, the profile downstream of the peak is overpredicted in their simulations while it matches better the measurements in the current simulations. Maragkos et al. [178] reported the distributions of the major species only. Their results show overprediction in the fuel mole fraction profile, but are in closer agreement with the measurements than those in [43] and also present an underpredicted O_2 profile. In their study, an overprediction in the CO_2 mole fraction profile is noted reaching a maximum value of 0.075, in contrast with the current predictions and previous results [43]. It is worth noting that both of these previously published studies have compared their results with experimental measurements from a different source [158], older than the set used for comparisons in the current study [11]. The two sources display considerable variation in the reported measurements. For example, the value for O_2 and H_2O mole fractions at 20 cm from the inlet are 0.14 and 0.071 in [11], while they are 0.079 and 0.22 in [158], respectively.

Radiative heat flux

An additional case with 512 angles, referred to as Case-RTE512, is investigated to test the effect of angular resolution on the radiative flux results. The differences between predictions of temperature, velocity and mole fractions from Case-RTE128 and Case-RTE512 are very small without any impact on the analysis and conclusions presented previously. Figure 5.12(a) shows the distribution of radiative heat flux from the fire with height outside of the pool at radial position 0.6 m from the pool center. The results from Case-RTE32, Case-RTE128, Case-RTE512 and experimental measurements from [9] are included. As expected, the estimated values for Case-RTE128 and Case-RTE512 match better the experimental measurements in comparison to those of Case-RTE32. With the finest angular

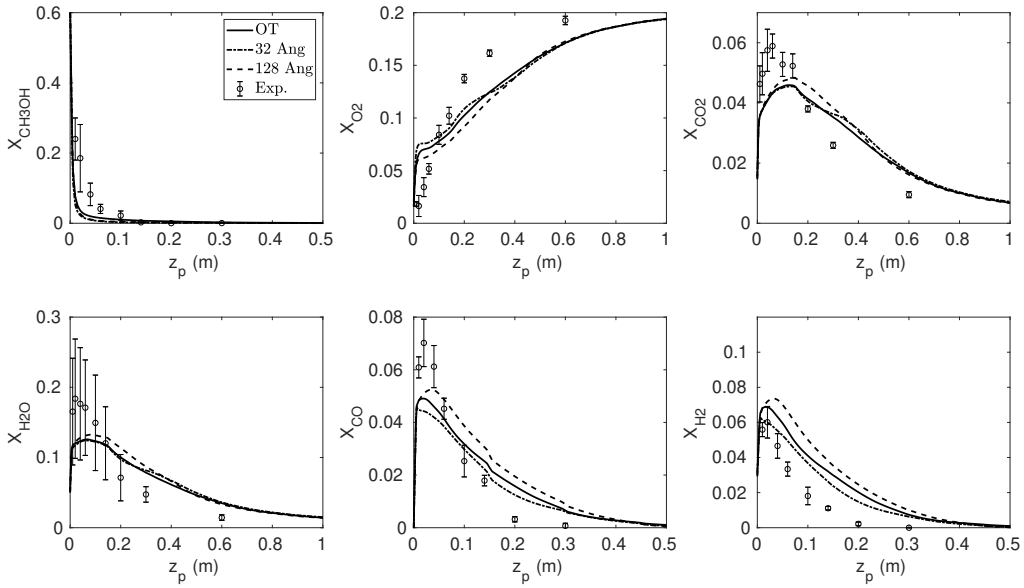


Figure 5.11: Centerline variation of the time averaged species mole fractions of (a) CH_3OH, (b) O_2, (c) CO_2, (d) H_2O, (e) CO, and (f) H_2. Experimental data taken from [11]. Same legend as in Figure 5.5.

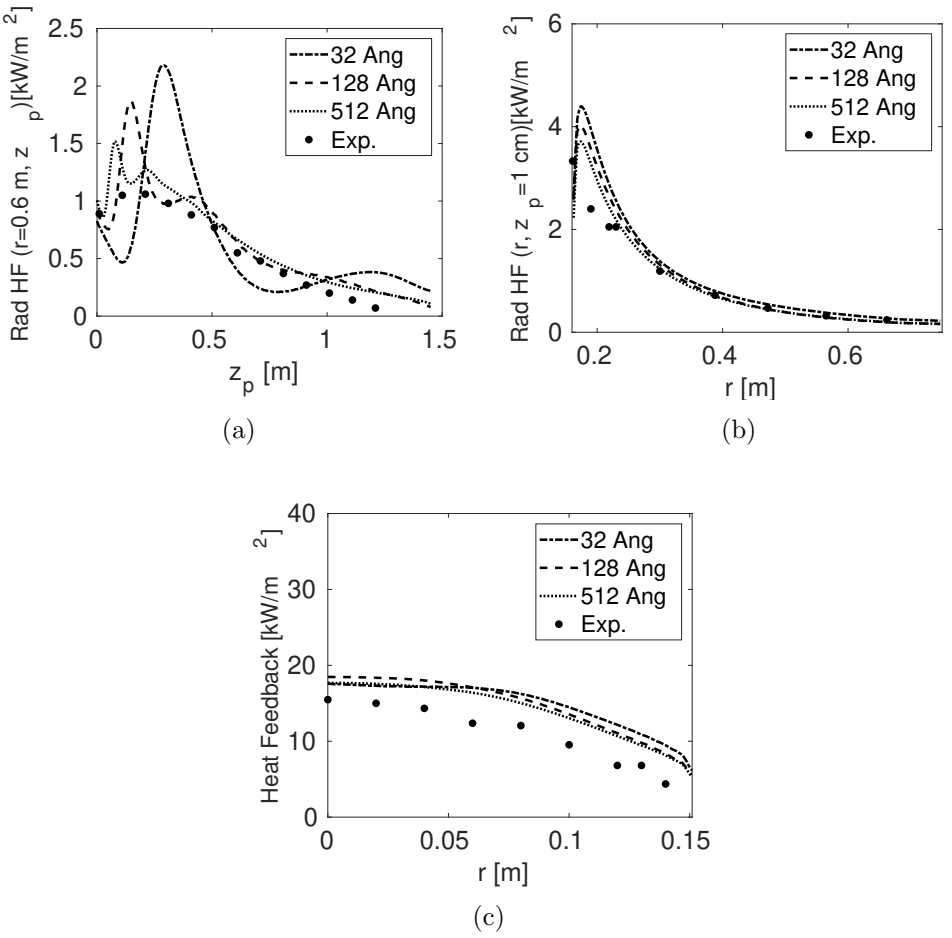


Figure 5.12: Estimated radiative heat flux in comparison to measured values: (a) Vertical distribution for flux in the radial direction at 0.6 m from the centerline (b) radial distribution for flux in the downward direction outside of the burner (c) radial distribution for flux in the downward direction over the pool surface. Experimental data taken from [9] except for (c) taken from [12]. Same legend as in Figure 5.5.

mesh, the predictions show a dip followed by a peak in the predictions in the first 0.2 m above the fuel followed by a smoother curve in the downstream. The peak is larger than the experimental value, but agreement improves in the downstream regions. In comparison, Case-RTE32 and Case-RTE128 display similar shapes, but spread over a longer height and show overall higher level of discrepancies along most of the curve to the outlet. In Figure 5.12(b), the variation in radiative flux in the downward direction radially along a line extending from the burner rim is shown in comparison to experimental measurements [9]. For all cases, radiation is overpredicted near the burner in comparison to the measurements, but the results get closer moving away from the burner. However, with the angular mesh refinement, the prediction of the peak value is enhanced and matches the experimental measurement more closely. Figure 5.12(c) shows the variation in radiative flux in the downward direction radially over the pool surface in comparison to the experimental measurements [12]. The measured values show that the radiative heat feedback is highest at the pool center and decreases moving radially to the burner wall. This behavior is replicated in the predicted values with all angular meshes which are close to each other and overpredicted in comparison to the measurements. This may be explained by the difference in lip height between the current simulated case of 1 cm and that reported for the measured case to be 0.5 cm [12].

The behavior of the different heat flux profiles discussed above is similar to a previous study by Ma et al. [43] which implemented the RCFSK instead of the WSGG in the current model. Their results overpredict the flux as well at 0.6 m from the centerline, but instead of the localized peak shown in Figure 5.12(a), their results show a similar degree of overprediction that is extended over a wide distance up to $z_p = 0.5$ m. In addition, the predictions of the radiative flux variation radially out of the pool in Figure 5.12(b) are closer to the experimental measurements, while those in [43] show a higher degree of overprediction. For the radiative flux over the pool, the predictions from both studies are similar.

Examining the three distributions, the differences between the predictions using the different angular meshes are high outside the flame region, but the results from all meshes are similar near the flame. This agrees with previous suggestions that a finer angular grid is required for better radiative flux predictions outside of the flame region only [190]. The current model does not account for methanol radiation in the calculation of the absorption coefficient which is a possible contributing factor for the discrepancies shown.

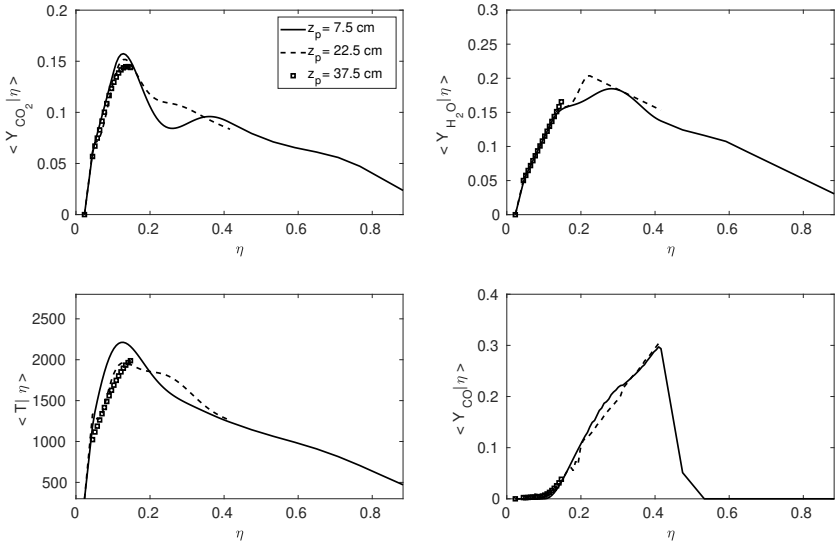


Figure 5.13: Conditional averages of mass fractions of CO_2, H_2O, and CO as well as temperature at 7.5, 22.5 and 37.5 cm from the inlet.

Conditional averages

Figure 5.13 shows the conditional averages of mass fractions of CO_2, H_2O and CO as well as temperature at at three axial locations within the predicted flame height for Case-RTE128. As can be seen, the conditional mass fractions of CO_2 and temperature rise until reaching their peak value around the stoichiometric mixture fraction of 0.135 and then decrease for fuel rich mixtures. The peak of the conditional mass fractions of H_2O is slightly on the fuel rich side, but the trend is similar. For CO, the values are nearly zero for the fuel lean mixtures corresponding to regions of excess air where complete combustion is reached. For larger mixture fraction values greater than the stoichiometric value, the conditional mass fraction of CO increases, as expected due to fuel rich conditions.
When moving downstream, the fuel air mixture becomes more fuel lean due to turbulent mixing with surrounding air. Thus, farther downstream, there is less meaningful statistical information obtained through the FDF for the integral inversion performed for the conditional mass fractions of CO_2 and H_2O. This does not affect the unconditional averages as the FDF tends to zero for these η values. For example, at $z_p = 37.5$ cm, the peak value of $\tilde{Z}$ is around 0.15 and therefore, limited to no statistical information is available for fuel rich mixtures that may introduce some inaccuracies in the conditional profiles. No experi-

mental conditional values are available for comparison for the present study, however, the trends are similar to those found in a previous RANS-CSE methanol flame study [84]. The conditional profiles do not vary much with axial distance, noting that the results from the three axial locations are extracted from three different ensembles. This small spatial variation in the conditional averages was also seen in previous investigations for turbulent flames far from extinction [32, 159].

5.3 Large-scale methanol pool fire

In this section, the coupling between CSE and RTE solution is applied to a large-scale methanol pool fire [13] to further assess the capabilities of this new approach. The numerical predictions are compared with available experimental measurements of temperature and radiative fluxes.

5.3.1 Experimental setup

The large-scale methanol pool fire is considered for simulations in the current section as reported in [13]. It is one of the MaCFP target experiments [177]. The fuel evaporates to the domain from a pool of 100 cm diameter featuring a burner rim of 1 cm. The burner is placed such that the rim is 0.3 m above the ground. The methanol mass flow rate is 12.8 $\pm$ 0.9 g/s which corresponds to an ideal heat release rate of 254 $\pm$ 19 kW [13]. The time-averaged and rms values of temperature are measured in the flame axially and radially at several locations. Radiative heat flux measurements are also available outside the fire region [13] and over the pool surface [14]. Soot production is negligible in this case and is not modeled in the current study.

5.3.2 LES setup

The LES solver selected in the current study is FireFOAM, based on the open-source package OpenFOAM-7 [25]. The sub-grid scale (SGS) turbulence is treated using the constant Smagorinsky model [59] with the model constants set as $C_k = 0.02$ and $C_\epsilon = 1.048$.
The computational domain is cylindrical in shape with a 2.5 m radius and 4.0 m height, as shown in Figure 5.14. The fuel pan is set such that the pool surface is 29 cm above the ground and features a rim height of 1 cm as set in the experiments. The grid cell size is equal to 1 cm over the pool region in all directions. In the axial direction, this grid size is

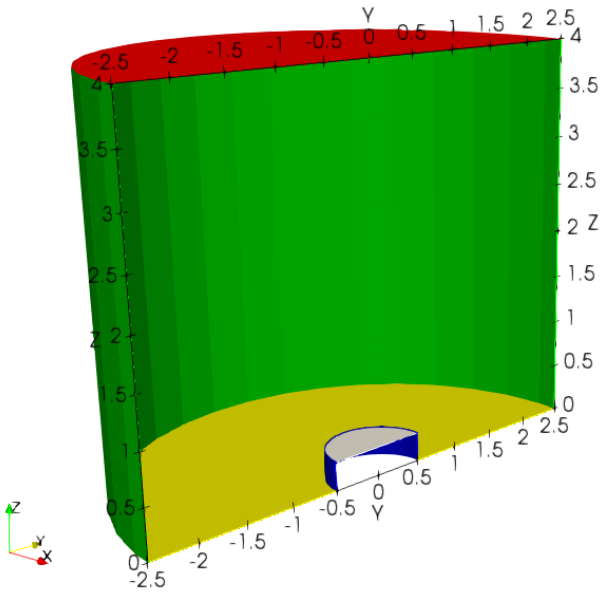


Figure 5.14: Computational domain sectional view for large scale methanol pool fire case showing the fuel pan with the burner lip at the center, and the overall domain dimensions in meters. The fuel inlet is in grey, domain outlet in red, and entrainment boundary in green.

kept up to a height of 150 cm from the surface of the pool then increased to 2 cm up to a height of 250 cm then stretched away in the rest of the domain. The total number of cells is 1,965,078. For the solution of the RTE, an angular mesh of 128 angles is considered. This exceeds the recommendation by the MaCFP working group of 100 angles resolution [177].
For the inlet surfaces, the mass flow rate is set to 12.8 g/s to match the reported experimental value [13] and is released as a vapour at the methanol boiling temperature of 337.8 K. The inlet boundary condition for the scalars accounts for both advection and diffusion fluxes. At the sides and outlet boundaries, a zero gradient is imposed for all scalars. The pressure and velocity are determined from the total hydrostatic pressure if the flow leaves the domain. In case of flow reversal, the pressure is reduced by the dynamic pressure.
The simulations are conducted for a minimum burning time of 40 seconds. To ensure that the initialization phase does not impact the results, data collection does not begin until after 15 seconds to avoid any impact caused by the transient phase at the start of the simulations.
The LES solver uses implicit time integration with a second order backward scheme and the time step is based on the maximum Courant number which is set to be 0.8. For CSE, the number of ensembles is equal to 30 dividing the domain as slices in the axial direction and clustered near the inlet. The ensembles begin at the pool surface and do not extend to the lower sides of the burner, as no reactions are anticipated in those areas. This is because the fuel evaporates from the pool surface and combusts further downstream. The mixture fraction space is discretized in 70 bins clustered around the stoichiometric value (0.135).

5.3.3 Results

In Figure 5.15, instantaneous snapshots of the experimental and simulated flame surfaces are presented. The experimental flame snapshots are obtained from a photographic view of the visible light emission at time instances during the flame cyclic pulsing [13]. The simulated flame surface is defined by the iso-contour of the volumetric heat release rate of 200 kW/m^3. The experimental flame is blue in colour indicating that no soot is produced. Both the experimental and simulated flames experience strong puffing behavior common in pool fires. Different stages of the buffing cycle is shown in the images. At the start, the flame appears confined to the near pool region. Next, both the experimental and simulated flames appear to develop in the downstream direction with the near pool flame region becoming necked and the flame getting confined around the center. In the final

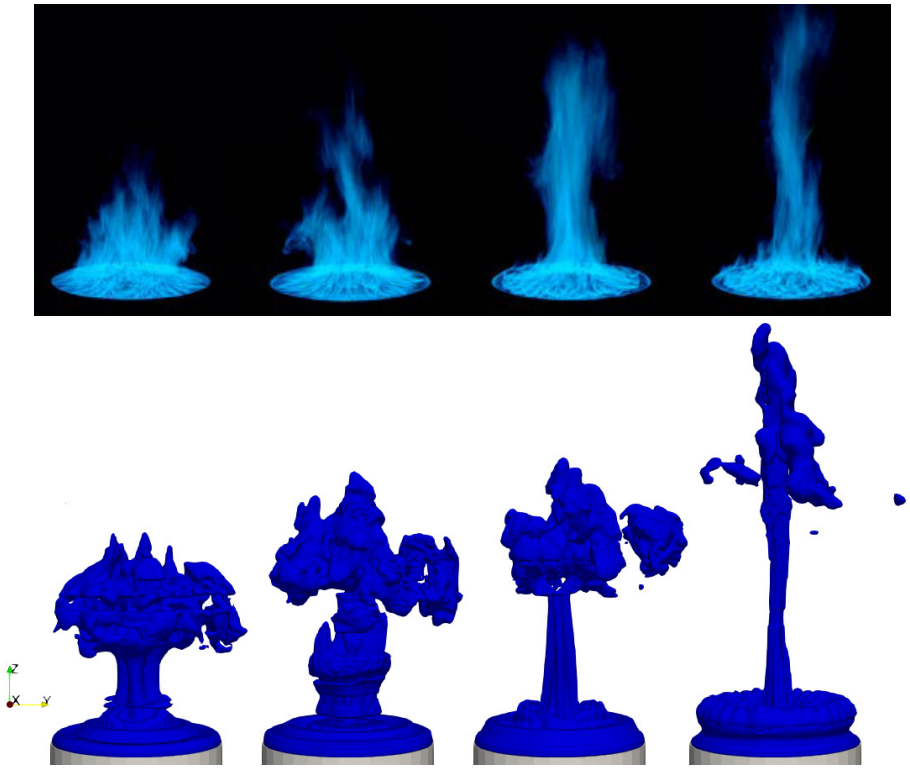


Figure 5.15: Comparison between the experimental flame surface (upper) obtained from [13] and the simulated flame surface defined as an iso-contour of the volumetric heat release rate of 200 kW/m^3 (lower). For both the experimental and numerical snapshots flames at different stages are shown.

stage, the flame becomes so elongated that it extends about two times the pool diameter in the axial direction.
The puffing frequency is estimated to be 1.26 Hz by applying fast Fourier transform to the time history of the axial velocity at a height of 0.64 m from the pool surface. The value is in good agreement with the reported value of 1.37 Hz in the experiments estimated from the video recording of the fire [13]. It also agrees well with the 1.25 Hz value reported in the previously published LES study of the same case [34].

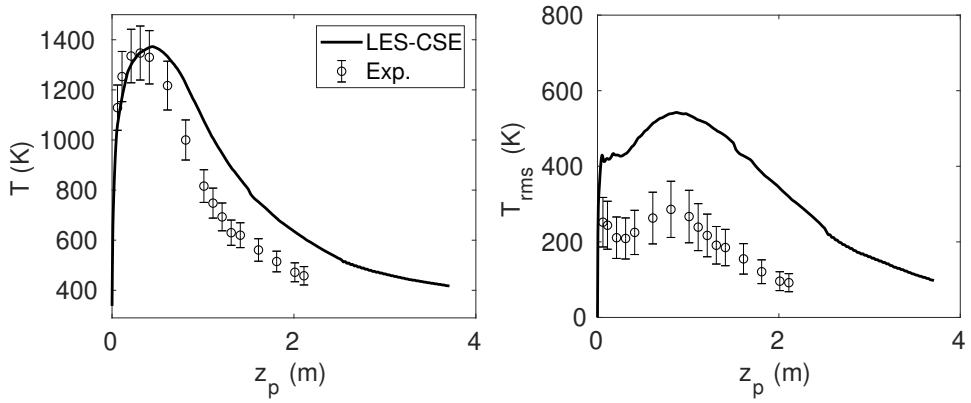


Figure 5.16: Vertical variation of temperature along centerline: left time-averaged values, right rms values. Experimental values taken from [13]. Error bars represent experimental uncertainty.

The time averaged centerline temperature profile along the axial direction is presented in Figure 5.16 as a function of the elevation from the fuel surface (z_p). The predicted temperatures increase from the fuel inlet value to a peak value. Then, farther downstream the predicted temperature decreases which is typical in the buoyancy driven flames. Experimental data shows that the time-averaged temperatures rise from the inlet to a peak value of about 1350 K at 0.31 m above the fuel inlet. Then, the experimental centerline temperatures gradually decrease. Similarly, the predicted time-averaged temperatures increase to reach a peak of 1372 K which is within the experimental uncertainty. In the downstream of the peak, the temperature measurements as well as the predictions drop with same rate up to about 80 cm from pool surface. Farther downstream, the results are overpredicted as they decrease more slowly than the measurements.
The predicted rms values shown in Figure 5.16 do not agree as well. This can be explained in part by the higher level of uncertainty in the rms measurements which is estimated in

the experiments to be about 26%.

Similar observations are found in the radial temperature profiles, as shown in Figure 5.17 at axial locations 20 cm, 60 cm and 100 cm from pool surface as well as in Figure 5.18 at 140 cm and 180 cm from pool surface. In general, the profiles show that the predictions are in agreement with the measurements. However, there is an overprediction in the time-averaged temperatures near the centerline in the downstream location as shown previously. The predictions are more accurate at the sides and show that the width of the flame is well predicted at different locations. The T_{rms} profiles show that the values are overpredicted near the centerline but get closer to the measurements at the periphery.

Figure 5.19(a) illustrates the distribution of radiative heat flux from the fire with height outside the pool at a radial distance of 2.07 meters from the pool center. The data reveals an initial dip followed by a peak within the first 0.9 meters from the fuel level. This peak is higher than the experimental measurements. Further downstream, another peak is observed, though it is of a smaller magnitude compared to the first. The predictions in these downstream regions show better alignment with the experimental data. In Figure 5.19(b), the variation in radiative flux in the downward direction radially along a line extending from the burner rim is depicted and compared to experimental measurements [13]. The results indicate that the model overpredicts the radiative flux near the burner when compared to the experimental data. However, as the distance from the burner increases, the predictions become more accurate, gradually converging with the experimental measurements.
Figure 5.19(c) presents the variation in radiative flux in the downward direction radially over the pool surface compared to experimental measurements from [14]. The experimental data shows that the radiative heat feedback is highest at the pool center and decreases as one moves radially towards the burner wall. This trend is successfully replicated in the model's predictions, although there is a slight underprediction of about 9% compared to the experimental values. This underprediction indicates that while the model captures the overall trend accurately, it slightly underestimates the radiative heat feedback across the pool surface.
The predictions of the different heat flux profiles discussed above are similar to those presented by Nmira et al. [34]. Their results overpredict the flux as well at 2.07 m from the centerline as in Figure 5.19(a) but to a lower level. The remaining radiative flux predictions are close to the current presented values.
Similar to the observations from the results of the medium scale case in Section 5.2.2 the current results reveal that the differences between the predictions and the measurements are higher outside the flame region, but get closer near the flame. This implies that a finer angular mesh resolution is required for out of the flame predictions since a fine angular grid is required for better radiative flux predictions outside of the flame region [190]. The fuel

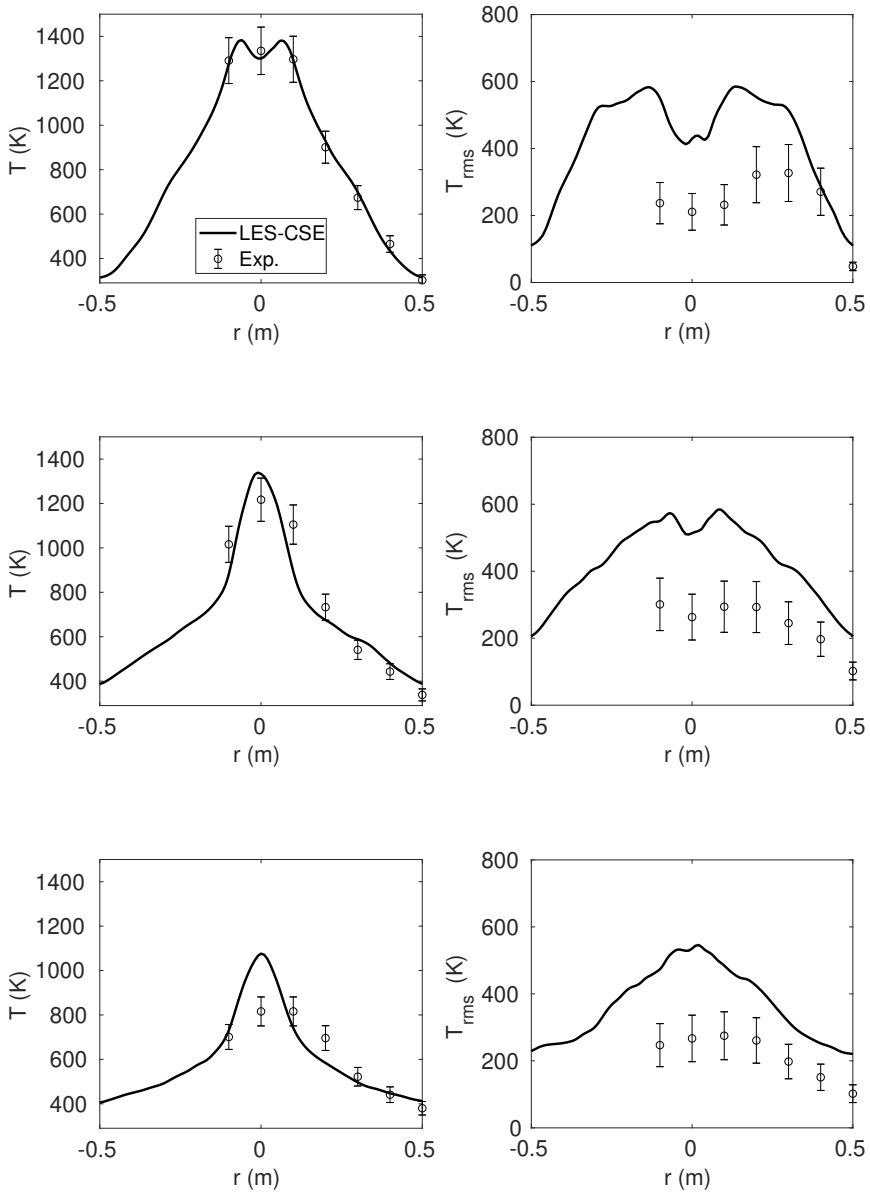


Figure 5.17: Radial variation of the time-averaged (left) and rms (right) temperature at z_p=20 cm (upper), z_p=60 cm (middle), and z_p=100 cm (lower). Experimental values taken from [13]. Error bars represent experimental uncertainty. Same legend as in Figure 5.16

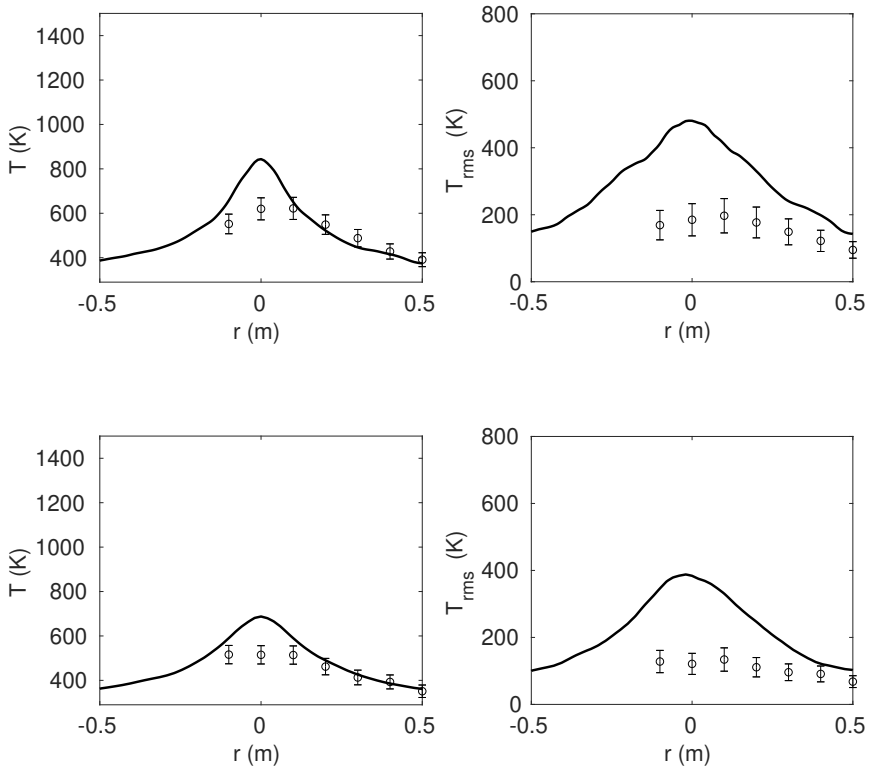
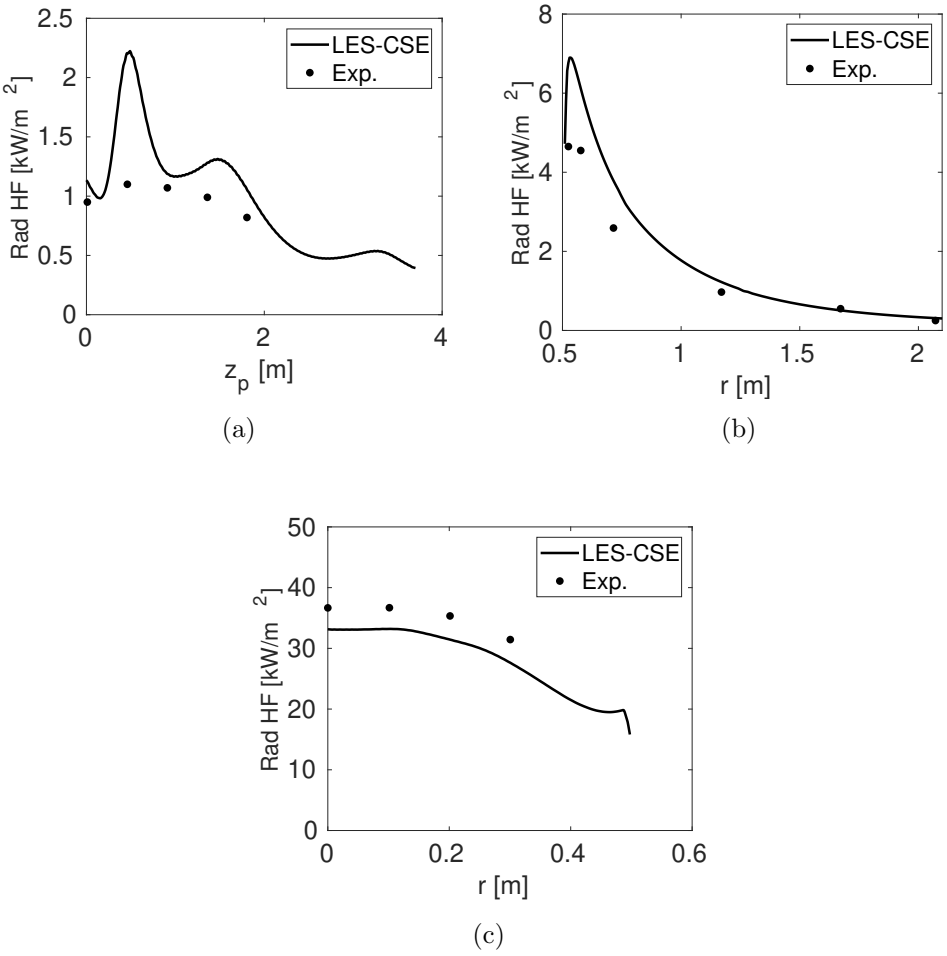


Figure 5.18: Radial variation of the time-averaged (left) and rms (right) temperature at z_p=140 cm (upper), and z_p=180 cm (lower). Experimental values taken from [13]. Error bars represent experimental uncertainty. Same legend as in Figure 5.16



(a) (b)

(c)

Figure 5.19: Estimated radiative heat flux in comparison to measured values: (a) Vertical distribution for flux in the radial direction at 2.07 m from the centerline (b) radial distribution for flux in the downward direction outside of the burner (c) radial distribution for flux in the downward direction over the pool surface. Experimental data taken from [13] except for (c) taken from [14].

radiation is not accounted for in the calculation of the absorption coefficient in the current model which is a possible source of discrepancies shown in the radiative flux results.

5.4 Summary

The LES FireFOAM solver coupled with the CSE approach is applied to model medium and large scale methanol pool fires. For the medium scale scenario, the radiation is treated first with the optically thin assumption and then compared with results that account for absorption by solving the RTE using the finite volume discrete ordinate method with coarse and fine angular resolutions. In all cases, the WSGG model is used to estimate the absorption coefficients and TRI are accounted for. Among the three investigated cases, the results are close, but the case that solves the RTE with 128 angles shows closer predictions to the measurements in general. Flame height and radiative fraction match the experimental values within experimental uncertainty. The predicted puffing frequency is found to be slightly lower, at 2-2.1 Hz in comparison to 2.6-2.8 Hz in the experiments. The current time-averaged temperature predictions are in good agreement with the experimental measurements, except at the centerline close to the pool surface. This observation is found in previous simulations as well and may be explained by the fixed prescribed mass flow rate boundary and modeling the pool to have a flat surface. For the remaining locations, the predictions are in reasonable agreement with the measurements and reproduce well the flame width at different axial positions. The centerline species mole fraction distributions show that there is a general agreement in the trends, but there are some discrepancies in the downstream region of the fire. Some of these discrepancies may be explained by the dissimilarity in the fuel evaporation rate between the experimental setup used to measure the species mole fraction and the base one investigated in the current simulations as well as experimental uncertainties. The close predictions from the different radiation modeling approaches indicate that the optically thin approximation is reasonable for the medium scale fire. For the radiative flux, it is shown that the predictions align better with the measurements with the finer angular mesh outside of the flame region, while the results from both angular meshes are in agreement within the flame, meaning that, a coarse angular mesh is adequate to estimate the near flame region radiative fluxes, but a finer one is required farther away from the pool fire. The current model does not account for the methanol contribution in the radiation calculation which is a possible source of discrepancy in the radiative flux results.
For the large scale fire, the results are shown for CSE coupled with the solution of RTE with an angular mesh of 128 angles. The finite volume discrete ordinate method is used

for solution of the RTE combined with the weighted sum of grey gases while accounting for TRI similar to what is employed in the medium scale case. The time-averaged temperature predictions are in good agreement with the experimental measurements, except on the centerline downstream of the flame region where the results are overpredicted and show a slower rate of decrease than what is observed in the experiments. The radiative heat flux results show that, the differences between the predictions and the measurements are higher outside the flame region, but get closer near the flame. This implies that the current angular mesh resolution is not fine enough for out of the flame region since a fine angular grid is required for better radiative flux predictions outside of the flame region.

This first LES-CSE coupling with the solution of the RTE is an important step for further developments of the CSE framework to study more complex fire cases with detailed chemistry. Further research will consider pool fire with different fuel such as ethanol with soot production to examine the expected larger benefits using the sgs combustion and radiation models implemented in the current work.

Chapter 6

Investigation of soot modeling in LES of a medium-scale ethanol pool flame coupled with CSE approach

Soot emission plays a crucial role in influencing flame radiation and the concentration of toxic products in non-premixed flames. This is particularly important in understanding fire behavior and safety measures. Soot, being a primary component of smoke from fires, significantly reduces visibility. Consequently, complicating evacuation efforts during fire-related incidents, making it more challenging for individuals to find safe exits. Moreover, soot inhalation is a major health concern as it can cause respiratory diseases. The environmental impact of soot is also significant, as it contributes to air pollution and can affect climate patterns by absorbing sunlight and warming the atmosphere. Additionally, in large hydrocarbon fires, smoke shielding becomes a critical factor. The presence of dense smoke can block emitted radiation from escaping, which in turn affects the overall fire dynamics. This interaction between chemical reactions in fires, buoyancy-driven flow of hot gases, and radiation can lead to more intense and unpredictable fire behavior.
In Chapters 4 and 5, soot modeling was not included in studying the different cases since the flames were non-sooting. The aim of this chapter is to enhance the comprehensive CSE framework by integrating it with two widely used laminar smoke point based soot models in LES of pool fires for the first time. This new approach will be evaluated by simulating a medium-scale ethanol pool fire. Experimental measurements of different flow quantities including temperature, species mole fractions and radiative fluxes for this case are available in [11, 175, 9]. Soot is modeled in two ways based on laminar smoke point concept. The first model calculates the laminar soot formation and oxidation rates then provides a

correction to account for turbulent effects. The second one calculates soot reaction rate in the conditional space based on analytical functions in mixture fraction and conditional temperature then integrates it with filtered density function to obtain filtered reaction rate. Predictions of the time-averaged and root mean square temperature, in addition to species mole fractions and soot mass fraction profiles, are compared with the experimental measurements.
The current study is the first one that focuses on this pool fire. It is also the first one to study turbulent buoyant diffusion flames using CSE approach while accounting for soot modeling. Previous studies investigating soot formation in turbulent buoyant diffusion flames relied on EDM/EDC models for combustion closure [146, 147, 148].
The numerical predictions are compared with existing experimental measurements of time-averaged temperature and their root mean square (rms) values. The distributions of species mole fractions and soot mass fraction in the axial direction as well as radiative heat flux measurements at different locations are also examined and compared with available experimental data.

6.1 Soot modeling

Soot is modelled using two approaches based on the LSP concept. In both approaches, a transport equation for soot mass fraction is solved as

$$\frac{\partial(\overline{\rho}\tilde{Y_s})}{\partial t} + \frac{\partial(\overline{\rho}\tilde{u_i}\tilde{Y_s})}{\partial x_i} = \frac{\partial}{\partial x_i}\left(\overline{\rho}\left(D_s + D_t\right)\frac{\partial \tilde{Y_s}}{\partial x_i}\right) + \overline{\dot{\omega}_s}, \tag{6.1}$$

where $\tilde{Y_s}$ is the filtered soot mass fraction, $\overline{\dot{\omega}_s}$ the filtered soot source term, D_s the laminar soot diffusivity taken as 1% of the gas diffusivity following previous studies [191, 146]. This lower value compared to the gaseous species can be explained by the soot particles being much heavier and larger than gas molecules. The soot source term is estimated by modelling both soot formation and oxidation process separately then finding the resultant as

$$\overline{\dot{\omega}_s} = \overline{\dot{\omega}_{s,f}} - \overline{\dot{\omega}_{s,o}}, \tag{6.2}$$

In both models, soot formation and oxidation rates are determined directly from flow variables, rather than being linked to precursor species. The models are generalized for various fuels by correlating the peak soot formation rate with the fuel LSP height, which is 0.225 m for ethanol [141] in the present work. Further, both approaches assume that, when normalized by the stoichiometric mixture fraction, the regions in mixture fraction space

where soot formation and oxidation occur are the same for all fuels. The dependence on specific soot surface area is also neglected in both the formation and oxidation source terms. The two models differ primarily in how they describe the dependence of soot formation and oxidation on flow variables, and the LES extension of the initial laminar formulation to account for turbulence soot interactions is also treated differently.

- First soot model

The first approach used for modelling $\overline{\dot{\omega}_s}$ in the current study is based on the model developed by Beji et al. [49] for laminar non-premixed flames and extended for turbulent LES fire simulations by Chen et al. [146]. In this model, the laminar soot formation is estimated as

$$\dot{\omega}_{s,f} = \frac{4.4E-6}{L_{sp}} \rho^2 Y_f T^{2.25} e^{-2000/T}, \qquad Z_{st} \leq Z \leq 2.5 Z_{st}, \tag{6.3}$$

where L_{sp} is the laminar smoke point height [141], Y_f the fuel mass fraction, Z is the mixture fraction and Z_{st} the stoichiometric mixture fraction. To account for the turbulence effects on soot formation, the partially stirred reactor concept is applied [192, 146]. A given computational cell is assumed to be composed of reacting and non-reacting zones and the filtered soot formation rate can be estimated by providing a correction to the laminar soot formation calculated from the filtered flow variables as

$$\overline{\dot{\omega}_{s,f}} = m_r \dot{\omega}_{s,f}(\overline{\rho}, \tilde{Y}_f, \tilde{T}), \tag{6.4}$$

where m_r is the mass fraction of the reacting zone in a given computational cell and can be expressed as

$$m_r = \frac{\tau_{c,s}}{\tau_{c,s} + \tau_{mix}}, \tag{6.5}$$

where $\tau_{c,s}$ is the chemical time scale and τ_{mix} is the turbulent mixing time scale. The chemical time scale is assumed to be proportional to the laminar smoke point height

$$\tau_{c,s} = C_{sp} L_{sp}, \tag{6.6}$$

where C_{sp} is a constant derived based on the characteristic soot production time scale for an ethylene flame [193] and is equal to 0.364 s/m. The mixing time scale, τ_{mix}, is approximated to be the geometric mean of the largest and smallest flow time scales as

$$\tau_{mix} = \sqrt{\frac{\nu^{1/2} k}{\epsilon^2}}, \tag{6.7}$$

where k and ϵ are the total turbulent kinetic energy and its dissipation rate [146], respectively.
The soot oxidation rate is modelled such that it takes place in a region that has sufficient oxygen and close to the flame surface [146, 49] as

$$\overline{\dot{\omega}_{s,o}} = \overline{\rho}\tilde{Y}_s\dot{m}^* \frac{(L^*/L^{'})^{0.2}(\tilde{Z}/Z_{st})}{1-(L^*/L^{'})^{0.2}(\tilde{Z}/Z_{st})}, \qquad 0 \leq \tilde{Z} \leq Z_{st} \text{ and } \tilde{T} \geq 1300K, \tag{6.8}$$

where $L^{'}$ is the characteristic fire plume length scale [194], $\dot{m}^*$ is the mass transfer rate between the fine structures where soot oxidation takes place and the surrounding fluid defined as

$$\dot{m}^* = \left(\frac{3}{C_{D2}}\right)^{1/2}\left(\frac{\epsilon}{\nu}\right)^{1/2}, \tag{6.9}$$

and L^* is the characteristic length of the finest turbulent structures defined as

$$L^* = \frac{2}{3}\left(\frac{3C_{D2}^3}{C_{D1}^2}\right)^{1/4}\left(\frac{\nu^3}{\epsilon}\right)^{1/4}, \tag{6.10}$$

where C_{D1} and C_{D2} are constants equal to 0.5 and 0.75, respectively.

- Second soot model

In the second approach, the laminar soot model proposed by Lautenberger et al. [15] is implemented. The turbulence interactions are accounted for in the soot source term by first estimating the soot production source term in conditional space then integrating with the FDF to obtain the filtered quantity required in Eqs. 6.1 and 6.2.
The conditional soot formation and oxidation rates are estimated as the product of analytical functions of mixture fraction and temperature

$$\langle\dot{\omega}_{s,f}|\eta\rangle = f_{s,f}(\eta)g_{s,f}(\langle T|\eta\rangle), \tag{6.11}$$

$$\langle\dot{\omega}_{s,o}|\eta\rangle = f_{s,o}(\eta)g_{s,o}(\langle T|\eta\rangle), \tag{6.12}$$

where $\langle\dot{\omega}_s|\eta\rangle$ is the soot reaction rate, $f_s(\eta)$ the mixture fraction analytical function, $g_s(\langle T|\eta\rangle)$ the temperature analytical function, the subscript f denotes formation and o corresponds to oxidation. The function shapes are based on soot formation rate map obtained from experimental measurements of non-premixed ethylene flame [136]. The map shows that formation rate trends are approximately parabolic functions in each of mixture fraction and temperature. Thus, the mixture fraction soot formation function is assumed

to be a third order polynomial. The function coefficients are determined by specifying the start point of function, η_L, the end point, η_H, the location of the peak, η_P, and its value, $f_{s,f}(\eta_P)$. The temperature soot formation function is obtained through the same approach normalized between zero and unity. The same is also true for the mixture fraction soot oxidation function. However, the soot temperature oxidation function, $g_{s,o}$, is assumed to be linearly proportional to temperature starting from a critical value for simplicity.
Each mixture fraction function start, end and peak points are parameterized by the stoichiometric mixture fraction, η_{st}, as

$$\eta_i = \psi_i \eta_{st}, \; i = L, H, P \tag{6.13}$$

where ψ_i is a constant, L denotes start point, H denotes end point and P denotes peak point. The different parameters that define the four functions are listed in Table 6.1. The

Table 6.1: Soot formation and oxidation function parameters for the second soot model from [15]

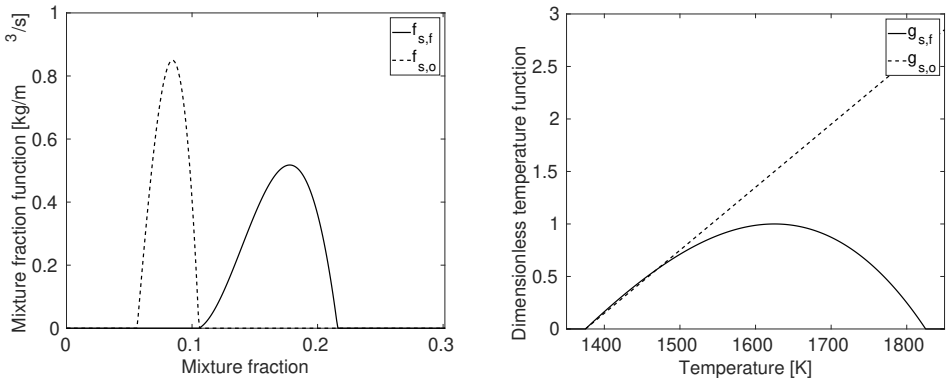
Parameter	Soot formation	Soot oxidation
ψ_L	1.05	0.56
ψ_P	1.77	0.84
ψ_H	2.15	1.05
$f(Z_P)$	$1.1(0.106/L_{sp})$ kg/m^3s	-0.85 kg/m^3s
T_L	1375 K	1375 K
T_P	1625 K	-
T_H	1825 K	-
$dg_{s,o}/dT$	-	0.006 K^{-1}

.

parameters were initially optimized for an ethylene flame. However, soot peak formation is parameterized by the fuel LSP height to accommodate different fuels other than ethylene [15]. The final functions for the current case are shown in Fig. 6.1.

6.2 Radiation modeling

Radiation is treated by assuming the medium to be non-scattering. The total absorption coefficient is calculated as the summation of the gas and soot absorption coefficients. The radiation absorption is accounted for by solving the RTE for an absorbing-emitting medium following what was done in Chapter 5. The weighted sum of grey gases (WSGG) model



(a) (b)

Figure 6.1: (a) Mixture fraction functions Eq. 6.11 and Eq. 6.12 and (b) Temperature functions for Eq. 6.11 and Eq. 6.12. In both, solid line is for soot formation and dashed line is for oxidation.

[116] is used to estimate the gas absorption coefficient. The WSGG parameters for mixtures of CO_2 and H_2O were originally based on experimental data but derived here from recent correlations based on HITEMP [195].
The soot absorption coefficient is calculated following the approach in [196] as

$$\kappa_{soot} = \rho Y_{soot}(1232.4 + 0.59155(T - 2000.0)) \tag{6.14}$$

where κ_{soot} is the soot absorption coefficient and Y_s is the soot mass fraction. The soot contribution is then included by adding the soot absorption coefficient to that of the gas to obtain the total absorption coefficient, $\kappa_T = \kappa + \kappa_{soot}$.
The TRI effects are considered by first calculating the total absorption coefficient and the emission term in conditional space and then integrating them with the FDF as

$$\overline{\kappa_T} = \overline{\rho} \int_0^1 \frac{1}{\langle \rho|\eta \rangle} \langle \kappa_T|\eta \rangle(\eta, t)\tilde{P}(\eta, x_j, t)d\eta, \tag{6.15}$$

$$\overline{\kappa_T I_b} = \overline{\rho} \int_0^1 \frac{1}{\langle \rho|\eta \rangle} \langle \kappa_T I_b|\eta \rangle(\eta, t)\tilde{P}(\eta, x_j, t)d\eta. \tag{6.16}$$

In the current study, the finite-volume discrete ordinates method is selected as well for the solution of the RTE where the intensity is assumed to be constant over discrete parts of the total solid angle 4π.

6.3 Computational details

6.3.1 Experimental setup

The current study investigates the medium scale ethanol pool fire, as reported in [9, 11]. This pool fire is one of the target experiments in the MaCFP working group under the NIST pool fires subgroup. The pool diameter is 30 cm elevated above the ground such that the fuel surface is 29 cm from the floor. A 1 cm lip height is maintained during the experiments. The ethanol mass burning flux is reported to be 13.9 ± 0.8 g/m^2/s which corresponds to a heat release rate of 26.3 ± 1.5 kW. The time-averaged and rms values of temperature are measured in the flame at several locations along the centerline. In addition, the species mole fraction and soot mass fraction centerline measurements are provided for the same case as well as radiative heat flux measurements at different locations [9, 11].

6.3.2 LES setup

Following what is employed in Chapters 4 and 5, the LES calculations are carried out using a customized version of the FireFOAM solver [25]. This solver is built upon the open-source CFD package OpenFOAM. FireFOAM employs a finite volume approach and incorporates a variable density LES formulation, offering various modeling choices for handling turbulence, combustion, and radiation.

The computational domain takes the form of a cylindrical shape with a diameter of 1.5 m and a height of 1.75 m along the z-direction, as shown in Figure 6.2. Positioned 0.29 meters (approximately one pool diameter) above the ground, the fuel inlet placement is equivalent to that in the experiments. Additionally, the burner features a 1 cm lip height, replicating the experimental setup described in [9, 11]. Maintaining the observed rim height during experiments in pool fire simulations is crucial for achieving accurate results, as illustrated previously [43].

In the pool region, the grid cell size is 5 mm up to a height of 62 cm from the pool surface. Beyond that height, the grid is stretched across the rest of the domain. This mesh resolution adheres to the MaCFP recommendation [177] for this scenario and aligns with previously published LES studies on similar pool fires [180, 179, 42, 178]. The mesh consists of 755,202 cells. For this study, the Smagorinsky model [59] is employed to handle subgrid-scale (SGS) turbulence, with model constants $C_k = 0.02$ and $C_\epsilon = 1.048$. Implicit time integration using a second-order accurate backward scheme is applied in the LES solver. Spatial discretization of convective terms utilizes the Total Variation Diminishing (TVD) scheme called limitedLinear, while a second-order central difference scheme is used

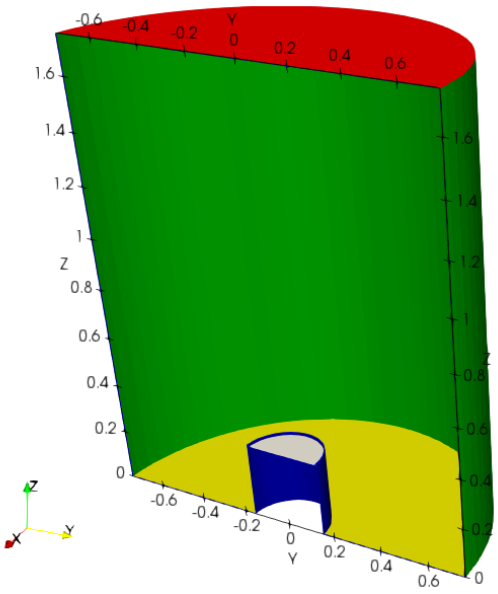


Figure 6.2: Sectional view of computational domain with fuel pan at the center and dimensions in meter. The fuel inlet is in grey, domain outlet in red, entrainment boundary in green, fuel pan side wall in blue and ground in yellow.

for diffusion terms. In all cases, simulations are conducted with a minimum burning time of 35 seconds. To ensure that the initialization phase does not affect the results, data collection begins only after the first 10 seconds. The simulation time step is approximately 0.5 milliseconds, controlled by the Courant number set to 0.8.
The mass flow rate is set at the inlet surface to match what is reported experimentally. For the scalars inlet boundary conditions, both advection and diffusion fluxes are accounted for. At the lateral and outlet boundaries, scalar gradients are set to zero. When flow exits the domain, the total hydrostatic pressure governs both pressure and velocity. In the event of flow reversal, the pressure is adjusted by the dynamic pressure. This adjustment helps mitigate potential instability arising from sudden velocity increases, as the driving pressure gradient is also decreased [25].
To solve the RTE, an angular mesh with 128 angles is set, satisfying the MaCFP working group's recommended resolution of 100 angles for this scenario [177]. Further, prior simulations of pool fires at a similar scale utilized angular meshes with 64 [20], 72 [178], and 128 angles [181].

6.3.3 CSE details

For the CSE calculations, the LES domain is divided into ensembles of computational cells in the form of axial slices split into two halves. The ensembles are 15 cm in height, equivalent to half of the pool diameter, in the first 90 cm from the pool surface. For the remaining part of the domain, the ensemble height is 27.5 cm. The ensembles do not extend below the pool surface on the sides of the burner. No reactions are expected in this region of space since the fuel evaporates from the pool surface and combustion starts farther downstream.
The effect of heat losses in the flame on the tabulated conditional reaction rates and mass fractions is included by incorporating non-adiabatic tables. Different sets of tables with different levels of enthalpy loss are generated starting from the adiabatic conditions. The tables are labeled by the absolute enthalpy defined as the sum of species formation enthalpy and the sensible enthalpy. The tables are generated at different levels by multiplying the adiabatic enthalpy, which has a negative value, by a coefficient starting from 1.1 up to 6.0. To determine the enthalpy level during the simulations, an additional transport equation is solved for the adiabatic enthalpy ($\widetilde{h_{ad}}$) similar to Eq. 2.20, but without the radiation loss term. Then, the filtered enthalpy loss is calculated as the difference between the sensible enthalpy and the adiabatic one $\widetilde{h_{loss}} = \widetilde{h_{ad}} - \widetilde{h}$. The conditional enthalpy loss ($\langle h_{loss}|\eta\rangle$) is then obtained from the filtered values through integral inversion and used as one of the parameters in the chemistry tables. The resulting TGLDM tables are four dimensional,

mixture fraction, enthalpy loss and mass fractions of CO_2 and H_2O.
The mixture fraction space is discretized in 50 bins clustered around the stoichiometric value (0.1). To determine $\langle Y_{CO_2}|\eta\rangle$, $\langle Y_{H_2O}|\eta\rangle$ and $\langle h_{loss}|\eta\rangle$, three inversions are performed in each ensemble for each variable and two additional inversions are performed for $\langle T|\eta\rangle$ and $\langle Y_s|\eta\rangle$ needed for radiation modelling. Conditional reactions rates of major species (ethanol (C_2H_5OH), oxygen (O_2), CO_2 and H_2O) are retrieved from the TGLDM tables as well as mass fractions of minor species (carbon monoxide (CO), hydrogen (H_2) and hydroxide (OH)). Eq. 3.25 is applied to calculate the unconditional values by integrating the conditional values with the FDF over η space.
The numerical predictions from three cases are presented next. For comparison, one LES calculation does not include any soot modelling (first case), but is otherwise configured the same as the two cases with soot models included. The other two set of simulations include soot models using the two approaches discussed in section 6.1.

6.4 Results

6.4.1 Flame structure

Instantaneous snapshots of both experimental and simulated flame surfaces are shown in Figure 6.3. The experimental flame snapshots are captured through visible light emission photography at two distinct time instances during the flame cyclic pulsing [9]. The flame surface obtained from the first case of the simulations is defined as an iso-contour of the volumetric heat release rate (200 kW/m^3). These snapshots reveal interesting flame dynamics. Initially, both experimental and simulated flames appear confined in a region close to the pool surface. However, in the subsequent view, they exhibit an attached base near the pool surface followed by formation of an elongated tube-like flame structure. Downstream, larger flame puffing structures emerge due to buoyancy-driven motions. In addition, small flame pockets appear detached from the main combustion zone in both the experimental and simulated flames.
The flame height is estimated to be 62 cm based on the axial point at which the time-averaged temperature exceeds that of the ambient by 550 K beyond the maximum temperature point [124]. The prediction is within the reported value of 61.1 ± 28.2 cm in the experiments, for which, the measured value is based on processing video recorded frames of the experiments [11]. Further, the pulsation frequency is determined in the simulations by performing a Fourier transform on the time history of vertical velocity at a distance of 0.36 meters from the pool surface along the centerline. The estimated value is 2.48 Hz.

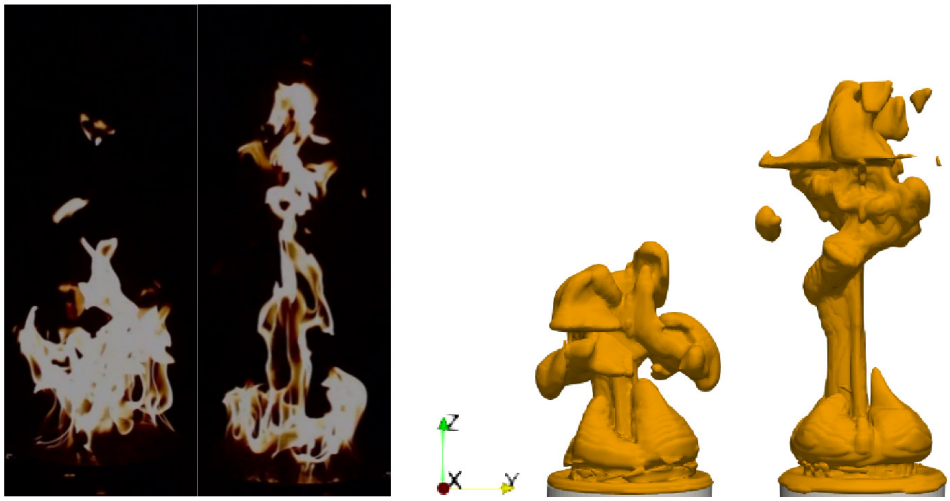
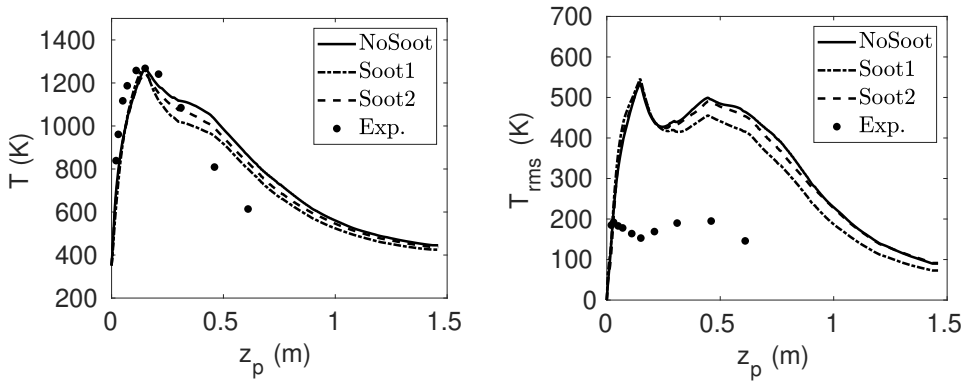


Figure 6.3: Comparison between flame shapes. The left side shows the experimental flame surface, taken from reference [9]. The right side shows the simulated flame surface defined as an iso-contour of the volumetric heat release rate of 200 kW/m^3. Snapshots display high and low flames at different time instants.

There is no direct measurement of the pulsation frequency for the current case. However, the estimated value closely aligns with findings from experiments involving pool fire at the same scale, but fueled by methanol. The pulsation frequency is estimated from the video analysis of those experiments to be 2.8 ± 0.3 Hz in [12] and 2.65 ± 0.08 Hz in [188]
The radiative fraction is estimated from the simulations by evaluating the equation $\chi_{rad} = \int \overline{\dot{Q}}_{rad} dV / \int \overline{\dot{Q}}_{react} dV$. In the case with no soot modelling, the radiative fraction is approximately 0.28, while it is estimated to be slightly higher with values of 0.35 with the first soot model and 0.32 with the second soot modelling approach. These values are in good agreement with the experimentally measured value of $0.26 \pm 25\%$ [9].

6.4.2 Temperature

Figure 6.4 shows the centerline variation of the temperature with height above the pool surface. Both the time-averaged and the root mean square (rms) variations are presented. Simulation results are shown for a case without any soot modelling as well as with soot accounted for using the two models discussed before in comparison to measurements from experiments [11]. In both figures, z_p is the axial height measured from the pool surface (29 cm from the ground). In the experiments, the measured time-averaged temperature rises



(a) (b)

Figure 6.4: Centerline variation of the time averaged (left) and rms (right) temperature along the domain centerline. Solid lines case without soot modelling, dashed-dotted lines solution with the first soot model, and dashed lines solution with the second soot model. Experimental data taken from [11].

from the inlet until reaching a peak of 1268 K at 15 cm from the pool surface then starts decreasing. For the case without soot modelling, the results show that the time-averaged temperatures are slightly underpredicted near the inlet close to the pool surface until reaching the peak temperature point where it is close to the measured value. Downstream from the peak, in the plume region, temperatures decrease at a slower rate than that of the experiments and there is an overprediction of nearly 28% at 46 cm from the fuel surface compared to the measured value. With the inclusion of soot, the variation in the time averaged temperature is small. However, the case with the first soot model shows improved temperature predictions compared to the other two cases: the temperature peak agrees well with the experimental value and the downstream profile is also closer to the experimental measurements. The predicted rms values do not align with experimental values as well. This discrepancy can be attributed, in part, to the anticipated higher uncertainty associated with rms measurements. Previous experiments estimated this uncertainty to exceed 25% [189].

6.4.3 Species mole fractions

The time-averaged centerline species mole fractions of C_2H_5OH, O_2, CO_2, H_2O, CO and H_2 species are shown in Figure 6.5 and compared with the experimental values [11]. The

predictions show general agreement with the trends of the experimental measurements. The three simulated cases present only slight variations in the species mole fraction predictions. The predicted fuel concentration rapidly decreases from the inlet and is almost totally consumed within 30 cm from the pool surface. However, the rate of fuel consumption is lower than that observed from the measurements and the simulations overpredict the centerline fuel variation. Still, the predictions in the two cases including soot are closer to the measurements than the case without soot. Due to chemical reactions, O_2 is consumed in the flame region and the O_2 mole fraction increases with downstream distance approaching the value in ambient as more air is entrained into the fire plume. The mole fractions of CO_2 and H_2O increase in the flame region, as expected, and then decay in the plume region as they mix with the entrained air. The predicted peak of CO_2 matches the experimental value. The predicted peak of H_2O mole fraction also agrees with the measurements if the experimental uncertainty is considered. In the downstream region of the peak, the predicted rate of decay of both of CO_2 and H_2O concentrations is lower than that seen in the measurements. The CO and H_2 profiles show rapid rise near the inlet where the mixture is fuel rich, following the experimental trend. Farther downstream, they are depleted as the mixture gets leaner and reactions with the excess O_2 take place. In comparison to the reported experimental values, the CO mole fraction peak is within the reported uncertainty, while that of H_2 is overpredicted compared to the measurements taking into consideration the experimental uncertainty. No radial profiles of chemical species are available in the experimental investigations.
The variation between the measurements and the simulation results may be explained in part by the uncertainties in the measurements which, for example, can reach about 70% for the values of oxygen mole fractions as well as the minor species [175].

6.4.4 Soot mass fraction

The time-averaged centerline soot mass fraction distribution is shown in Figure 6.6 with the experimental measurements [11]. The peak soot mass fraction obtained from the first soot model is close to that in the measurements, albeit with an underprediction of approximately 29%. However, this discrepancy remains reasonable for soot predictions and considering the reported experimental uncertainty of 11%. With the second soot model, the results do not agree as well and there is a significant underprediction in the soot peak value. The peak soot location is measured at 14 cm from pool surface in the experiments, while it is predicted at 12 cm with the first soot model and only 9 cm with the second soot modelling approach. Farther downstream, the predictions from the first soot model become much larger than the experimental data and show a lower rate of decay compared

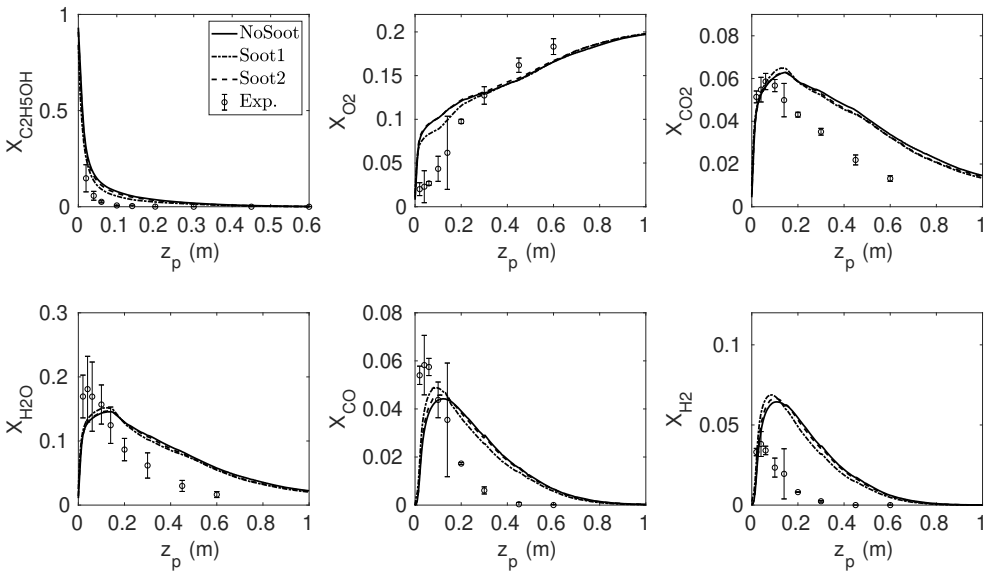


Figure 6.5: Centerline variation of the time averaged species mole fractions of (a) C_2H_5OH, (b) O_2, (c) CO_2, (d) H_2O, (e) CO, and (f) H_2. Experimental data taken from [11]. Same legend as in Figure 6.4.

to the experiments. In contrast, the low values from the second soot model are close to the measurements. The overall soot predictions obtained by model 1 are in closer agreement with experiments for the shape and magnitude of the centerline soot mass fraction in comparison to those from model 2.
One possible source of discrepancy, found in both models, is the lack of soot formation dependence on surface area that is likely more important in lightly sooting flames as with the case under consideration with ethanol as a fuel [15]. The two selected soot models do not account for such effect and consider only homogeneous soot formation. For this, solution of an additional transport equation for soot number density would be required or the different constants and functions used in the current approaches would need to be modified.
The variation in the soot predictions between the two models can be related to the model formulation. There are constants in both models that were originally calibrated for other fuels. The LSP height is introduced to account for the expected variation of the sooting level with changing of fuels. However, as can be noted in Table 6.1, the controlling parameters of soot oxidation rate in the second soot model are not parameterized by the LSP height. Although this is also true for the first soot model, the oxidation rate in this case shown in Eq. 6.8 is a function of the soot mass fraction providing a dependence on the sooting level of the case under consideration which may help adjust the oxidation level. Further, the turbulence soot interactions treatment is different, one governed by an EDC-PaSR formulation in model 1 and the other using the FDF and convolution over mixture fraction space. Considering the present results, the combined uncertainties found in model 2 have resulted in predicted soot mass fractions much lower than the experimental data in the region of high soot level for this fire.
Higher soot levels lead to higher radiation losses, consequently, lower temperature predictions. Therefore, the predictions of soot mass fractions are reflected in the temperature predictions previously discussed. For example, 46 cm above the fuel surface, the centerline temperature is lowered by 80 K with the first soot model and 42 K with the second model making it closer to the measured value. Still, the current effect of soot on temperature predictions is limited with inclusion of soot, even with the first model, since ethanol is a lightly sooting fuel. For example, the experimentally measured soot mass fraction in an acetone pool fire of the same scale is approximately five times that of the ethanol [11].

6.4.5 Radiative heat flux

Figure 6.7(a) shows the distribution of radiative heat flux from the fire with height outside of the pool at radial position 0.6 m from the pool center. The results from the three cases

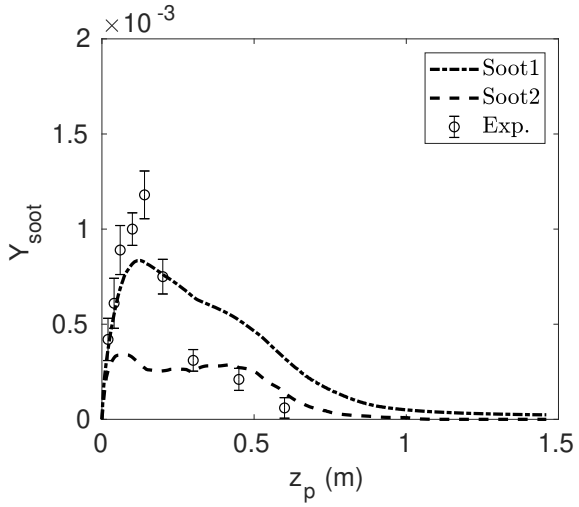


Figure 6.6: Centerline variation of the time averaged soot mass fraction. Experimental data taken from [11]. Same legend as in Figure 6.4.

and experimental measurements [9] are included. The predictions show a dip followed by a peak in the predictions in the first 0.2 m above the fuel followed by a smoother curve in the downstream. The peak is larger than the experimental value, but agreement improves in the downstream regions. The predictions are higher with the first soot model results than the other two cases which can be explained by the larger soot mass fraction predicted in this case. Moving downstream, this variation is less evident as the soot gets depleted.
In Figure 6.7(b), the radial variation in radiative flux in the downward direction along a line extending from the burner rim is shown in comparison to experimental measurements [9]. The radiative flux is overpredicted near the burner in comparison to the measurements, but the results get closer moving away from the burner.
Figure 6.7(c) shows the radial variation in total heat feedback in the downward direction over the pool surface in comparison to the experimental measurements [9]. The measured values show that the heat feedback is highest at the pool center and decreases moving radially to the burner wall. This behaviour is also replicated in the simulations, but with an overprediction near the center in comparison to the measurements. Moving away from the center the predictions get closer to the measurements.
The behaviour of the different heat flux profiles discussed above is similar to that of a previous study [43] simulating methanol pool fire of the same scale. Their results overpredict the flux as well at 0.6m from the centerline, but instead of the localized peak shown in Figure 6.7(a), their results show a lower degree of overprediction that is extended over a

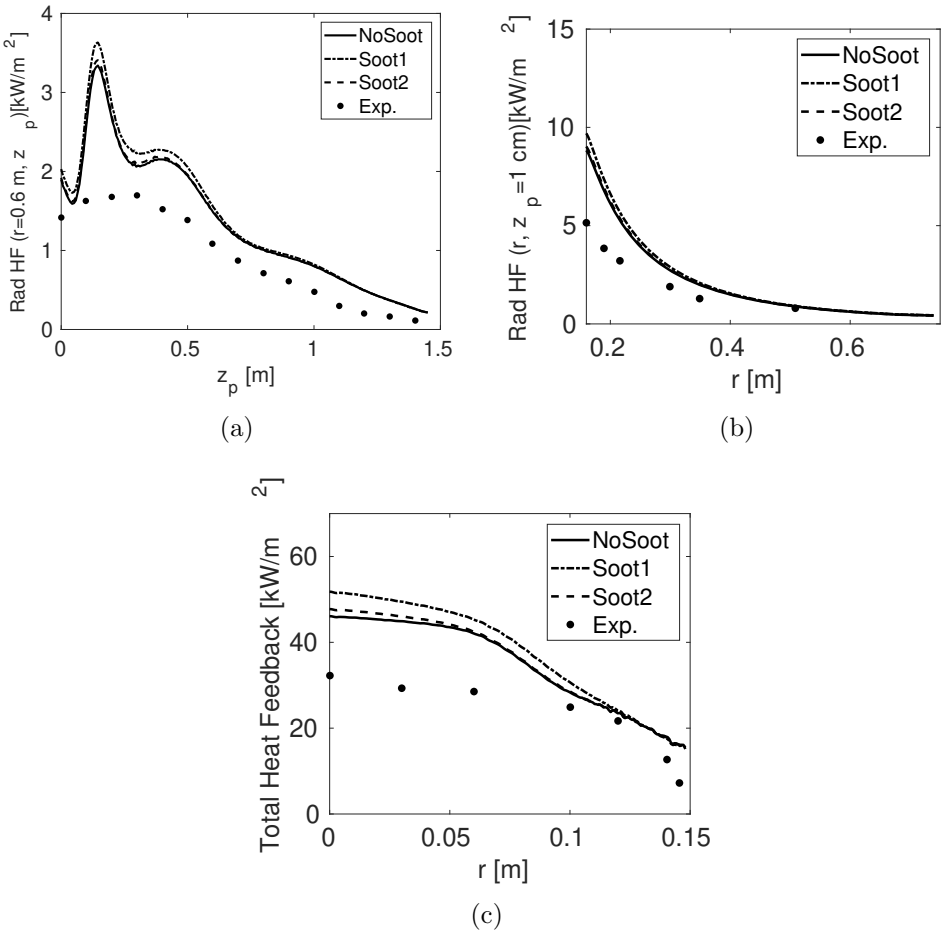


Figure 6.7: Estimated radiative heat flux in comparison to measured values: (a) Vertical distribution for flux in the radial direction at 0.6 m from the centerline (b) radial distribution for flux in the downward direction outside of the burner (c) radial distribution for total heat feedback over the pool surface. Experimental data taken from [9]. Same legend as in Figure 6.4.

wide distance up to $z_p = 0.5$ m. The rest of the radiative flux profiles are close to the current predictions.
The current model does not account for fuel radiation in the calculation of the absorption coefficient which is a possible contributing factor for the discrepancies shown. The use of a finer angular grid may lead to better radiative flux predictions but only outside of the flame region, as suggested previously [190].

6.5 Summary

The LES FireFOAM solver coupled with the CSE approach and soot modelling is applied to simulate a medium scale ethanol pool fire. Detailed chemical kinetics are accounted for through TGLDM tables with the inclusion of the effect of radiation heat loss. The radiation treatment accounts for absorption by solving the RTE using the finite volume discrete ordinate method and the WSGG model for estimating the gas absorption coefficients. Soot is modeled in two ways based on the LSP concept. The first model calculates the laminar soot formation and oxidation rates then provides a correction for turbulent effects. The second calculates soot reaction rates in conditional space based on the analytical functions and conditional temperature then integrates the conditional profiles with the FDF to obtain filtered rates. Three cases are investigated. The first case does not include soot modelling, while the other two account for soot through the two described soot models. The predicted flame height and radiative fractions are in agreement with what is reported experimentally. The time-averaged temperature predictions agree with the experiments as well. There is an overprediction in the plume region, away from the peak temperature that is smaller when the first soot model is applied. Species mole fractions are in general agreement with the measurements with some discrepancies observed in the products downstream of the peak which can be explained in part by the uncertainty in the measurements. The soot mass fraction peak is underpredicted by 29% using the first soot model. However, with the second soot model the values are notably underpredicted and the peak soot location is closer to the fire base in comparison to what is seen in the experiments. Although soot model 1 heavily relies on many empirical constants and relations, and includes simplified expressions based on EDC/partially stirred reactor concept, the current soot predictions are reasonable in the context of soot/fire simulations where large experimental uncertainties are found. In contrast, soot model 2 has not performed as well as soot model 1 for the present case. Soot model 2 includes a mixture fraction dependence for soot formation and oxidation through presumed functions making it more suitable for CSE formulation and explicit inclusion of turbulence soot interactions. As pointed out by Lautenberger et al.

[15], the larger discrepancies in soot mass fraction predicted by model 2 may be due to the lack of soot formation dependence on surface area, important in lightly sooting fuels such as ethanol, and the functions probably need more adjustment. This is difficult to conduct without additional experimental data.

The simulations overpredict the peak radiative flux away from the pool in the radial direction. However, the results become closer to the measurements moving downstream. The radiative flux in the downward direction is overpredicted as well near the burner wall and becomes in agreement with the measurements moving radially. The behaviour of the different heat flux profiles is similar to that of a previous study [43] simulating methanol pool fires of the same scale. The current model does not account for fuel radiation in the calculation of the absorption coefficient which is a possible contributing factor for the discrepancies shown.

The present work with simple soot models as part of a larger LES framework including detailed turbulent combustion and radiation models is a very first step towards incorporating more detailed soot models for pool fires exhibiting higher soot levels. Additional experimental fire data need to be examined for further validation.

Chapter 7

Conclusions

7.1 Summary of main findings

In Chapter 4, the LES FireFOAM solver coupled with the CSE approach is applied to the UMD buoyant turbulent flame including tabulated detailed chemistry and different approaches for radiation modeling. The current time averaged temperature predictions are in good agreement with the experimental measurements, except very close to the fuel inlet. The predicted temperatures increase more slowly compared to the experimental data in the first 0.09 m above the burner exit. The temperature rms is in reasonable agreement with experimental data with the peak rms being overpredicted by approximately 17%. Further, flame shape, unconditional and conditional quantities, axial velocity and mixture fraction are also examined for qualitative analysis and found to correspond to expected trends.
The current LES-CSE predicted temperature and rms compare well with previously published numerical results for the same flame. The present LES-CSE formulation does not incorporate any conditional space submodels that were problematic in previous LES-CMC. The effect of the calculation of the radiation term in the conditional domain to account for TRI is found to have an influence on the predicted maximum temperature: the peak is reduced by approximately 7% moving the predictions closer to the experimental data. However, the use of the non-adiabatic tables is found to show only slight effect on the predictions for the current case. The predicted flame height closely matches the experimental value. The calculated radiative fraction is found to be in agreement with the reported value in the experiments. However, the HRR is found to be larger than the experimental value of 50 kW. In the current work, the radiation modeling formulation relies on the optically thin assumption along with the Planck mean absorption coefficients calculated using RAD-

CAL. This is found to be reasonable for the selected case. This first LES-CSE provides a good foundation for further developments for more complex fire cases. The study can be extended to include more detailed models that account for absorption such as the finite volume discrete ordinate method combined with the weighted sum of grey gases. For this, the RTE will need to be solved, the conditional absorption coefficient may be calculated in conditional space as a function of conditional temperature and species concentrations like CO_2 and H_2O, the mean absorption may be determined by integrating the product of conditional absorption and FDF over mixture fraction space, similar to what is reported in [7] and the absorption TRI would be neglected, shown to be a reasonable assumption [161].

In Chapter 5, the LES FireFOAM solver coupled with the CSE approach and RTE solver is applied to model medium and large scale methanol pool fires. For the medium scale scenario, the radiation is treated first with the optically thin assumption and then compared with results that account for absorption by solving the RTE using the finite volume discrete ordinate method with coarse and fine angular resolutions. In all cases, the WSGG model is used to estimate the absorption coefficients and TRI are accounted for. Among the three investigated cases, the results are close, but the case that solves the RTE with 128 angles shows closer predictions to the measurements in general. Flame height and radiative fraction match the experimental values within experimental uncertainty. The predicted puffing frequency is found to be slightly lower, at 2-2.1 Hz in comparison to 2.6-2.8 Hz in the experiments. The current time-averaged temperature predictions are in good agreement with the experimental measurements, except at the centerline close to the pool surface. This observation is found in previous simulations as well and may be explained by the fixed prescribed mass flow rate boundary and modeling the pool to have a flat surface. For the remaining locations, the predictions are in reasonable agreement with the measurements and reproduce well the flame width at different axial positions. The centerline species mole fraction distributions show that there is a general agreement in the trends, but there are some discrepancies in the downstream region of the fire. Some of these discrepancies may be explained by the dissimilarity in the fuel evaporation rate between the experimental setup used to measure the species mole fraction and the base one investigated in the current simulations as well as experimental uncertainties in species concentrations. The close predictions from the different radiation modeling approaches indicate that the optically thin approximation is reasonable for the medium scale fire. For the radiative flux, it is shown that the predictions align better with the measurements with the finer angular mesh outside of the flame region, while the results from both angular meshes are in agreement within the flame, meaning that, a coarse angular mesh is adequate to estimate the near flame region radiative fluxes, but a finer one is required farther away from the pool

fire. The current model does not account for the methanol contribution in the radiation calculation which is a possible source of discrepancy in the radiative flux results.
For the large scale fire, the results are shown for CSE coupled with the solution of RTE with an angular mesh of 128 angles. The finite volume discrete ordinate method is used for solution of the RTE combined with the weighted sum of grey gases while accounting for TRI similar to what is employed in the medium scale case. The time-averaged temperature predictions are in good agreement with the experimental measurements, except on the centerline downstream of the flame region where the results are overpredicted and show a slower rate of decrease than what is observed in the experiments. The radiative heat flux results show that the differences between the predictions and the measurements are higher outside the flame region but get closer near the flame. This implies that the current angular mesh resolution is not fine enough for out of the flame region since a fine angular grid is required for better radiative flux predictions away from the flame.
This first LES-CSE coupling with the solution of the RTE is an important step for further developments of the CSE framework to study more complex fire cases with detailed chemistry. Further research will consider pool fire with different fuels such as ethanol with soot production to examine the expected larger benefits using the sgs combustion and radiation models implemented in the current work.

In Chapter 6, the LES-CSE framework coupled with soot modeling is applied to simulate a medium scale ethanol pool fire. Detailed chemical kinetics are accounted for through TGLDM tables with the inclusion of the effect of radiation heat loss. The radiation treatment accounts for absorption by solving the RTE using the finite volume discrete ordinate method and the WSGG model for estimating the gas absorption coefficients. Soot is modeled in two ways based on the LSP concept. The first model calculates the laminar soot formation and oxidation rates then provides a correction for turbulent effects. The second calculates soot reaction rates in conditional space based on the analytical functions and conditional temperature then integrates the conditional profiles with the FDF to obtain filtered rates. Three cases are investigated. The first case does not include soot modelling, while the other two account for soot through the two described soot models. The predicted flame height and radiative fractions are in agreement with what is reported experimentally. The time-averaged temperature predictions agree with the experiments as well. There is an overprediction in the plume region, away from the peak temperature that is smaller when the first soot model is applied. Species mole fractions are in general agreement with the measurements with some discrepancies observed in the products downstream of the peak which can be explained in part by the uncertainty in the measurements. The soot mass fraction peak is underpredicted by 29% using the first soot model. However, with the second soot model the values are notably underpredicted and the peak soot location

is closer to the fire base in comparison to what is seen in the experiments. Although soot model 1 heavily relies on many empirical constants and relations, and includes simplified expressions based on EDC/partially stirred reactor concept, the current soot predictions are reasonable in the context of soot/fire simulations where large experimental uncertainties are found. In contrast, soot model 2 has not performed as well as soot model 1 for the present case. Soot model 2 includes a mixture fraction dependence for soot formation and oxidation through presumed functions making it more suitable for CSE formulation and explicit inclusion of turbulence soot interactions. As pointed out by Lautenberger et al. [15], the larger discrepancies in soot mass fraction predicted by model 2 may be due to the lack of soot formation dependence on surface area, important in lightly sooting fuels such as ethanol, and the functions probably need more adjustment. This is difficult to conduct without additional experimental data

The simulations overpredict the peak radiative flux away from the pool in the radial direction. However, the results become closer to the measurements moving downstream. The radiative flux in the downward direction is overpredicted as well near the burner wall and becomes in agreement with the measurements moving radially. The behaviour of the different heat flux profiles is similar to that of a previous study [43] simulating methanol pool fires of the same scale. The current model does not account for fuel radiation in the calculation of the absorption coefficient which is a possible contributing factor for the discrepancies shown.

The present work with simple soot models as part of a larger LES framework including detailed turbulent combustion and radiation models is a very first step towards incorporating more detailed soot models for pool fires exhibiting higher soot levels. Additional experimental fire data need to be examined for further validation.

7.2 Summary of accomplishments

The main outcomes of the current dissertation can be summarized as

- Previously, CSE approach has been considered in modeling jet flames at different situations. However, the current study extends CSE approach to investigations of turbulent buoyant diffusion flames such as fires for the first time.
- Coupling of CSE approach for the first time with the LES FireFOAM solver. As a first step, the UMD methane line fire is tested with different radiation implementations all with the optically thin approximation. The results are in good agreement

with experimental measurements and are improved with the inclusion of TRI in the calculations.

- Inclusion of radiation absorption with CSE for the first time. All of the previous CSE simulations have relied on the optically thin approximation and the RADCAL approach for estimating coefficients. In the current study, radiation absorption is accounted for by solving the RTE along with applying WSGG for calculation of the absorption coefficients. The TRI are included as well by calculating the absorption coefficients and the emission term in conditional space then integrating them with the FDF.

- The new framework is used to investigate medium and large scale methanol pool fires to be the first CSE study on pool fires. The temperature results are improved with including RTE solution. A fine angular mesh is shown to be important away from the pool fire, while a coarse one is adequate to estimate the near flame region radiative fluxes.

- Coupling CSE for the first time with two of the most commonly used soot models in fire simulations that are based on the LSP concept. The approach is used for the investigation of the medium scale ethanol pool fire which has not been investigated previously.

7.3 Future work

In the current study, methane, methanol and ethanol fires are considered. However, more complex fuels, that are found in engineering applications and subject to fire incidents such as kerosene and jet A, are important to study as well. For this, the current tabulation technique may not be adequate, and other tabulation techniques may be implemented along with CSE to simulate such complex fuels. The performance of chemistry tabulations would be enhanced by inclusion of the recent advances in machine learning and neural networks.

Some numerical parameters have been selected based on choices from previously published studies. The effects associated with varying those parameters on the results have not been investigated or at least are not studied well enough. It is worth considering the effect of variation of those parameters in the future. These parameters include the Courant number, the use of dynamic Smagorinsky sgs turbulence model, the ensembles shape as well as distribution and the outer geometric dimensions of the computational domains.

Throughout the current study, the implemented form of CSE relies on a single conditioning variable. With high levels of extinction, double conditioning variables or DCSE will need to be examined, and in particular the joint PDF closure will have to be investigated in the context of turbulent buoyant flames.

The effects of water suppression in fires can be included through inclusion of spray modeling in the current framework. This is an important step in modeling real world fire incidents.

Other radiation modeling approaches will be considered, including more detailed description of the absorption coefficient and falling under the class of narrow band and wide band models.

In regard to soot modeling, more detailed models that account for soot formation dependence on surface area as well as the inclusion of PAH-based soot inception will be required for more accurate predictions. This is important in cases of fuels with high levels of soot production such as acetone and heptane.

Introducing pyrolysis and flame spread modeling to the current framework to extend the applications from pool fires to other situations involving complex combusting materials.

Letters of Copyright Permission

- The letter of permission for Figure 1.1:

  This Agreement between Ahmed Abdalhamid (”You”) and Elsevier (”Elsevier”) consists of your license details and the terms and conditions provided by Elsevier and Copyright Clearance Center.
  License Number 5926000315578
  License date Dec 11, 2024
  Licensed Content Publisher Elsevier
  Licensed Content Publication Fire Safety Journal
  Licensed Content Title A review of physics and correlations of pool fire behaviour in wind and future challenges
  Licensed Content Author Longhua Hu
  Licensed Content Date Jul 1, 2017
  Licensed Content Volume 91
  Licensed Content Issue n/a
  Licensed Content Pages 15
  Start Page 41
  End Page 55
  Type of Use reuse in a thesis/dissertation
  Portion figures/tables/illustrations
  Number of figures/tables/illustrations 1
  Format both print and electronic
  Are you the author of this Elsevier article? No
  Will you be translating? No
  Title of new work Development of Conditional Source-term Estimation (CSE) Framework for Turbulent Buoyant Diffusion Flames
  Institution name University of Waterloo
  Expected presentation date Dec 2024

Portions Fig. 1
The Requesting Person / Organization to Appear on the License Ahmed Abdalhamid
Requestor Location Mr. Ahmed Abdalhamid –
Publisher Tax ID GB 494 6272 12
Total 0.00 USD

- The letter of permission for Figure 4.5:

  This Agreement between Ahmed Abdalhamid ("You") and Elsevier ("Elsevier") consists of your license details and the terms and conditions provided by Elsevier and Copyright Clearance Center.
  License Number 5926000755007
  License date Dec 11, 2024
  Licensed Content Publisher Elsevier
  Licensed Content Publication Fire Safety Journal
  Licensed Content Title Large eddy simulation of flame extinction in a turbulent line fire exposed to air-nitrogen co-flow
  Licensed Content Author S. Vilfayeau,J.P. White,P.B. Sunderland,A.W. Marshall,A. Trouvé
  Licensed Content Date Nov 1, 2016
  Licensed Content Volume 86
  Licensed Content Issue n/a
  Licensed Content Pages 16
  Start Page 16
  End Page 31
  Type of Use reuse in a thesis/dissertation
  Portion figures/tables/illustrations
  Number of figures/tables/illustrations 1
  Format both print and electronic
  Are you the author of this Elsevier article? No
  Will you be translating? No
  Title of new work Development of Conditional Source-term Estimation (CSE) Framework for Turbulent Buoyant Diffusion Flames
  Institution name University of Waterloo
  Expected presentation date Dec 2024
  Portions Fig. 4
  The Requesting Person / Organization to Appear on the License Ahmed Abdalhamid

Requestor Location Mr. Ahmed Abdalhamid –
Publisher Tax ID GB 494 6272 12
Total 0.00 USD

- The letter of permission for Figures 5.4 and 6.3:

  This Agreement between Ahmed Abdalhamid ("You") and Elsevier ("Elsevier") consists of your license details and the terms and conditions provided by Elsevier and Copyright Clearance Center.
  License Number 5926001010848
  License date Dec 11, 2024
  Licensed Content Publisher Elsevier
  Licensed Content Publication Fire Safety Journal
  Licensed Content Title Energy balance in medium-scale methanol, ethanol, and acetone pool fires
  Licensed Content Author Sung Chan Kim,Ki Yong Lee,Anthony Hamins
  Licensed Content Date Jul 1, 2019
  Licensed Content Volume 107
  Licensed Content Issue n/a
  Licensed Content Pages 10
  Start Page 44
  End Page 53
  Type of Use reuse in a thesis/dissertation
  Portion figures/tables/illustrations
  Number of figures/tables/illustrations 1
  Format both print and electronic
  Are you the author of this Elsevier article? No
  Will you be translating? No
  Title of new work Development of Conditional Source-term Estimation (CSE) Framework for Turbulent Buoyant Diffusion Flames
  Institution name University of Waterloo
  Expected presentation date Dec 2024
  Portions Fig. 4
  The Requesting Person / Organization to Appear on the License Ahmed Abdalhamid
  Requestor Location Mr. Ahmed Abdalhamid –
  Publisher Tax ID GB 494 6272 12
  Total 0.00 USD

- The letter of permission for Figures 5.15:

  This Agreement between Ahmed Abdalhamid ("You") and Elsevier ("Elsevier") consists of your license details and the terms and conditions provided by Elsevier and Copyright Clearance Center.
  License Number 5926090224294
  License date Dec 11, 2024
  Licensed Content Publisher Elsevier
  Licensed Content Publication Fire Safety Journal
  Licensed Content Title The characteristics of a 1 m methanol pool fire
  Licensed Content Author Kunhyuk Sung,Jian Chen,Matthew Bundy,Anthony Hamins
  Licensed Content Date Mar 1, 2021
  Licensed Content Volume 120
  Licensed Content Issue n/a
  Licensed Content Pages 1
  Start Page 103121
  End Page 0
  Type of Use reuse in a thesis/dissertation
  Portion figures/tables/illustrations
  Number of figures/tables/illustrations 1
  Format both print and electronic
  Are you the author of this Elsevier article? No
  Will you be translating? No
  Title of new work Development of Conditional Source-term Estimation (CSE) Framework for Turbulent Buoyant Diffusion Flames
  Institution name University of Waterloo
  Expected presentation date Dec 2024
  Portions Fig. 4
  The Requesting Person / Organization to Appear on the License Ahmed Abdalhamid
  Requestor Location Mr. Ahmed Abdalhamid –
  Publisher Tax ID GB 494 6272 12
  Total 0.00 USD

References

[1] L. Hu, A review of physics and correlations of pool fire behaviour in wind and future challenges, Fire Saf. J. 91 (2017) 41–55.

[2] A. Hussien, C. Devaud, Simulations of turbulent acetone spray flames using the conditional source term estimation (CSE) approach, Combust. Theor. Model. 25 (2) (2021) 269–292.

[3] M. F. Modest, Radiative Heat Transfer (3rd Edition), Elsevier, 2013.

[4] J. White, E. Link, A. Trouvé, P. Sunderland, A. Marshall, J. Sheffel, M. Corn, M. Colket, M. Chaos, H.-Z. Yu, Radiative emissions measurements from a buoyant, turbulent line flame under oxidizer-dilution quenching conditions, Fire Saf. J. 76 (2015) 74–84.

[5] S. Vilfayeau, J. White, P. Sunderland, A. Marshall, A. Trouvé, Large eddy simulation of flame extinction in a turbulent line fire exposed to air-nitrogen co-flow, Fire Saf. J. 86 (2016) 16–31.

[6] A. Marchand, S. Verma, R. Xu, J. White, A. Marshall, T. Rogaume, F. Richard, J. Luche, A. Trouvé, et al., Simulations of a turbulent line fire with a steady flamelet combustion model coupled with models for non-local and local gas radiation effects, Fire Saf. J. 106 (2019) 105–113.

[7] R. Xu, A. Marchand, S. Verma, T. Rogaume, F. Richard, J. Luche, A. Trouvé, et al., Simulations of the coupling between combustion and radiation in a turbulent line fire using an unsteady flamelet model, Fire Saf. J. 120 (2021) 103101.

[8] B. Kruljevic, I. Stankovic, B. Merci, Large eddy simulations of the UMD line burner with the conditional moment closure method, Fire Saf. J. 116 (2020) 103206.

[9] S. C. Kim, K. Y. Lee, A. Hamins, Energy balance in medium-scale methanol, ethanol, and acetone pool fires, Fire Saf. J. 107 (2019) 44–53.

[10] E. Weckman, A. Strong, Experimental investigation of the turbulence structure of medium-scale methanol pool fires, Combust. Flame 105 (3) (1996) 245–266.

[11] R. Falkenstein-Smith, K. Sung, J. Chen, A. Hamins, Chemical structure of medium-scale liquid pool fires, Fire Saf. J. 120 (2021) 103099.

[12] A. Hamins, S. Fischer, T. Kashiwagi, M. Klassen, J. Gore, Heat feedback to the fuel surface in pool fires, Combust. Sci. Technol. 97 (1-3) (1994) 37–62.

[13] K. Sung, J. Chen, M. Bundy, A. Hamins, The characteristics of a 1 m methanol pool fire, Fire Saf. J. 120 (2021) 103121.

[14] M. Klassen, J. Gore, Structure and radiation properties of pool fires: Final report, NIST GCR (1994) 94–651.

[15] C. W. Lautenberger, J. L. de Ris, N. A. Dembsey, J. R. Barnett, H. R. Baum, A simplified model for soot formation and oxidation in cfd simulation of non-premixed hydrocarbon flames, Fire Saf. J. 40 (2) (2005) 141–176.

[16] J. X. Wen, Fire modelling: The success, the challenges, and the dilemma from a modeller's perspective, Fire Saf. J. 144 (2024) 104087.

[17] R. D. Peacock, K. B. McGrattan, G. P. Forney, P. A. Reneke, et al., CFAST–Consolidated Model of Fire Growth and Smoke Transport (Version 7) Volume 1: Technical Reference Guide (2015).

[18] A. Trouvé, Y. Wang, Large eddy simulation of compartment fires, Int. J. Comut. Fluid Dyn. 24 (10) (2010) 449–466.

[19] A. Trouvé, CFD modeling of large-scale pool fires, Fire Saf. Sci. 9 (2008).

[20] M. M. Ahmed, A. Trouve, Large eddy simulation of the unstable flame structure and gas-to-liquid thermal feedback in a medium-scale methanol pool fire, Combust. Flame 225 (2021) 237–254.

[21] P. Chatterjee, Y. Wang, K. V. Meredith, S. B. Dorofeev, Application of a subgrid soot-radiation model in the numerical simulation of a heptane pool fire, Proc. Combust. Inst. 35 (3) (2015) 2573–2580.

[22] D. Burot, Transported probability density function for the numerical simulation of flames characteristic of fire, Ph.D. thesis, Aix-Marseille (2017).

[23] S. B. Pope, S. B. Pope, Turbulent flows, Cambridge university press, 2000.

[24] K. McGrattan, R. McDermott, C. Weinschenk, G. Forney, Fire dynamics simulator, technical reference guide, sixth edition (4-November- 2013). doi:https://doi.org/10.6028/NIST.sp.1018.

[25] OpenFOAM, Openfoam-7/applications/solvers/combustion/firefoam at master · openfoam/openfoam-7.
URL https://github.com/OpenFOAM/OpenFOAM-7/tree/master/applications/solvers/combustion/fireFoam

[26] G. Maragkos, B. Merci, Large eddy simulations of CH_4 fire plumes, Flow Turbul. Combust. 99 (1) (2017) 239–278.

[27] D. B. Spalding, Development of the eddy-break-up model of turbulent combustion, in: Symp. (Int.) Combust., Vol. 16, Elsevier, 1977, pp. 1657–1663.

[28] B. F. Magnussen, B. H. Hjertager, On mathematical modeling of turbulent combustion with special emphasis on soot formation and combustion, in: Symp. (Int.) Combust., Vol. 16, Elsevier, 1977, pp. 719–729.

[29] B. F. Magnussen, The eddy dissipation concept: A bridge between science and technology, in: ECCOMAS thematic conference on computational combustion, Vol. 21, Libson, Portugal, 2005, p. 24.

[30] N. Peters, Laminar diffusion flamelet models in non-premixed turbulent combustion, Prog. Energy Combust. Sci. 10 (3) (1984) 319–339.

[31] S. K. Liew, K. Bray, J. Moss, A flamelet model of turbulent non-premixed combustion, Combust. Sci. Technol. 27 (1-2) (1981) 69–73.

[32] A. Y. Klimenko, R. W. Bilger, Conditional moment closure for turbulent combustion, Prog. Energy Combust. Sci. 25 (6) (1999) 595–687.

[33] H. Steiner, W. Bushe, Large eddy simulation of a turbulent reacting jet with conditional source-term estimation, Phys. Fluids 13 (3) (2001) 754–769.

[34] F. Nmira, L. Ma, J.-L. Consalvi, Influence of gas radiative property models on Large Eddy Simulation of 1 m methanol pool fires, Combust. Flame 221 (2020) 352–363.

[35] M. M. Salehi, C. Devaud, W. K. Bushe, Advances and challenges of the conditional source-term estimation model for turbulent reacting flows, Prog. Energy Combust. Sci. 104 (2024) 101172.

[36] D. Dovizio, M. M. Salehi, C. B. Devaud, RANS simulation of a turbulent premixed bluff body flame using conditional source-term estimation, Combust. Theor. Model. 17 (5) (2013) 935–959.

[37] J. W. Labahn, C. B. Devaud, Investigation of conditional source-term estimation applied to a non-premixed turbulent flame, Combust. Theor. Model. 17 (5) (2013) 960–982.

[38] J. W. Labahn, I. Stanković, C. B. Devaud, B. Merci, Comparative study between Conditional Moment Closure (CMC) and Conditional Source-term Estimation (CSE) applied to piloted jet flames, Combust. Flame 181 (2017) 172–187.

[39] M. Mortada, C. Devaud, Large eddy simulation of lifted turbulent flame in cold air using doubly conditional source-term estimation, Combust. Flame 208 (2019) 420–435.

[40] M. Klassen, J. Gore, Structure and radiation properties of pool fires: Final report, National Institute of Standards and Technology Report NIST-GCR-94-651, Gaithersburg, MD (1992) 1–153.

[41] G. Maragkos, B. Merci, Large eddy simulations of flame extinction in a turbulent line burner, Fire Saf. J. 105 (2019) 216–226.

[42] I. Sikic, S. Dembele, J. Wen, Non-grey radiative heat transfer modelling in les-cfd simulated methanol pool fires, J. Quant. Spectrosc. Radiat. Transf. 234 (2019) 78–89.

[43] L. Ma, F. Nmira, J.-L. Consalvi, Large eddy simulation of medium-scale methanol pool fires-effects of pool boundary conditions, Combust. Flame 222 (2020) 336–354.

[44] H. Wang, Formation of nascent soot and other condensed-phase materials in flames, Proc. Combust. Inst. 33 (1) (2011) 41–67.

[45] P. K. Raj, Large hydrocarbon fuel pool fires: Physical characteristics and thermal emission variations with height, J. Hazard. Mater. 140 (1-2) (2007) 280–292.

[46] T. Steinhaus, S. Welch, R. O. Carvel, J. L. Torero, Large-scale pool fires, Therm. Sci. 11 (2) (2007) 101–118.

[47] Z. Yin, S. Liu, D. Tan, Z. Zhang, Z. Wang, B. Wang, A review of the development and application of soot modelling for modern diesel engines and the soot modelling for different fuels, Process Saf. Environ. Prot. (2023).

[48] M. J. Thomson, Modeling soot formation in flames and reactors: Recent progress and current challenges, Proc. Combust. Inst. 39 (1) (2023) 805–823.

[49] T. Beji, J. Zhang, W. Yao, M. Delichatsios, A novel soot model for fires: validation in a laminar non-premixed flame, Combust. Flame 158 (2) (2011) 281–290.

[50] M. Salehi, W. Bushe, K. Daun, Application of the conditional source-term estimation model for turbulence–chemistry interactions in a premixed flame, Combust. Theor. Model. 16 (2) (2012) 301–320.

[51] M. Wang, J. Huang, W. Bushe, Simulation of a turbulent non-premixed flame using conditional source-term estimation with trajectory generated low-dimensional manifold, Proc. Combust. Inst. 31 (2) (2007) 1701–1709.

[52] A. M. Abdalhamid, C. Devaud, Large eddy simulations of a buoyant turbulent line flame using conditional source-term estimation (CSE), Combust. Theor. Model. 28 (2024) 344–365.

[53] B. Merci, T. Beji, Fluid mechanics aspects of fire and smoke dynamics in enclosures, CRC press Leiden, 2016.

[54] T. Poinsot, D. Veynante, Theoretical and numerical combustion, RT Edwards, Inc., 2005.

[55] A. J. Favre, Formulation of the statistical equations of turbulent flows with variable density, in: Studies in turbulence, Springer, 1992, pp. 324–341.

[56] B. E. Launder, D. B. Spalding, The numerical computation of turbulent flows, in: Numerical prediction of flow, heat transfer, turbulence and combustion, Elsevier, 1983, pp. 96–116.

[57] F. R. Menter, M. Kuntz, R. Langtry, et al., Ten years of industrial experience with the sst turbulence model, Turbulence, heat and mass transfer 4 (1) (2003) 625–632.

[58] D. C. Wilcox, et al., Turbulence modeling for CFD, Vol. 2, DCW industries La Canada, CA, 1998.

[59] J. Smagorinsky, General circulation experiments with the primitive equations: I. the basic experiment, Mon. Weather Rev. 91 (3) (1963) 99–164.

[60] U. Schumann, Subgrid scale model for finite difference simulations of turbulent flows in plane channels and annuli, J. Comput. Phys. 18 (4) (1975) 376–404.

[61] Z. H. Yan, Large eddy simulations of a turbulent thermal plume, Heat Mass Transf. 43 (6) (2007) 503–514.

[62] D. Spalding, Mixing and chemical reaction in steady confined turbulent flames, in: Symp. (Int.) Combust., Vol. 13, Elsevier, 1971, pp. 649–657.

[63] R. Bilger, Turbulent flows with nonpremixed reactants, in: Turbulent reacting flows, Springer, 1980, pp. 65–113.

[64] C. D. Pierce, P. Moin, A dynamic model for subgrid-scale variance and dissipation rate of a conserved scalar, Phys. Fluids 10 (12) (1998) 3041–3044.

[65] J. Labahn, C. Devaud, Large eddy simulations (LES) including conditional source-term estimation (CSE) applied to two Delft-Jet-in-Hot-Coflow (DJHC) flames, Combust. Flame 164 (2016) 68–84.

[66] N. Peters, Turbulent combustion, Measurement Science and Technology 12 (11) (2001) 2022–2022.

[67] S. Girimaji, Assumed β-pdf model for turbulent mixing: Validation and extension to multiple scalar mixing, Combust. Sci. Technol. 78 (4-6) (1991) 177–196.

[68] B. Cuenot, The flamelet model for non-premixed combustion, in: Turbulent Combustion Modeling: Advances, New Trends and Perspectives, Springer, 2011, pp. 43–61.

[69] R. Bilger, Conditional moment closure for turbulent reacting flow, Phys. Fluids 5 (2) (1993) 436–444.

[70] A. Y. Klimenko, Multicomponent diffusion of various admixtures in turbulent flow, Fluid Dyn. 25 (3) (1990) 327–334.

[71] R. Bilger, Future progress in turbulent combustion research, Prog. Energy Combust. Sci. 26 (4-6) (2000) 367–380.

[72] S. H. Kim, K. Y. Huh, R. A. Fraser, Numerical prediction of the autoignition delay in a diesel-like environment by the conditional moment closure model, SAE transactions (2000) 50–56.

[73] S. H. Kim, K. Y. Huh, L. Tao, Application of the elliptic conditional moment closure model to a two-dimensional nonpremixed methanol bluff-body flame, Combust. Flame 120 (1-2) (2000) 75–90.

[74] C. Dopazo, E. E. O'Brien, An approach to the autoignition of a turbulent mixture, Acta Astronaut. 1 (9-10) (1974) 1239–1266.

[75] C. Dopazo, E. E. OBRIEN, Functional formulation of nonisothermal turbulent reactive flows, Phys. Fluids 17 (11) (1974) 1968.

[76] S. B. Pope, PDF methods for turbulent reactive flows, Prog. Energy Combust. Sci. 11 (2) (1985) 119–192.

[77] D. C. Haworth, Progress in probability density function methods for turbulent reacting flows, Prog. Energy Combust. Sci. 36 (2) (2010) 168–259.

[78] A. Y. Klimenko, S. B. Pope, The modeling of turbulent reactive flows based on multiple mapping conditioning, Phys. Fluids 15 (7) (2003) 1907–1925.

[79] M. Cleary, A. Kronenburg, Multiple mapping conditioning for extinction and reignition in turbulent diffusion flames, Proc. Combust. Inst. 31 (1) (2007) 1497–1505.

[80] K. Vogiatzaki, A. Kronenburg, M. Cleary, J. Kent, Multiple mapping conditioning of turbulent jet diffusion flames, Proc. Combust. Inst. 32 (2) (2009) 1679–1685.

[81] A. P. Wandel, R. P. Lindstedt, Hybrid binomial langevin-multiple mapping conditioning modeling of a reacting mixing layer, Phys. Fluids 21 (1) (2009).

[82] M. Cleary, A. Klimenko, Multiple mapping conditioning: A new modelling framework for turbulent combustion, in: Turbulent Combustion Modeling: Advances, New Trends and Perspectives, Springer, 2011, pp. 143–173.

[83] J. Huang, W. Bushe, Simulation of transient turbulent methane jet ignition and combustion under engine-relevant conditions using conditional source-term estimation with detailed chemistry, Combust. Theor. Model. 11 (6) (2007) 977–1008.

[84] S. Lee, C. Devaud, Application of conditional source-term estimation to two turbulent non-premixed methanol flames, Combust. Theor. Model. 20 (5) (2016) 765–797.

[85] J. W. Labahn, C. Devaud, Species and temperature predictions in a semi-industrial mild furnace using a non-adiabatic conditional source-term estimation formulation, Combust. Theor. Model. 21 (3) (2017) 466–486.

[86] B. Jin, R. Grout, W. Bushe, Conditional source-term estimation as a method for chemical closure in premixed turbulent reacting flow, Flow Turbul. Combust. 81 (2008) 563–582.

[87] A. Hussien, C. Devaud, Simulations of partially premixed turbulent ethanol spray flames using doubly conditional source term estimation (DCSE), Combust. Flame 239 (2022) 111651.

[88] S. M. Ashrafizadeh, C. Devaud, Investigation of conditional source-term estimation coupled with a semi-empirical model for soot predictions in two turbulent flames, Combust. Theor. Model. 26 (5) (2022) 856–878.

[89] M. Fairweather, R. Woolley, First-order conditional moment closure modeling of turbulent, nonpremixed methane flames, Combust. Flame 138 (1-2) (2004) 3–19.

[90] G. P. Smith, Gri-mech 3.0, http://www. me. berkley. edu/gri_mech/ (1999).

[91] A. Hussien, C. Devaud, LES study of turbulent ethanol spray flames using CSE coupled with non-adiabatic chemistry tables, Proc. Combust. Inst. 39 (2) (2023) 2379–2388.

[92] S. Pope, U. Maas, Simplifying chemical kinetics: Trajectory-generated low-dimensional manifolds, Mechanical and Aerospace Engineering Report, Ithaca, NY, Report No. FDA (1993) 93–11.

[93] J. W. Labahn, C. B. Devaud, T. A. Sipkens, K. J. Daun, Inverse analysis and regularisation in conditional source-term estimation modelling, Combust. Theor. Model. 18 (3) (2014) 474–499.

[94] J. Van Oijen, L. De Goey, Modelling of premixed laminar flames using flamelet-generated manifolds, Combust. Sci. Technol. 161 (1) (2000) 113–137.

[95] K. Han, K. Y. Huh, Conditional moment closure method with tabulated chemistry in adiabatic turbulent nonpremixed jet flames, Combust. Flame 234 (2021) 111652.

[96] X. H. Fang, R. Ismail, K. Bushe, M. Davy, Simulation of ecn diesel spray a using conditional source-term estimation, Combust. Theor. Model. 24 (4) (2020) 725–760.

[97] A. H. Mahdipour, C. Devaud, Different conditional source-term estimation formulations applied to turbulent nonpremixed jet flames with varying levels of extinction, Combust. Th. Model. 28 (3) (2024) 237–261.

[98] R. Grout, W. K. Bushe, C. Blair, Predicting the ignition delay of turbulent methane jets using conditional source-term estimation, Combust. Theor. Model. 11 (6) (2007) 1009–1028.

[99] P. C. Hansen, Numerical tools for analysis and solution of fredholm integral equations of the first kind, Inverse problems 8 (6) (1992) 849.

[100] R. A. Willoughby, Solutions of ill-posed problems (AN Tikhonov and VY Arsenin), SIAM Review 21 (2) (1979) 266.

[101] P. C. Hansen, The truncatedSVD as a method for regularization, BIT Numerical Mathematics 27 (4) (1987) 534–553.

[102] C. Bowman, R. Hanson, D. Davidson, W. Gardiner Jr, V. Lissianski, G. Smith, D. Golden, M. Frenklach, M. Goldenberg, GRI-Mech 2.11, 1995, http://www.me.berkeley.edu/gri_mech/ (1995).

[103] G. P. Smith, D. M. Golden, M. Frenklach, N. W. Moriarty, B. Eiteneer, M. Goldenberg, C. T. Bowman, R. K. Hanson, S. Song, W. C. Gardiner, Jr., V. V. Lissianski, Z. Qin, GRI-Mech 3.0, http://www.me.berkeley.edu/gri_mech/.

[104] J. Huang, Natural gas combustion under engine-relevant conditions, Ph.D. thesis, University of British Columbia (2006).

[105] U. Maas, S. B. Pope, Simplifying chemical kinetics: intrinsic low-dimensional manifolds in composition space, Combust. Flame 88 (3-4) (1992) 239–264.

[106] J. Nafe, U. Maas, Modeling of no formation based on ildm reduced chemistry, Proc. Combust. Inst. 29 (1) (2002) 1379–1385.

[107] R. J. Renka, Algorithm 751: Tripack: a constrained two-dimensional delaunay triangulation package, ACM Trans. Math. Softw. 22 (1) (1996) 1–8.

[108] H. Hottel, E. Cohen, Radiant heat exchange in a gas-filled enclosure: Allowance for nonuniformity of gas temperature, AIChE Journal 4 (1) (1958) 3–14.

[109] F. Lockwood, N. Shah, A new radiation solution method for incorporation in general combustion prediction procedures, in: Symp. (Int.) Combust., Vol. 18, Elsevier, 1981, pp. 1405–1414.

[110] M. F. Modest, D. C. Haworth, Radiative heat transfer in turbulent combustion systems: theory and applications, Springer, 2016.

[111] G. N. Schenker, B. Keller, Line-by-line calculations of the absorption of infrared radiation by water vapor in a box-shaped enclosure filled with humid air, Int. J. Heat Mass Transf. 38 (17) (1995) 3127–3134.

[112] J. Hartmann, R. L. Di Leon, J. Taine, Line-by-line and narrow-band statistical model calculations for H_2O, J. Quant. Spectrosc. Radiat. Transf. 32 (2) (1984) 119–127.

[113] H. Zhang, M. F. Modest, Multi-group full-spectrum k-distribution database for water vapor mixtures in radiative transfer calculations, in: Heat Transfer Summer Conference, Vol. 36932, 2003, pp. 797–806.

[114] F. André, R. Vaillon, The k-moment method for modeling the blackbody weighted transmission function for narrow and wide band radiative properties of gases, J. Quant. Spectrosc. Radiat. Transf. 108 (1) (2007) 1–16.

[115] H. Hottel, A. Sarofim, Radiative Transfer, McGraw-Hill, New York, 1967.

[116] M. Modest, The weighted-sum-of-gray-gases model for arbitrary solution methods in radiative transfer, J. Heat Tran. 113 (1991) 650–656.

[117] L. S. Rothman, I. E. Gordon, A. Barbe, D. C. Benner, P. F. Bernath, M. Birk, V. Boudon, L. R. Brown, A. Campargue, J.-P. Champion, et al., The HITRAN 2008 molecular spectroscopic database, J. Quant. Spectrosc. Radiat. Transf. 110 (9-10) (2009) 533–572.

[118] L. S. Rothman, I. Gordon, R. Barber, H. Dothe, R. R. Gamache, A. Goldman, V. Perevalov, S. Tashkun, J. Tennyson, HITEMP, the high-temperature molecular spectroscopic database, J. Quant. Spectrosc. Radiat. Transf. 111 (15) (2010) 2139–2150.

[119] M. F. Modest, H. Zhang, The full-spectrum correlated-k distribution and its relationship to the weighted-sum-of-gray-gases method, ASME-Publications-Htd 366 (2000) 75–84.

[120] L. J. Dorigon, G. Duciak, R. Brittes, F. Cassol, M. Galarca, F. H. Franca, WSGG correlations based on HITEMP2010 for computation of thermal radiation in non-isothermal, non-homogeneous H_2O/CO_2 mixtures, Int. J. Heat Mass Transf. 64 (2013) 863–873.

[121] F. R. Coelho, F. H. França, WSGG correlations based on HITEMP2010 for gas mixtures of H_2O and CO_2 in high total pressure conditions, Int. J. Heat Mass Transf. 127 (2018) 105–114.

[122] Z. Chen, J. Wen, B. Xu, S. Dembele, Large eddy simulation of a medium-scale methanol pool fire using the extended eddy dissipation concept, Int. J. Heat Mass Transf. 70 (2014) 389–408.

[123] B. Kruljevic, Fundamental study in applications of the conditional moment closure method to fire-related flows, Ph.D. thesis, Ghent University (2021).

[124] G. Maragkos, T. Beji, B. Merci, Advances in modelling in CFD simulations of turbulent gaseous pool fires, Combust. Flame 181 (2017) 22–38.

[125] R. Barlow, A. Karpetis, J. Frank, J.-Y. Chen, Scalar profiles and NO formation in laminar opposed-flow partially premixed methane/air flames, Combust. Flame 127 (3) (2001) 2102–2118.

[126] W. L. Grosshandler, A narrow-band model for radiation calculations in a combustion, Environment NIST Tech (1993).

[127] T. Workshop, Radiation models, https://tnfworkshop.org/radiation/.

[128] H. Bockhorn, Soot formation in combustion: mechanisms and models, Vol. 59, Springer Series in Chemical Physics, 1994.

[129] F. Xu, A. El-Leathy, C. Kim, G. Faeth, Soot surface oxidation in hydrocarbon/air diffusion flames at atmospheric pressure, Combust. Flame 132 (1-2) (2003) 43–57.

[130] B. S. Haynes, H. G. Wagner, Soot formation, Prog. Energy Combust. Sci. 7 (4) (1981) 229–273.

[131] M. Frenklach, H. Wang, Detailed mechanism and modeling of soot particle formation, in: Soot formation in combustion: mechanisms and models, Springer, 1994, pp. 165–192.

[132] M. Frenklach, Reaction mechanism of soot formation in flames, Phys. Chem. Chem. Phys. 4 (11) (2002) 2028–2037.

[133] H. Omidvarborna, A. Kumar, D.-S. Kim, Recent studies on soot modeling for diesel combustion, Renew. Sustain. Energy Rev. 48 (2015) 635–647.

[134] H. Wang, M. Frenklach, A detailed kinetic modeling study of aromatics formation in laminar premixed acetylene and ethylene flames, Combust. Flame 110 (1-2) (1997) 173–221.

[135] J. Martin, M. Salamanca, M. Kraft, Soot inception: Carbonaceous nanoparticle formation in flames, Prog. Energy Combust. Sci. 88 (2022) 100956.

[136] J. Kent, D. Honnery, A soot formation rate map for a laminar ethylene diffusion flame, Combust. Flame 79 (3-4) (1990) 287–298.

[137] J. Moss, C. Stewart, Flamelet-based smoke properties for the field modelling of fires, Fire Saf. J. 30 (1998) 229–250.

[138] F. Eigentler, P. Gerlinger, A detailed PAH and soot model for complex fuels in CFD applications, Flow Turbul. Combust. 109 (2022) 225–251.

[139] K. M. Leung, R. P. Lindstedt, W. P. Jones, A simplified reaction mechanism for soot formation in nonpremixed flames, Combust. Flame 87 (3-4) (1991) 289–305.

[140] F. Nmira, J. Consalvi, R. Demarco, L. Gay, Assessment of semi-empirical soot production models in C1–C3 axisymmetric laminar diffusion flames, Fire Saf. J. 73 (2015) 76–90.

[141] A. Tewarson, Smoke point height and fire properties of materials, US Department of Commerce, National Institute of Standards and Technology, NIST GCR 88-555, Gaithersburg, MD, 1988.

[142] G. Markstein, J. De Ris, Radiant emission and absorption by laminar ethylene and propylene diffusion flames, in: Symp. (Int.) Combust., Vol. 20, Elsevier, 1985, pp. 1637–1646.

[143] M. Delichatsios, A phenomenological model for smoke-point and soot formation in laminar flames, Combust. Sci. Technol. 100 (1-6) (1994) 283–298.

[144] W. Yao, J. Zhang, A. Nadjai, T. Beji, M. A. Delichatsios, A global soot model developed for fires: Validation in laminar flames and application in turbulent pool fires, Fire Saf. J. 46 (7) (2011) 371–387.

[145] Y. Niu, Y. Zhang, X. Chen, D. Zhou, Application of the global soot model based on smoke point in simulation of multiple laminar diffusion flames, Combust. Sci. Technol. 190 (6) (2018) 1060–1074.

[146] Z. Chen, J. Wen, B. Xu, S. Dembele, Extension of the eddy dissipation concept and smoke point soot model to the LES frame for fire simulations, Fire Saf. J. 64 (2014) 12–26.

[147] C. Wang, H. Liu, J. X. Wen, An improved PaSR-based soot model for turbulent fires, Appl. Therm. Eng. 129 (2018) 1435–1446.

[148] S. Motaghian, T. Beji, Soot modeling in large eddy simulation of turbulent buoyant flames using the laminar smoke point and the eddy dissipation concept, Combust. Sci. Technol. (2023) 1–22.

[149] P. Chatterjee, D. Zeng, Y. Wang, Numerical modeling of soot radiation in optically-thin, buoyant diffusion flames at varying oxygen concentrations, Proc. Combust. Inst. 38 (3) (2021) 4987–4994.

[150] P. Chatterjee, Y. Wang, Numerical simulations of soot-radiation from buoyant turbulent wall-bounded diffusion flames, Fire Saf. J. 120 (2021) 103105.

[151] A. Brown, M. Bruns, M. Gollner, J. Hewson, G. Maragkos, A. Marshall, R. McDermott, B. Merci, T. Rogaume, S. Stoliarov, J. Torero, A. Trouvé, Y. Wang, E. Weckman, Proceedings of the first workshop organized by the IAFSS Working Group on Measurement and Computation of Fire Phenomena (MaCFP), Fire Saf. J. 101 (2018) 1–17.

[152] J. P. White, Measurement and simulation of suppression effects in a buoyant turbulent line fire, Ph.D. thesis, University of Maryland, College Park (2016).

[153] J. White, E. Link, A. Trouvé, P. Sunderland, A. Marshall, A general calorimetry framework for measurement of combustion efficiency in a suppressed turbulent line fire, Fire Saf. J. 92 (2017) 164–176.

[154] J. White, S. Vilfayeau, A. Marshall, A. Trouve, R. McDermott, Modeling flame extinction and reignition in large eddy simulations with fast chemistry, Fire Saf. J. 90 (2017) 72–85.

[155] L. Ma, F. Nmira, J.-L. Consalvi, Modelling extinction/re-ignition processes in fire plumes under oxygen-diluted conditions using flamelet tabulation approaches, Combust. Theor. Model. 26 (2022) 613–636.

[156] C. Greenshields, OpenFOAM v8 User Guide: 5.2 Boundaries (Jul 2020).
URL https://cfd.direct/openfoam/user-guide/v8-boundaries/#x25-1770005.2

[157] P. J. Coelho, Numerical simulation of the interaction between turbulence and radiation in reactive flows, Prog. Energy Combust. Sci. 33 (4) (2007) 311–383.

[158] A. Hamins, A. Lock, The Structure of a Moderate-Scale Methanol Pool Fire, TN-1928, NIST, 2016.

[159] W. Bushe, Spatial gradients of conditional averages in turbulent flames, Combust. Flame 192 (2018) 314–339.

[160] B. Merci, J. Li, G. Maragkos, On the importance of the heat release rate in numerical simulations of fires in mechanically ventilated air-tight enclosures, Proc. Combust. Inst. 39 (3) (2023) 3647–3672.

[161] J. Consalvi, F. Nmira, Absorption turbulence-radiation interactions in sooting turbulent jet flames, J. Quant. Spectrosc. Radiat. Transf. 201 (2017) 1–9.

[162] Y. Chen, J. Fang, X. Zhang, Y. Miao, Y. Lin, R. Tu, L. Hu, Pool fire dynamics: Principles, models and recent advances, Prog. Energy Combust. Sci. 95 (2023) 101070.

[163] G. Maragkos, P. Rauwoens, Y. Wang, B. Merci, Large eddy simulations of the flow in the near-field region of a turbulent buoyant helium plume, Flow Turbul. Combust. 90 (2013) 511–543.

[164] B. F. Magnussen, B. H. Hjertager, On mathematical modeling of turbulent combustion with special emphasis on soot formation and combustion, in: Int. Symp. Combust., Vol. 16, Elsevier, 1977, pp. 719–729.

[165] G. Maragkos, B. Merci, Influence of radiation modelling in under-resolved fds freeburn simulations, Int. J. Heat Fluid Flow (2024) 109437.

[166] S. B. Pope, Pdf methods for turbulent reactive flows, Prog. Energy Combust. Sci. 11 (2) (1985) 119–192.

[167] M. Jangi, B. Z. Dlugogorski, On wall fire interaction in a small pool fire: A large-eddy simulation study, Fire Saf. J. 92 (2017) 199–209.

[168] N. Peters, Laminar diffusion flamelet models in non-premixed turbulent combustion, Prog. Energy Combust. Sci. 10 (3) (1984) 319–339.

[169] W. Han, J. Lin, G. H. Yeoh, E. R. Hawkes, Les/pdf modelling of a one-meter diameter methane fire plume, Proc. Combust. Inst. 38 (3) (2021) 4943–4951.

[170] M. Cleary, J. Kent, Modelling of species in hood fires by conditional moment closure, Combust. Flame 143 (4) (2005) 357–368.

[171] W. K. Bushe, H. Steiner, Laminar flamelet decomposition for conditional source-term estimation, Phys. Fluids 15 (2003) 1564–1575.

[172] J.-L. Consalvi, F. Nmira, W. Kong, On the modeling of the filtered radiative transfer equation in large eddy simulations of lab-scale sooting turbulent diffusion flames, J. Quant. Spectrosc. Radiat. Transf. 221 (2018) 51–60.

[173] A. Gupta, D. Haworth, M. Modest, Turbulence-radiation interactions in large-eddy simulations of luminous and nonluminous nonpremixed flames, Proc. Combust. Inst. 34 (1) (2013) 1281–1288.

[174] J.-L. Consalvi, F. Nmira, F. André, Modelling and effects of fuel radiation in methanol pool fires, Fire Saf. J. 140 (2023) 103911.

[175] R. Falkenstein-Smith, R. Falkenstein-Smith, K. Sung, J. Chen, K. Harris, A. Hamins, The structure of medium-scale pool fires, US Department of Commerce, National Institute of Standards and Technology, 2020.

[176] A. Brown, M. Bruns, M. Gollner, J. Hewson, G. Maragkos, A. Marshall, R. McDermott, B. Merci, T. Rogaume, S. Stoliarov, et al., Proceedings of the first workshop organized by the iafss working group on measurement and computation of fire phenomena (MaCFP), Fire Saf. J. 101 (2018) 1–17.

[177] Measurement and Computation of Fire Phenomena Database - 2023 Modeling Guidelines, https://github.com/MaCFP/macfp-db/wiki/MaCFP-2023-Modeling-Guidelines, Accessed: 2023-11-30.

[178] G. Maragkos, T. Beji, B. Merci, Towards predictive simulations of gaseous pool fires, Proc. Combust. Inst. 37 (3) (2019) 3927–3934.

[179] G. Maragkos, B. Merci, On the use of dynamic turbulence modelling in fire applications, Combust. Flame 216 (2020) 9–23.

[180] G. Maragkos, B. Merci, Grid insensitive modelling of convective heat transfer fluxes in CFD simulations of medium-scale pool fires, Fire Saf. J. 120 (2021) 103104.

[181] J. A. Hubbard, M. A. Hansen, J. R. Kirsch, J. C. Hewson, S. P. Domino, Medium-scale methanol pool fire model validation, J. Heat Transf. 144 (6) (2022) 061303.

[182] J. Kirsch, J. Hubbard, Study of radiative heat transfer and flow physics from medium-scale methanol pool fire simulations, Proc. Combust. Inst. 39 (3) (2023) 4013–4020.

[183] Measurement and Computation of Fire Phenomena Database - Waterloo Methanol, https://github.com/MaCFP/macfp-db/tree/master/Liquid_Pool_Fires/Waterloo_Methanol/Experimental_Data, Accessed: 2023-11-30.

[184] Y. Wang, P. Chatterjee, J. L. de Ris, Large eddy simulation of fire plumes, Proc. Combust. Inst. 33 (2) (2011) 2473–2480.

[185] G. Maragkos, P. Rauwoens, B. Merci, Application of fds and firefoam in large eddy simulations of a turbulent buoyant helium plume, Combust. Sci. Technol. 184 (7-8) (2012) 1108–1120.

[186] A. Jatale, P. J. Smith, J. N. Thornock, S. T. Smith, J. P. Spinti, M. Hradisky, Application of a verification, validation and uncertainty quantification framework to a turbulent buoyant helium plume, Flow Turbul. Combust. 95 (2015) 143–168.

[187] K. McGrattan, R. McDermott, C. Weinschenk, G. Forney, Fire dynamics simulator users guide, sixth edition (2013). doi:https://doi.org/10.6028/NIST.sp.1019.

[188] Z. Wang, W. C. Tam, J. Chen, K. Y. Lee, A. Hamins, Thin filament pyrometry field measurements in a medium-scale pool fire, Fire Technol. 56 (2020) 837–861.

[189] N. Crauford, S. Liew, J. Moss, Experimental and numerical simulation of a buoyant fire, Combust. Flame 61 (1) (1985) 63–77.

[190] K. A. Jensen, J.-F. Ripoll, A. A. Wray, D. Joseph, M. El Hafi, On various modeling approaches to radiative heat transfer in pool fires, Combust. Flame 148 (4) (2007) 263–279.

[191] I. M. Kennedy, W. Kollmann, J.-Y. Chen, A model for soot formation in a laminar diffusion flame, Combust. Flame 81 (1) (1990) 73–85.

[192] V. A. Sabel'Nikov, L. F. F. da Silva, Partially stirred reactor: study of the sensitivity of the monte-carlo simulation to the number of stochastic particles with the use of a semi-analytic, steady-state, solution to the pdf equation, Combust. Flame 129 (1-2) (2002) 164–178.

[193] M. Smooke, M. Long, B. Connelly, M. Colket, R. Hall, Soot formation in laminar diffusion flames, Combust. Flame 143 (4) (2005) 613–628.

[194] H. Baum, K. McGrattan, R. Rehm, Three dimensional simulations of fire plume, in: Fire Saf. Sci.—Proceedings of the Fifth International Symposium, Tsukuba, Japan, 1996, pp. 511–522.

[195] T. Kangwanpongpan, F. H. França, R. C. da Silva, P. S. Schneider, H. J. Krautz, New correlations for the weighted-sum-of-gray-gases model in oxy-fuel conditions based on HITEMP 2010 database, Int. J. Heat Mass Transf. 55 (25-26) (2012) 7419–7433.

[196] A. Snegirev, E. Markus, E. Kuznetsov, J. Harris, T. Wu, On soot and radiation modeling in buoyant turbulent diffusion flames, Heat Mass Transf. 54 (2018) 2275–2293.